A FAULT-CONTROLLED GEOTHERMAL SYSTEM IN TARUTUNG (NORTH SUMATRA, INDONESIA) INVESTIGATED BY SEISMOLOGICAL ANALYSIS

Dissertation
zur Erlangung des akademischen Grades
"doctor rerum naturalium"
(Dr. rer. nat.)
in der Wissenschaftsdisziplin "Geophysik"

eingereicht an der
Mathematisch-Naturwissenschaftlichen Fakultät
der Universität Potsdam

von

Muksin

Potsdam, im April 2014

Published online at the
Institutional Repository of the University of Potsdam:
URL http://opus.kobv.de/ubp/volltexte/2014/7206/
URN urn:nbn:de:kobv:517-opus-72065
http://nbn-resolving.de/urn:nbn:de:kobv:517-opus-72065

Abstract

An integrated geological and geophysical approach was applied to comprehend the tectonic setting and seismic structure of the North Tapanuli district (North Sumatra Indonesia) where several geothermal manifestations are located. For the first time, passive seismic methods are used as a geothermal exploration tool in Indonesia. The specific aims of the seismological study are to provide Vp, Vp/Vs, and seismic attenuation images as well as the detailed fault structure of the region derived from seismicity and focal mechanism analysis. A seismic network of 42 short period instruments was installed in the region covering the Tarutung (in the north) and the Sarulla basin (in the south) for 10 months starting from May 2011. The seismic arrivals were detected by using an optimized automatic earthquake detection approach. The earthquakes were then localized by using HYPO71 with a 1D velocity model. In order to increase the picking accuracy, the seismic onsets were revised manually and the earthquakes were relocated by using the same procedure.

The seismic network recorded 2568 local earthquakes which are mostly located in the Tarutung and the Sarulla basins. Among these earthquakes, 809 events (with azimuthal gap angle less than 180^0) were used for further analysis. 45 different imposed 1D models were inverted and 809 events were relocated simultaneously by using VELEST. The model with small data variance and RMS residuals was chosen as the best 1D velocity model. The best 1D model together with the new hypocenter locations were used as the starting parameters for the 3D inversion for the Vp and the Vp/Vs modelling and hypocenter relocation (traveltime tomography) using SIMUL2000. Among 809 seismic events, 229 events with very good waveforms were involved in the attenuation tomography. A spectral inversion method was used to calculate the path attenuation (t^*) between a source and a receiver. SIMUL2000 was then applied to invert for the 3D seismic attenuation (Q_p) of the region. A further seismicity relocation (hypoDD) was performed and the focal mechanisms of the earthquakes were determined from first motion polarities by using a grid search method (HASH code) to derive the detailed fault structure of the region around the Tarutung basin.

The seismic structure (Vp, Vp/Vs, and Q_p anomalies) contributes to the physical properties and the lithology of rocks and possible fluid distribution in the region. The Vp model images the geometry of the Tarutung and the Sarulla basins. Both basins have a depth of around 2.0 km. High Vp/Vs and high attenuation (low Q_p) anomalies are observed along the Sarulla graben associated with a weak zone caused by volcanic

activities along the graben. Low Vp/Vs and low conductivity anomalies are found in the west of the Tarutung basin. This anomaly is interpreted as dry, compact, and rigid granitic rock in the region as also found by geological observations. Low Vp, high Vp/Vs and low Q_p anomalies are found at the east of the Tarutung basin which appear to be associated with the three big geothermal manifestations in Sipoholon, Hutabarat, and Panabungan area. These anomalies are connected with high Vp/Vs and low Q_p anomalies below the Tarutung basin at depth of around 3 - 10 km. This suggests that these geothermal manifestations are fed by the same source of the hot fluid below the Tarutung basin. The hot fluids from below the Tarutung basin propagate to the more dilatational and more permeable zone in the northeast. Granite found in the west of the Tarutung basin could also be abundant underneath the basin at a certain depth so that it prevents the hot fluid to be transported directly to the Tarutung basin. High seismic attenuation and low Vp/Vs anomalies are found in the southwest of the Tarutung basin below the Martimbang volcano. These anomalies are associated with hot rock below the volcano without or with less amount of partial melting. There is no indication that the volcano controls the geothermal system around the Tarutung basin. The geothermal resources around the Tarutung basin is a fault-controlled system as a result of deep circulation of fluids.

Outside of the basin, the seismicity delineation and the focal mechanism correlate with the shape and the characteristics of the strike-slip Sumatran fault. Within the Tarutung basin, the seismicity is distributed more broadly which coincides with the margin of the basin. An extensional duplex system in the Tarutung basin is derived from the seismicity and focal mechanism analysis which is also consistent with the geological observations. The vertical distribution of the seismicity suggests the presence of a negative flower structure within the Tarutung basin.

Contents

Chapter 1
Introduction

1.1 Motivation and goals

Indonesia is a country with a great potential of geothermal energy resources extending from the westernmost province, Aceh-North Sumatra to the easternmost province, West Papua. The geothermal resources in Sumatra are mostly located along the magmatic arc which correlates with the seismically active Sumatran Fault (Muraoka et al., 2010). One of the geothermal resources that has not been exploited is located around the Tarutung basin, south of Lake Toba, North Sumatra. Tarutung is the capital city of the North Tapanuli district. Another geothermal resource found in North Tapanuli is located around the Sarulla graben (further south of the Tarutung basin) which has been contracted to a geothermal company for exploitation. The Center for Geological Resources (CGR), the Indonesian governmental agency for geothermal exploration, proposes the resources in Tarutung as one of several potential target regions for the future extension of geothermal exploration and exploitation. The geothermal resource in Tarutung is represented by prominent geothermal manifestations (the Sipoholon, Hutabarat, and Panabungan hot springs, Fig. 1.4). So far, people build some recreational spots around the hot spring areas providing natural hot shower facilities.

In general, geophysical approaches have been used for geothermal exploration including geoelectric, geomagnetic, gravity and magnetotelluric measurement besides geology and geochemistry. In the Tarutung area, preliminary studies have been performed by CGR using geochemistry (Ardiwinata et al., 2005) and geology (Hasan et al., 2005) methods complemented by geophysical methods including geoelectric (Mustang et al., 2005), geomagnetic (Situmorang, 2005), and gravity (Djudjun, 2005) measurements. From these studies, a presumed magma chamber beneath the volcano called Martimbang volcano is interpreted to be the heat source of the geothermal system around the Tarutung basin (Djudjun, 2005; Hasan et al., 2005). However based on these geophysical measurements there is no clear evidence proving the relation between the magma chamber beneath the volcano and the geothermal system in Tarutung. In order to improve the understanding of the geological and tectonic setting of the geothermal system from the surface to depth we proposed an integrated approach including structural geology (e.g. Nukman and Moeck, 2013), geochemistry, magnetotelluric (Niasari et al., 2012), controlled source seismic (Wiyono et al., 2013), and

passive seismic investigations.

Passive seismic methods have been widely used in geothermal exploitation monitoring to investigate the characteristic changes of geothermal reservoirs, to track fluid movement, and to estimate the size of stimulated regions (e.g. Foulger, 1982; Julian et al., 1996; Jousset et al., 2011; Zucca et al. 1994). Unlike microseismic monitoring in geothermal exploitation that mostly deals with induced seismicity, in geothermal exploration we use natural tectonic earthquakes related to an active fault system as the seismic sources. The microseismic investigation is possible to be carried out in the Tarutung region because the region is located along the seismically active Sumatran fault. The Badan Meteorologi Klimatologi dan Geofisika (2012) and the USGS National Earthquake Information Center (2012) reported that earthquakes with magnitude larger than Mb 3.0 followed by the aftershocks occurring along the Tarutung and Sarulla basins. The main idea of the project is to provide a large picture of the tectonic system of the area including the fault and magmatic systems and their contribution to the geothermal system. From seismic imaging we could describe the structure of the region at different scales depending on the seismic experiment setup. The natural seismicity distribution represents a baseline study for future investigations to monitor induced seismicty.

Several authors have used passive seismic (seismology) methods to understand the seismic structures around geothermal areas and inferred the geothermal and tectonic setting of those regions (e.g., Chatterjee et al., 1985; Foulger, 1982; Husen et al., 2004; Jousset et al., 2011; Zucca et al., 1994). Seismic event distributions together with focal mechanism could illuminate the geometry and the pattern of the fault system. Having earthquake locations and focal mechanisms one could also determine the stress field of a region. Velocity anomalies (Vp, Vs, and Vp/Vs) obtained from traveltime tomography reflects rock properties, fluid and gas content, and lithology. Attenuation tomography is used to complement traveltime tomography. Intrinsic seismic attenuation is used to characterize fluid flow, fluid saturation, and temperature changes (e.g. De Lorenzo et al., 2001; Evans and Zucca, 1988; Zucca and Evans, 1992). One could also apply ambient noise tomography in a region with less seismic activity.

This study is a small part of an umbrella project called: “Sustainability concepts for exploitation of geothermal reservoirs in Indonesia - capacity building and methodologies for site deployment” funded by the German Federal Ministry of Education and Research (BMBF). The objectives of the passive seismic study for the Tarutung geothermal area are the following:

1. to investigate the fault structure determined from the seismicity distribution and focal mechanism,
2. to characterize the geothermal and volcanic system from joint interpretation of Vp, Vp/Vs and attenuation tomography together with the results of previous geophysical studies,
3. to develop a conceptual model of structure derived from the Vp, Vp/Vs, attenuation tomography and the seismicity distribution.

In the next section, I present the tectonic and geological background of Sumatra including the correlation between the subduction zone, the volcanic arc, and the presence of the Sumatran fault system. The discussion then focuses on the Tarutung region and its surroundings. In each publication I also describe the geological setting of the Tarutung region (Chapters 4, 5, and 6).

In Chapter 2, I discuss the seismic experiment and data preprocessing that consumed a large portion of the research time. The data preprocessing includes automatic detection of seismic arrivals, manual picking, first earthquake localization, and magnitude determination. In Chapter 3, I describe the theory behind the methods which were used in this study including 1D velocity determination and earthquake relocation, seismic tomography, relative relocation, and focal mechanism.

This dissertation is presented as the accumulation of the two published papers (Muksin et al., 2013a**;** 2013b) and one submitted manuscript (Muksin et al., 2014). Chapter 4 shows the results of seismic structure of the region based on the Vp and Vp/Vs tomography (Muksin et al., 2013a). Chapter 5 presents the 3D crustal structure derived from the attenuation tomography (Muksin et al., 2013b). The detailed fault system based on the advance hypocentre relocation and focal mechanism analysis is presented in Chapter 6 (Muksin et al., 2014). Based on the papers shown in Chapter 4, 5, and 6, a joint interpretation and synthesis of all results together with the results from other geophysical investigations is undertaken in Chapter 7. In this chapter, I summarize and conclude the contribution of the passive seismic investigation to the geothermal exploration in the area.

1.2 Geological and tectonic setting

1.2.1 Regional setting

The Tarutung region is located along the seismically active Sumatran Fault Sytem.

The fault was produced because of the presence of a large shear zone along the magmatic arc which was triggered by the oblique penetration of the Indo-Australian oceanic plate beneath the Sunda plate. Along Java the subducting plate moves nearly orthogonal to the trench and becomes more oblique along Sumatra and almost parallel to the trench along the Andaman region (Whittaker et al., 2007). The relative plate motion leads to steep subduction along the Java island and becomes shallower along the northern Sumatra and the Andaman region (Pesicek et al., 2010). The geometry of the subduction zone could also be influenced by the age and the convergence rates of the plates (Shapiro et al., 2008).

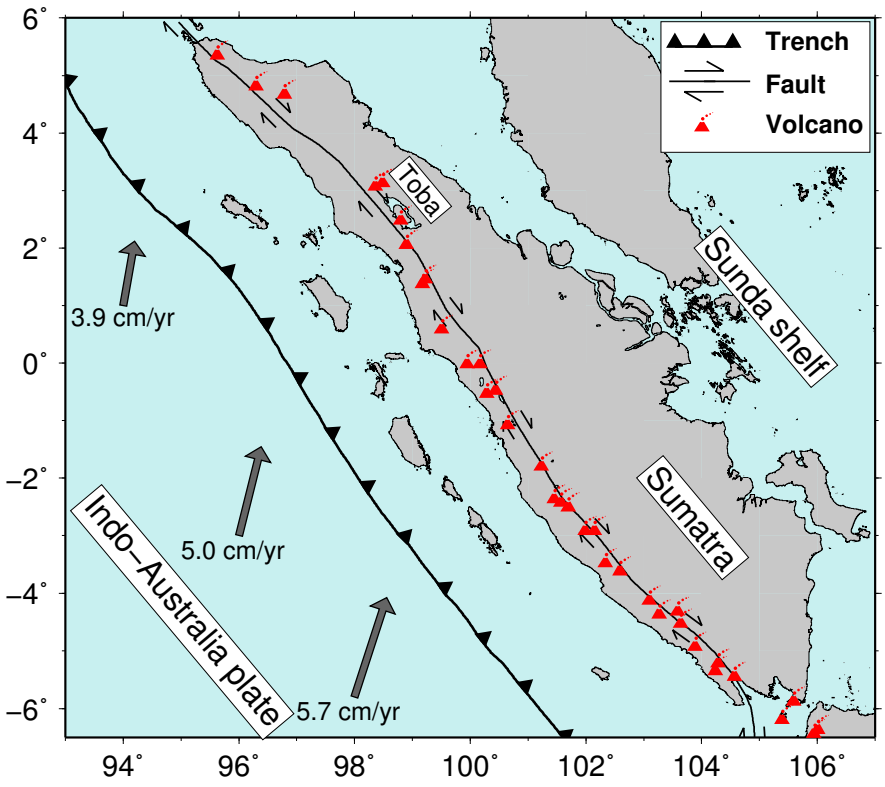

Figure 1.1: Obligue subduction results in the presence of the strike-slip Sumatran fault along the weak crustal line associated with the presence of volcanism along the island (Smithsonian Institution, National Museum of Natural History, Global Volcanism Program, 2012). The variations of rate and direction of movement of the Indo-Australian plate motion (represented by the arrows obtained from Subarya et al., 2006) is responsible for the segmentation of the fault.

The oceanic plate subducting beneath Sumatra has an age of 46-60 m.y and converges with a rate of 6.81 cm/yr. Around the former spreading center between the Indian and the Australian plates (Wharton ridge) the subducting material is observed to be more buoyant and thinner (Shapiro et al., 2008) which might be related to several

mega eruptions of the Toba supervolcano (see Fig. 1.1). Because the Indo-Australian oceanic crust penetrates the mantle, the water contained in the subducting slab lowers the melting temperature of the mantle. The magma then rises upward to produce the volcanic arc parallel to the Sunda trench. The 1,900 km long dextral slip Sumatran fault is formed to accommodate the trench-parallel component of the oblique convergence between the Indo-Australian and the Sunda plates. The fault is generated along the weakened volcanic arc line due to high temperature associated with magmatism (Beck, 1983). Therefore the Sumatran fault correlates with the volcanic arc line and the geometry of the Sunda trench (Sieh and Natawidjaja, 2000) (see Fig. 1.1). A complex interaction among the overriding, subducting, and the sliver plates has produced several smaller faults such as Batee and Mentawai faults (Sieh and Natawidjaja, 2000).

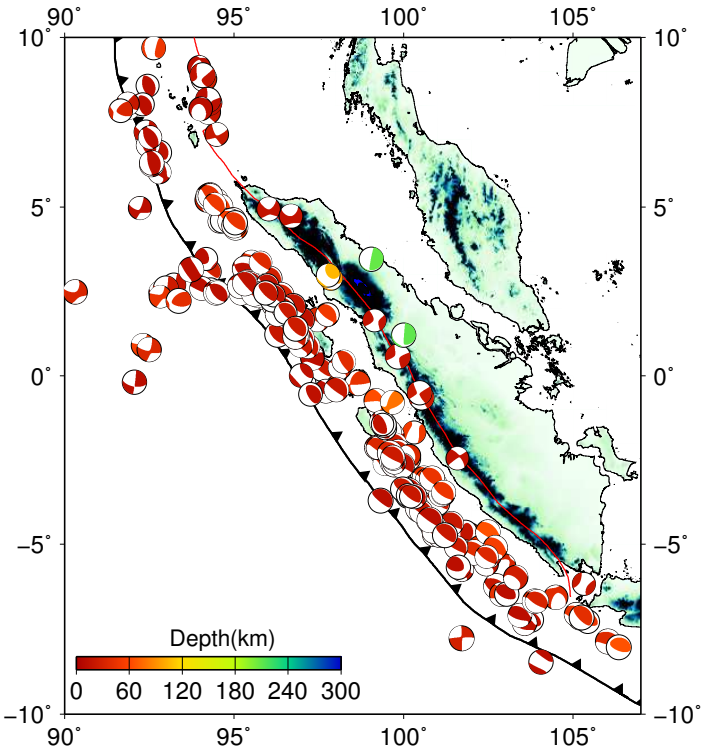

Figure 1.2: The distribution of earthquakes with magnitudes larger than Mw 5.5 along the Sumatran subduction zone (mostly thrust fault) and Sumatran Fault (mostly strike-slip) occurring in 1980-2014. The earthquake catalogue with focal mechanism is received from the Global Centroid Moment Tensor Project (2014).

As the consequence of the existence of the subduction zone and the Sumatran fault, Sumatra becomes one of the most seismically active regions in the world (Fig. 1.2). Two main types of earthquakes (with wide ranges of magnitudes) are (1) thrust fault

events on the subduction zone, and (2) strike-slip events on the Sumatran Fault System. After the mega thrust earthquake in Aceh 2004 with a magnitude of Mw 9.3 and its companion with a magnitude of Mw 8.5 in Nias, the region has become even more active. Recently, two large strike-slip earthquakes with magnitudes larger than Mw 8.0 followed by the aftershocks off the west coast of northern Sumatra. More recently, several hazardous strike-slip earthquakes also occurred along the Sumatran Fault.

Sieh and Natawidjaja (2000) divided the Sumatran Fault System into 19 major segments although smaller discontinuities also exist along the fault. Most of the segments are dilatational step overs although a few constractional bends also occur. Along the major segments strong and major earthquakes occur. The maximum magnitudes of the earthquakes correlate with the length of the segments. The lengths of the segments are mostly less than 100 km and only 2 segments have a length of 200 km. Because of the fault segmentation the magnitudes of the earthquakes tends to be smaller than Mw ~7.7 (See Sieh and Natawidjaja, 2000 for more detail). The obliquity of the convergence results in an increase of the slip rate of the Sumatran fault towards the northwest. The slip rate at the Sunda strait (the southernmost part of Sumatra) is around 6 mm/yr and increases to 17 mm/yr in central Sumatra (1^0S - 3^0N) (Bellier and Sébrier, 1995).

On the surface, the rock types along the Sumatran Fault correlates with the distribution of the volcanoes. From latitude of around 0^0 to the south of Sumatra volcanic rocks are observed along the fault (Fig. 1.3) correlating with a denser distribution of volcanoes (see Fig. 1.1). Huge amounts of volcanic rocks were found around the Toba area (Barber et al., 2005) including the Tarutung area associated with the eruption of the Toba super volcano around 74,000 years ago and other smaller eruptions, such as the Hopong volcano south of the Tarutung area. In the region with absence of volcanoes (3^0N to 4.7^0N) the lithology is dominated by Pliocene and Eocene sedimentary rocks. More to the north in Aceh (4.7^0N to 6^0N) the surface along the Sumatran fault is mostly occupied by older rock types, e.g. Upper Jurassic and Lower Cretaceous formations.

1.2.2 Geological setting of the Tarutung area

Geologically speaking the Tarutung area including the Tarutung and the Sarulla basins is a main feature along the Sumatran fault. Tarutung is mainly known as a highly populated capital city of the North Tapanuli district which was much larger before it was divided into three new districts. There are several geothermal resources

around the district which could be used for power generation. The Tarutung region is located between two main features along the Sumatran Fault: the Toba caldera (in the north) and the strike-slip duplex structured bifurcation (in the south) (Weller et al., 2012). The term bifurcation was introduced in Sieh and Natawidjaja (2000). The Tarutung region is characterized by a diamond-shape pull-apart basin in the north and the Sarulla graben in the south (Fig. 1.4). After the Toba caldera developed, a new branch of strike-slip fault crossing the Toba basin was formed. The Tarutung pull-apart basin was formed because the fault around the present day location of the basin was bent (Bellier and Sébrier, 1994).

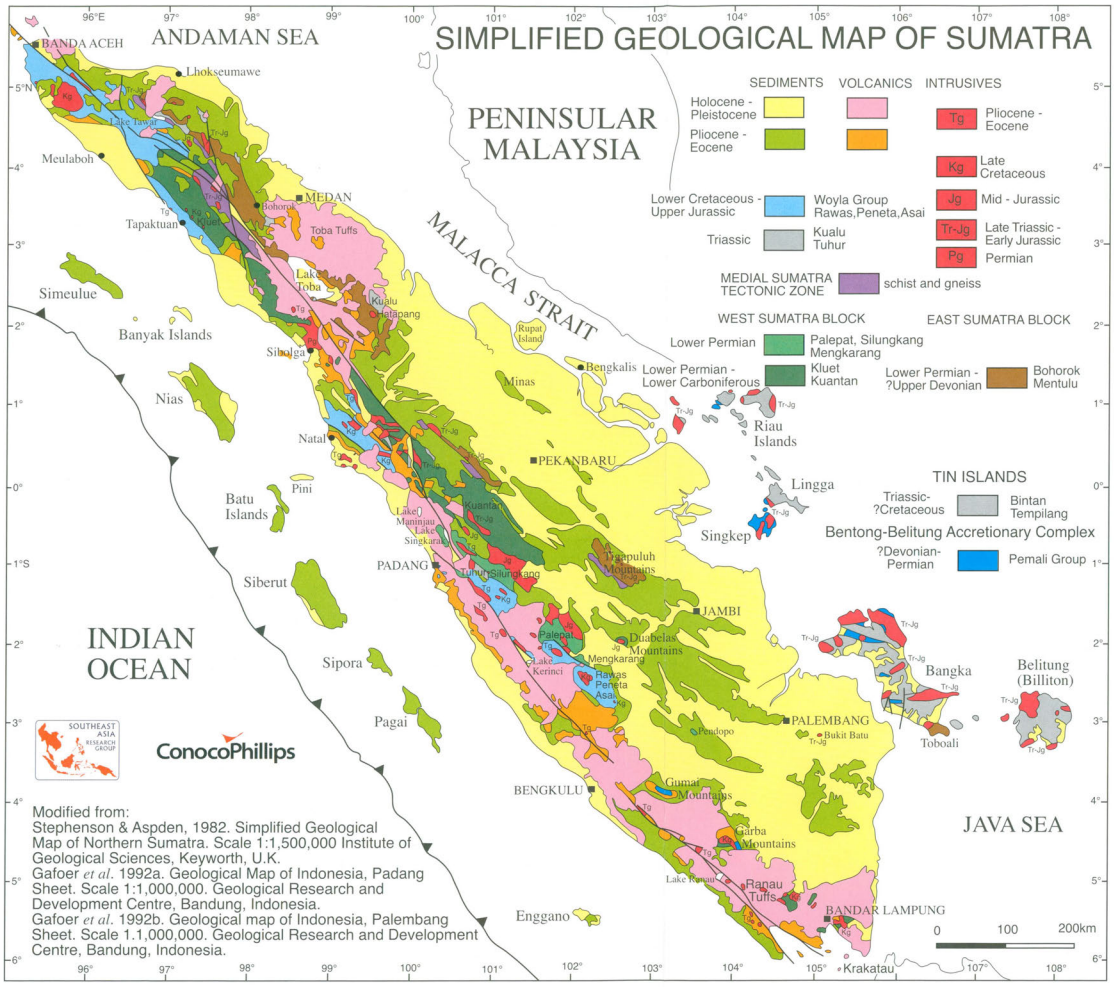

Figure 1.3: Simplified geological map of Sumatra (Crow and Barber, 2005).

A similar mechanism led to the formation of the Suoh pull-apart basin (around 4^0S) after the development of the Ranau caldera. The Sarulla graben on the other hand is not a typical pull-apart basin like the Tarutung basin. Hickman et al. (2004)

suggested that the Sarulla graben is bounded by the western margin of the fault and does not occupy a releasing step between two strike-slip faults. The Sarulla graben is also characterized by several normal faults which run parallel to the Sumatran fault. Both, the Tarutung and the Sarulla basins are seismically active with maximum magnitudes of Mb 6.0.

Nukman & Moeck (2013) propose a caldera-like structure in the northeast of the Tarutung basin identified by the SRTM map as indicated in Fig. 1.4. In the southwest of the Tarutung basin there is a young stratovolcano named Martimbang volcano. This yet undated volcano is characterized as a young andesitic basaltic cone (Hickman et al., 2004). There is a volcanic field dome located just south of the Martimbang volcano called Namora Langit consisting of dacite and rhyolite domes and andesitic rocks. An old caldera with a diameter of 9 km is located at the eastern margin of the fault along the Sarulla graben called Hopong caldera.

At the surface, the Tarutung basin is covered by alluvium and several travertines found at the eastern margin of the basin. The Tarutung basin is mostly covered by the youngest rock type called Toba Tuff with an age of ~74,000 year related to the latest Toba eruption. The older rock type is dacite of the Tuk-Tuk formation with an age of around 1.9 Ma which is found within the basin and on the eastern margin of the basin. Large amounts of andesitic rocks found within the Tarutung area show an age of mid-Miocene. Older than the andesitic rock is the granitic rock type found in the west of the basin, showing ages of around 264 Ma. The oldest rock type found in the Tarutung basin is the phylitic slate complex of the Kluet formation of Late Carboniferous found in the western edge of the basin and the wacke and quartz arenites of the Bohorok formation observed in the east (Nukman and Moeck, 2013). The detailed statigraphy of the Sarulla basin is described in Hickman et al. (2004). The recent rock type at the surface of the Sarulla basin is Alluvium. Dacite, basalt, and andesite are found in the northern Sarulla graben. Hickman et al. (2004) found andesite, Dacite and Hopong Tuff within the vicinity of the Hopong caldera.

1.2.3 Geothermal manifestations and previous geophysical work

Around both, the Tarutung basin and the Sarulla graben, we found several hot springs manifesting the geothermal resources in the North Tapanuli (Tarutung) district. There are three main clusters of the geothermal manifestations around the Sarulla graben which are mainly controlled by active volcanism as follows (Hickman et al., 2004):

1. The boiling chlorite springs in the Donatasik area located on the eastern and the western margin of the southern part of the Sarulla graben. From geothermometry analysis the Donatasik waters equilibrated at 200 - 300 ^0C.
2. A group of hot springs located closely to the Silangkitang area that has been explored and some drillings have been made. The Silangkitang geothermal source is located above a sub-graben formed between two smaller faults that are parallel to the Sumatran fault. The fluid temperature of the geothermal resource in this area could exceed 310 ^0C at 2 km depth.
3. The geothermal resources related to the Namora Langit field dome, consisting of a large number of fumaroles and acid sulfate springs. This geothermal system is strongly controlled by the volcanism rather than by the faults. Four wells have been drilled and were classified as highly permeable with temperatures exceeding 260 ^0C, with the potential to generate energy of 210 MW.

Unlike the hydrothermal resources around the Sarulla basin, the fluid discharges around the Tarutung basin have low to medium temperatures. The geothermal fluid discharges around the Tarutung basin are less volcaniccally controlled (Nukman and Moeck, 2013). There are at least 18 high PH fluid discharge centres around the Tarutung basin as indicated by red stars in Fig. 1.4. The three big red stars represent the larger and the higher temperature hot springs named after the villages Sipoholon (Si), Hutabarat (Ht), and Panabungan (Pg). The highest temperature of the hot fluid discharge is at the Sipoholon location about 65.5 ^0C. The other two big hot springs, the Hutabarat and the Panabungan hot springs have temperatures of around 52 ^0C and 49 ^0C, respectively while the other springs have temperatures below 50 ^0C. The hot springs at the eastern margin of the Tarutung basin are characterized by the presence of travertine. The hot spring at the Panabungan village has higher fluid flow rate than the other sites. The pictures of these three hot springs are provided in Appendix A. Bigger hot springs are predominantly exposed at the eastern side of the Tarutung basin which might be related to the tectonic setting in this region (Nukman and Moeck, 2013).

The geothermal systems around the Sarulla basin have been studied in detail by using different approaches including geology, geochemical and geophysical methods and are explained in detail in Gunderson et al. (2000). The geophysical methods used included gravity, time-domain electromagnetic (TDEM) and magnetutelluric (MT) surveys. A low gravity anomaly is found along the Sarulla graben which could reflect the tuff-filled graben as also confirmed by drilling results. MT and TDEM results show a much lower resistivity anomaly in the Silangkitang village than that along the

Sarulla graben indicating a clay-rich alteration and shallow depth geothermal system.

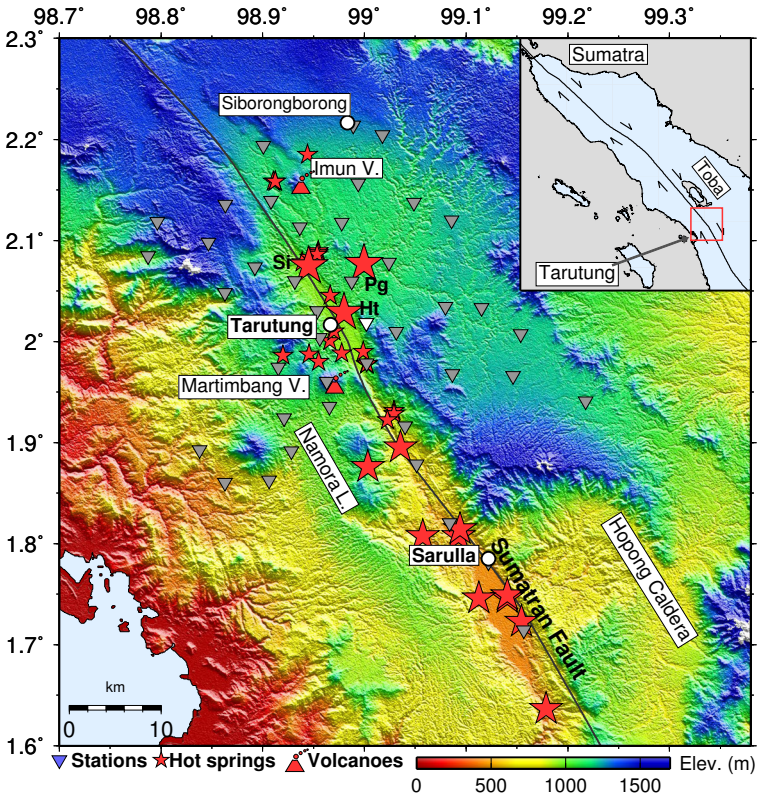

Figure 1.4: Topographic map of the Tarutung region showing the location of the hot springs and the seismic stations

In the Namora Langit area, a low gravity anomaly was found in the center of the volcanic complex, located between the two principal strands of the Great Sumatran Fault. This possibly reflects the tuff-filled graben underlying lavas of the volcanic complex as also confirmed by drilling results. The TDEM and MT studies revealed a prominent low resistivity anomaly at the southern thermal region associated with clay alteration underlying the geothermal system in the area.

Around the Tarutung basin geothermal exploration has been carried out by using geology, geochemical and geophysical methods. The geophysical methods used included geoelectric (Mustang et al., 2005), geomagnetic (Situmorang, 2005) measurements, and gravity (Djudjun, 2005) methods. However, the geophysical investigations were focused only on the vicinity of the Sipoholon hot spring. The geolectrical measurement revealed a low resistivity body around the Sipoholon hot spring at the eastern margin of the Tarutung basin at depths of around 0.5 km which extends more to the west at depths of 1.5 km. A low magnetic anomaly is found below the Sipoholon hot

spring. The gravity study found a high Bouguer anomaly located slightly southeast of the Sipoholon hot spring.

Chapter 2

Experiment and data preprocessing

2.1 Seismic experiment

The SIPOSEIS network consisting of 42 short period seismic instruments was installed for 10 months starting mid of May 2011 in the Tarutung district as shown in Fig. 2.1. 40 seismic stations were equipped with three component short-period (1 Hz) Mark sensors and 2 stations with three component PE-6/B 4.5 Hz geophones.

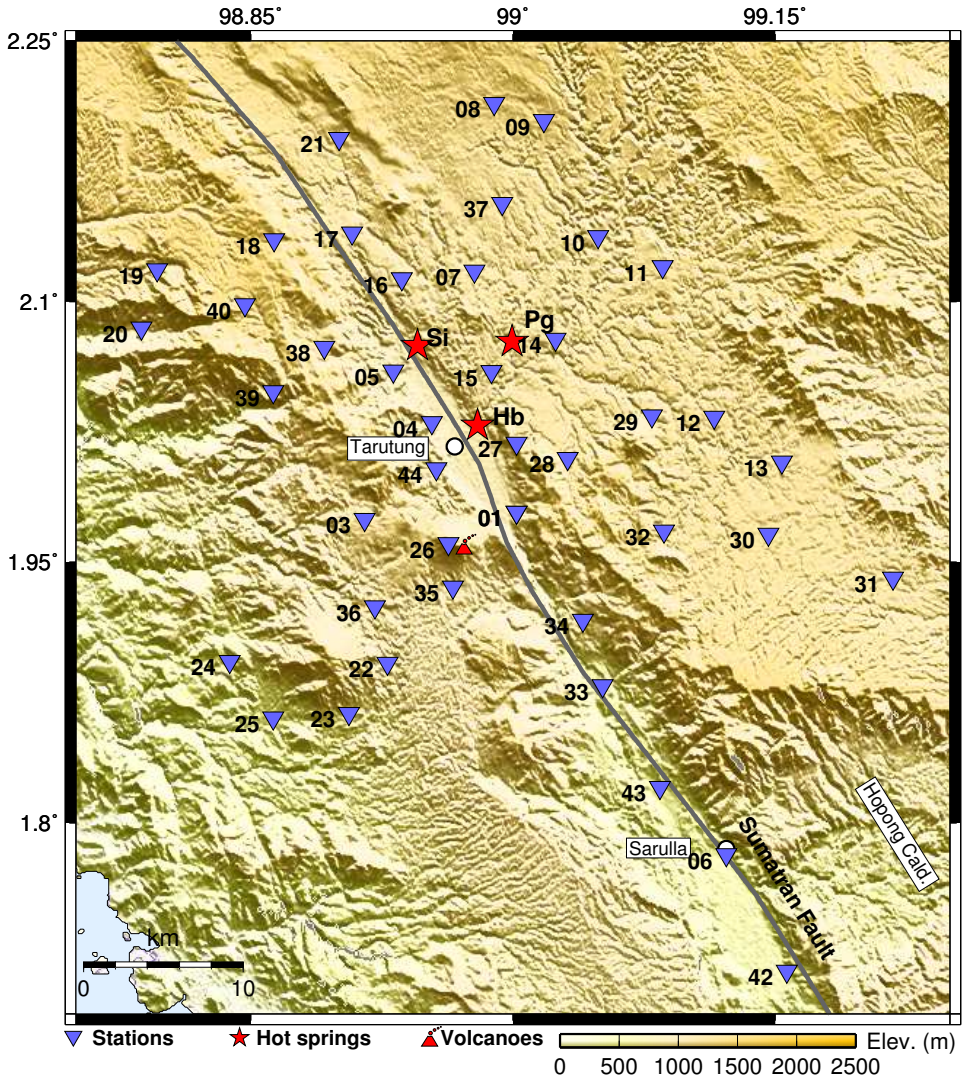

Figure 2.1: The distribution of the seismic stations in the area. The numbers indicate the name of the station.

The signals from the mark sensors were recorded by PR6-24 Earth Data Logger (EDL) sampling at 100 sps. The signals from the other two stations were recorded by DSS CUBE data logger (Omnirecs) at 200 sps. The network covers the entire district (between 1.71 N to 2.21 N and 98.79 E to 99.22 E) to record the local seismicity along the Sumatran fault especially along the Tarutung and the Sarulla basin so that the ray-paths could traverse the main sources of the geothermal system. The station list and the picture of the deployment are provided in Appendix B.

The stations were distributed with closer spacings around the Tarutung basin and coarser outside of the basin. With the average spacing of 5 km between stations, the seismic network aperture is around 35 km crossing the Sumatran fault and around 40 km parallel to the fault. With this station distribution, we could obtain a stable solution of the hypocenters at depth above 35 km. The stations could not be evenly distributed because of inaccessible areas. For safety reason, we deployed the instruments mostly within the government facilities and in private farming lands.

2.2 Automatic detection and earthquake localisation

There are several steps to be performed in order to obtain the first location of earthquakes. First, I automatically picked the P-wave arrivals of earthquakes and then localized the earthquakes. Having the first version of the earthquake catalogue I then manually revised the P- and S-wave arrivals. The hypocenters of the earthquakes are then relocated according to the revised arrivals.

The P-wave arrivals were automatically detected by using optimized automatic pickers (Nippress et al. 2010). The picker includes three different well recognized automatic detection techniques: STA/LTA (short term average/ long term average), PAI-K (phase arrival identification-kurtosis), and T^{pd} (damped predominant period) pickers. The STA/LTA picker (e.g. Allen 1978) calculates the STA and the LTA of a function defined by:

$$E_k = (x_k)^2 + (x_k^{'})^2 + C \tag{2.1}$$

where x_k is the seismic trace, $x_k^{'}$ is its derivative and C is a contant defined by the user. The algorithm detects an arrival when the ratio of STA/LTA exceeds a defined threshold value. Using this method a user need to define a threshold value, STA and

LTA window length for each station.

The PAI-K picker (Saragiotis et al. 2002; 2004) indentifies seismic arrivals based on a significant change in statistics of an M sample sliding window of a seismic trace. The arrival is determined at one sample before the kurtosis $\hat{\gamma}_k$ (k=M, M+1, ..., N) reaches the maximum as defined by:

$$\hat{\gamma}_k = (M-1)\frac{\sum_{n=k-M+1}^{k}(x(n)-\hat{m}_k)^4}{\left[\sum_{n=k-M+1}^{k}(x(n)-\hat{m}_k)^2\right]^2} - 3 \tag{2.2}$$

where $\hat{m}_k = \left[\sum_{n=k-M+1}^{k} x(n)\right]/M$. The appropriate trigger level and the sliding window are defined by the user.

The third picker applied in this optimized automatic picker is the T^{pd} picker (Hildyard et al. 2008; 2010). A seismic phase is considered to arrive when a threshold value is exceeded by the T^{pd} defined as:

$$T_i^{pd} = 2\pi\sqrt{\frac{X_i}{D_i + D_s}}, \tag{2.3}$$

where X_i and D_i are defined as

$$X_i = \alpha X_{i-1} + x_i^2 \tag{2.4}$$

and

$$D_i = \alpha D_{i-1} + \left(\frac{\partial x}{\partial t}\right)_i^2 \tag{2.5}$$

D_s is a constant related to the signal to noise ratio and α controls the influence of the preceeding trace in the $X_{i\text{-}1}$ and $D_{i\text{-}1}$. Hildyard et al. (2008) defined α as

$$\alpha = e^{\frac{ln(0.1)}{\tau/\triangle t}}, \tag{2.6}$$

where $1/\Delta t$ is the sampling rate. The T^{pd} is evaluated along a continuous waveform

with the user defined D_s, τ, and a threshold level parameter.

In the optimized automatic picker, the first picker is used to detect the arrivals and the two other pickers work in tandem to improve the picking accuracy. The service trips made two months after the deployment offerred the possibility to determine the appropriate parameters to be used in the automatic picking procedure. I then located the events by using the HYPO71 code (Lee and Lahr 1975) and the IASP91 velocity model (Kennett and Engdahl 1991). The arrivals were then manually revised and the hypocenters were relocated by using the same procedure.

Fig. 2.2 shows the vertical components of the seismic waveforms of two local earthquakes occured below the Tarutung basin. The recording of these two local earthquakes within 40 seconds evidences that the region is very active.

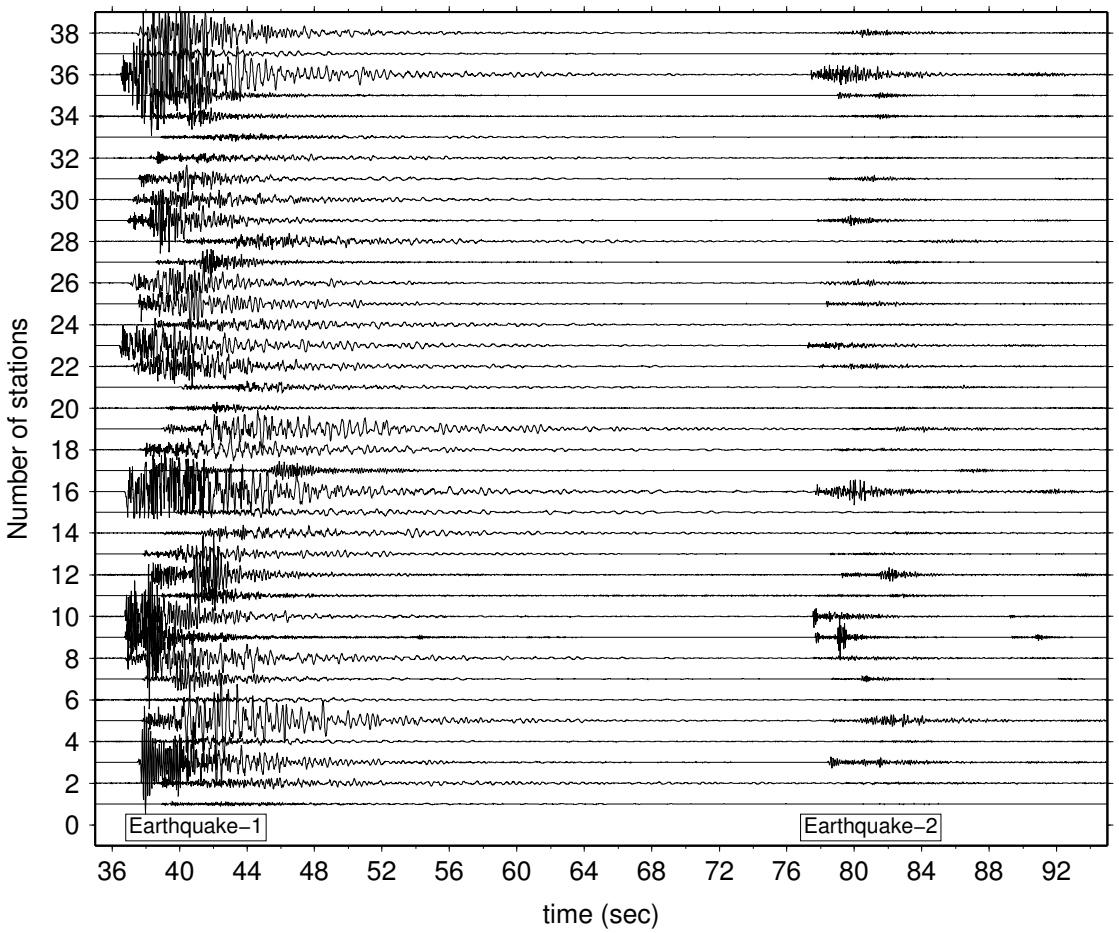

Figure 2.2: The vertical components of the seismic waveforms of two local earthquakes occured in the Tarutung basin on 1st September 2011 recorded by the SIPOSEIS network .

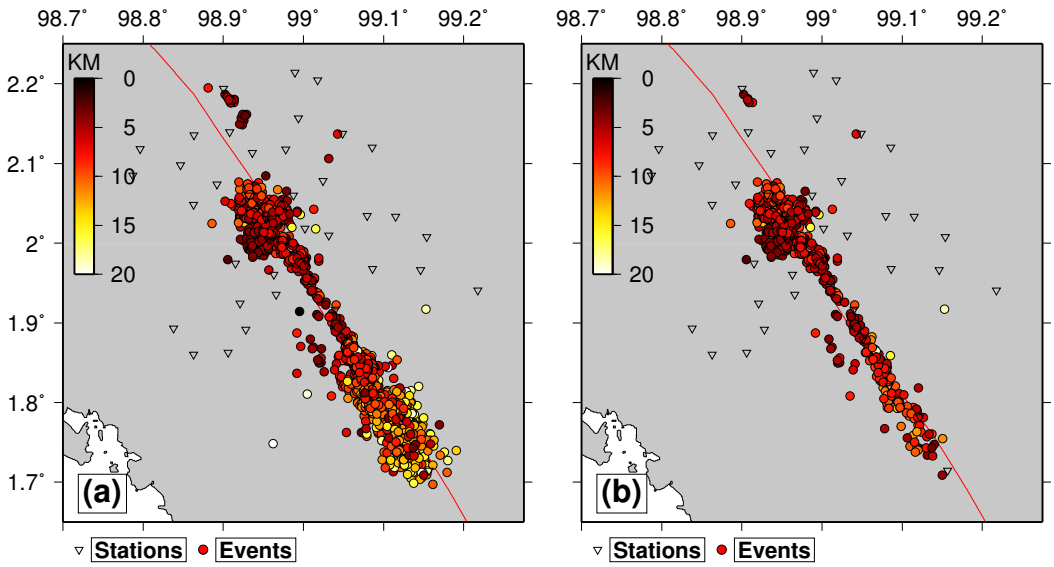

Figure 2.3: (a) All local earthquakes recorded by at least 8 stations during the seismic experiment. The large number of events in the south of the Tarutung district are the aftershocks of the Mb 5.8 eartquake in June 2013 destroying some buildings. (b) Local earthquakes with gap angles less than 180^0 used for further analysis.

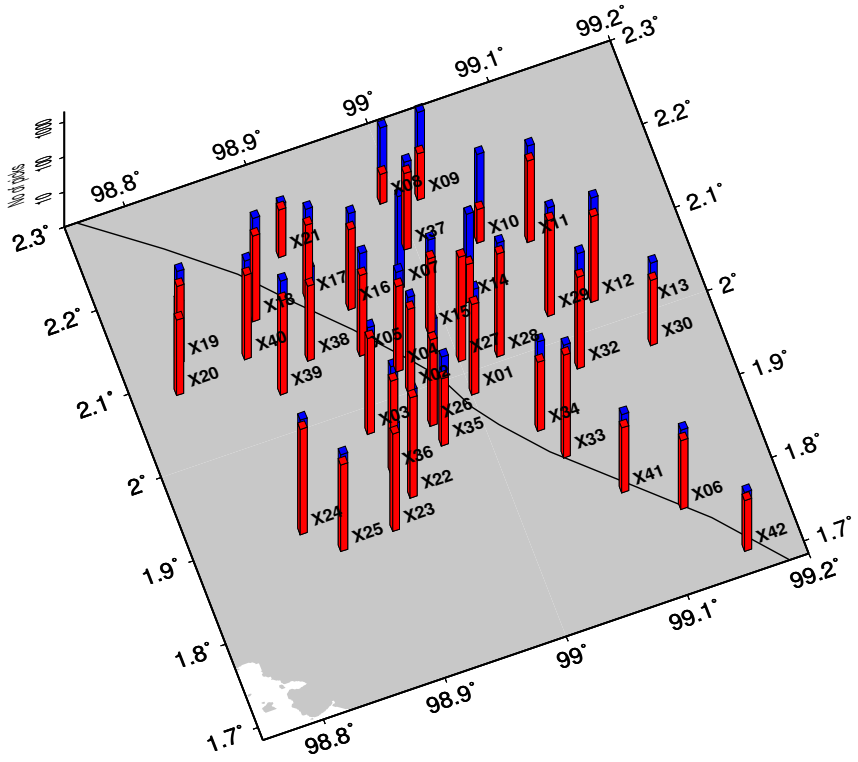

Figure 2.4: The distribution of the *P*- and *S*-wave arrivals of events located within the network picked by all stations represented by the blue and red bars, respectively.

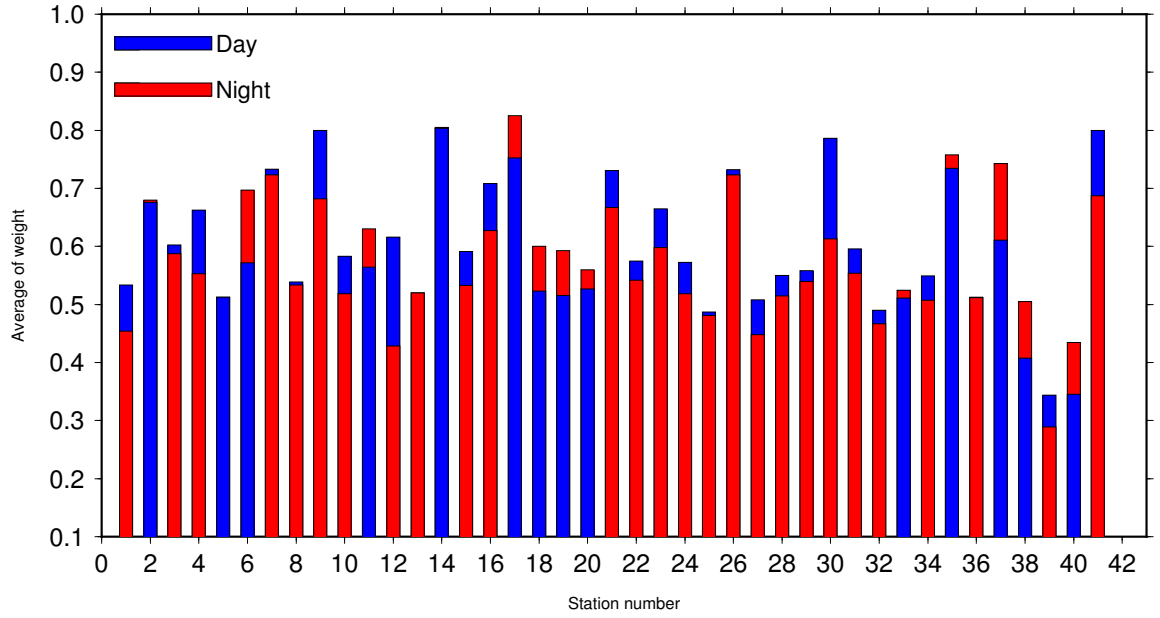

Figure 2.5: The average of the picking weights for each station. The blue and the red bars represent the events recorded during the day (6:00 to 21:00 local time) and during night (21:00 - 6:00).

During the deployment, 2586 local earthquakes were recorded by at least 8 stations (Fig. 2.3a). The large number of events in the south of the Tarutung district was related to the aftershocks of the Mb 5.8 right lateral strike-slip earthquakes occured on June 16, 2011. However, among this large number of events only 809 local earthquakes (Fig. 2.3b) were located in the network (eents with azimuthal gap angle less than 180^0) which are used for further analysis. The earthquakes with gap angle larger than 180^0 were exluded in order to obtain a better solution of the hypocentre location.

The distribution of the arrivals was comparable among stations as shown in Fig. 2.4. The area along the Sumatran fault is considered a noisy area since it is densely populated. The stations along the fault recorded a large number of events because the stations are close to the epicentres. Although a lot of earthquakes occurred in the south of the Tarutung district the station X06 (the southernmost station) did not record the events because of technical problems. Stations X42 and X43 in the southern Tarutung district (see Fig. 2.1) were deployed later so that the instruments also did not record the large number of the aftershocks of the Mb 5.8 event. Therefore, a large number of events in the southern Tarutung district have gap angles larger than 180^0 and should be excluded from further analysis.

During the step of the manual arrival revision, I assigned a weight to each pick associated with the uncertainty of the observed phase arrivals. The weight of picking

is defined by 0, 1, and 2 correlating with the estimated uncertainty of 0.01 s, 0.05 s, and 0.1 s, respectively. Therefore the weight of the picking could be associated with the estimated uncertainty which is mainly related to the noise level around the stations. Fig. 2.5 shows the average of the picking weight at each station during day (6:00 - 21:00 local time, blue bars) and night (21:00 - 6:00, red bars).

The idea of distinguishing the records between day and night was driven by the fact that the instruments were mostly deployed in public areas (e.g schools, churches, and offices) which were supposed to be noisy during the day and less noise during the night. Fig. 2.5 shows that there is no significant difference between day and night records. The average of the picking weight associated with the estimated uncertainties between night and day time are comparable which indicates that there is no big impact of human activities around the stations to the noise level of the data. The noise level seems to be dependent on the location of the stations. For the stations deployed in isolated areas (e.g., station 01, 05, 18-20, and 39) the average of the picking weight is lower during day and night. On the other hand, for the stations situated in noisy areas, (e.g, stations 07, 14, and 41) the average of the picking weight is higher all day (day and night).

2.3 Magnitude determination

The magnitude calculation is another basic task in seismological studies. Magnitudes of earthquakes represent energy release, physical size of earthquakes, and seismic hazard. Together with the hypocenter locations and the focal mechanisms, the magnitudes of earthquakes contribute to the understanding of the tectonic setting of an area of interest.

Different approaches are used to calculate earthquake magnitudes according to their distances. Parameters for the determination of global earthquake magnitudes have been well accepted by seismologists. For regional and local distances, the magnitudes of earthquakes are significantly influenced by the variation of local attenuation and geometrical spreading. For teleseismic earthquakes, magnitudes are often presented by: (1) body wave magnitude, m_b (for magnitudes < 7 and distances in the range of $20^0 - 100^0$), (2) surface wave magnitude, m_s (for magnitude < 8 and distance between $20^0 - 160^0$), and (3) moment magnitude, M_w for all distance ranges (Havskov and Ottemöller, 2010).

For local earthquakes, the local magnitudes are often expressed by M_L defined as

(Havskov and Ottemöller, 2010):

$$M_L = log(A) + a\log(r) + br + c \tag{2.7}$$

where A is the S-wave amplitude as a function of the hypocentral distance r. Parameters a, b, and c represent geometrical spreading, attenuation, and the base level, respectively.

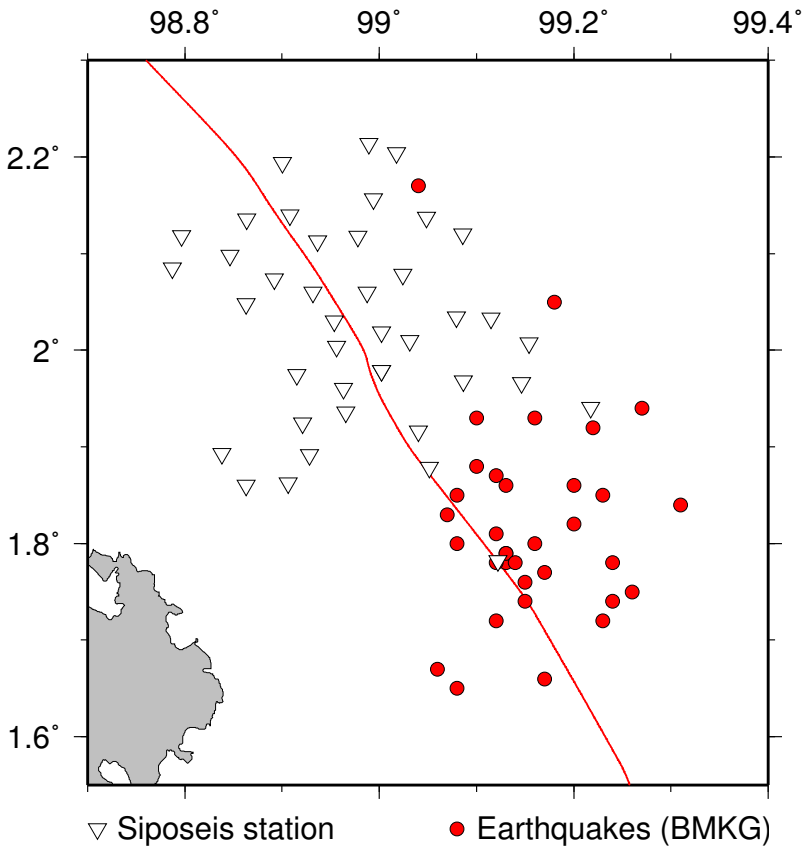

Figure 2.6: The widely distributed earthquakes without relocation around the Tarutung region provided by BMKG.

The parameters a, b, and c were determined by calibrating the earthquake magnitudes with the local magnitudes of earthquakes around the Tarutung region provided by the National Agency of Meteorology, Geophysics, and Climatology of Indonesia (Badan Meteorologi, Klimatologi, dan Geofisika, BMKG). The earthquake locations provided by BMKG are widely distributed because no relocation was applied to the data. Although the earthquake locations provided by BMKG are not well relocated as shown in Fig. 2.6, these BMKG earthquakes are the only local data available

that could be used for the calibration. The comparison between the magnitude provided by the BMKG and our network (SIPOSEIS network) is shown in Fig. 2.7. Since earthquake hypocenters provided by BMKG were not well located I could only compare six earthquakes with identical origin times.

The distribution of earthquake magnitudes located within the network (with azimuthal gap angle $\leq 180^0$) is shown in Fig. 2.8. A large earthquake occurred in the south of the Tarutung area. However, I excluded this earthquake and its large number aftershocks because they were located outside the network. From the resulting magnitude, I analysed the magnitude frequency distribution to determine the so-called b-value of the region. The relation between the frequency occurrence and the magnitudes of earthquakes is expressed by Gutenberg and Richter (1944):

$$\log_{10} N = a - bM \tag{2.8}$$

where N is the number of earthquakes with magnitudes larger than M while a is a contant and b is the slope of a log-linear relation known as b-value. Authors use the b-value to identify large earthquake precursor (e.g., Smith, 1981).

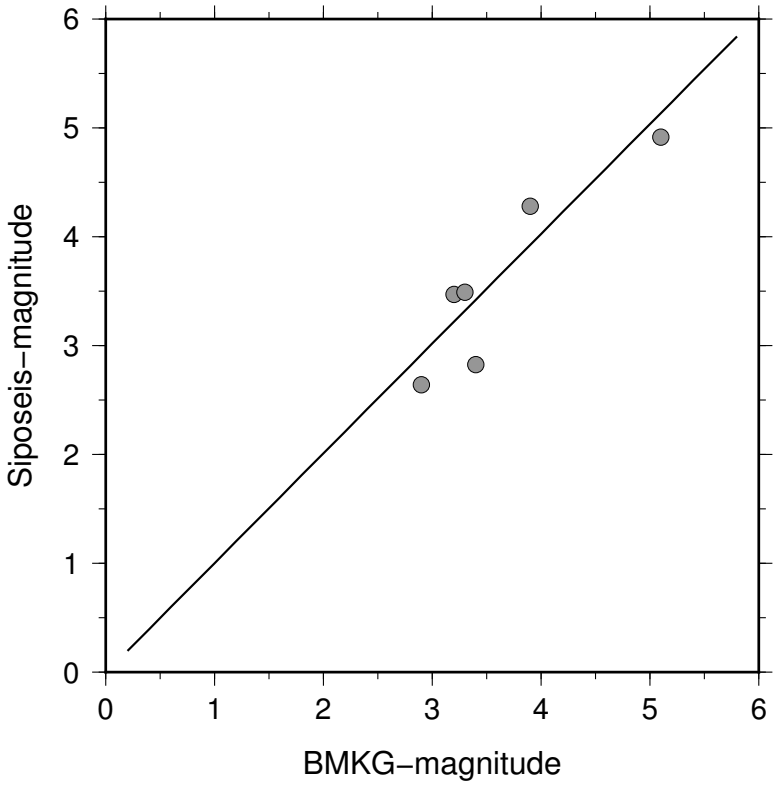

Figure 2.7: A comparison between earthquake magnitudes around the Tarutung region provided by BMKG and our calculation.

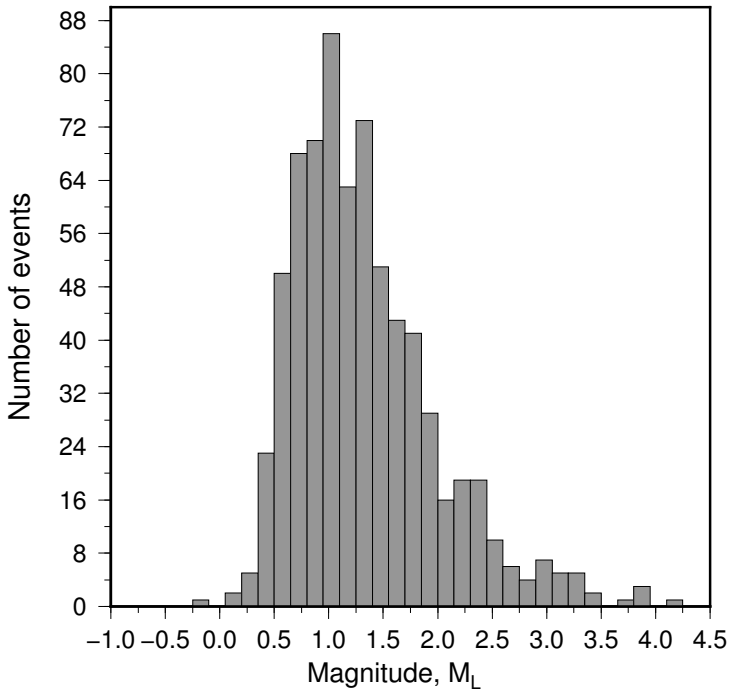

Figure 2.8: The distribution of eathquake magnitudes in the Tarutung region located within the network.

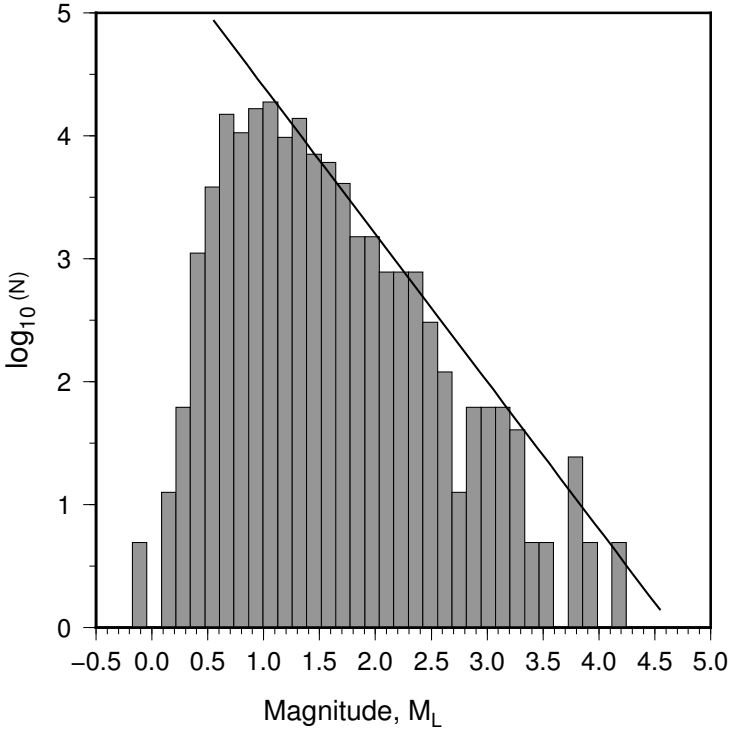

Figure 2.9: Determination of the b-value (the slope of log-linear relation, black line) for the Tarutung geothermal region which resulted *in* b=1.17 and a=5.6.

Generally, the b-values are distributed between 0.5-1.5 (for natural tectonic earthquakes) and for a seismically active region the b-value is around 1.0. Applying equation (2.8) to the distribution of the earthquake magnitudes I derived the b-value for the Tarutung region as described in Fig. 2.9. For the Tarutung region a b-value of 1.17 and a constant value a of 5.6 were obtained.

Chapter 3

Methods of seismic tomography, relocation and focal mechanism

3.1 1D velocity modelling and hypocenter relocation

The determination of the hypocenter location is nonlinearly dependent on the given 1D velocity model and vice versa. In seismic tomography, the solution of a 3D velocity model is highly dependent on the assigned initial model (disscussed in the next subsection). In global tomography, authors (e.g, Dziewonski, 1984; Van der Hilst et al., 1991) used well recognized 1D global models such as PREM (Dziewonski and Anderson, 1981), IASP91 (Kennett and Engdahl, 1991), and ak135 (Kennett et al., 1995) as the references. For regional tomography, a coarse 3D global model is used as a reference and the data is inverted to obtain the finer regional model (e.g., Gorbatov et al., 2001; Widiyantoro et al., 1999). In local earthquake tomography, authors initially determine a 1D velocity model to be used as the reference model to invert the 3D velocity model (e.g., Thurber, 1983; Koulakov, 2009). Therefore, before performing a seismic tomography inversion I derived a 1D velocity model for Vp and Vp/Vs and simultaneously relocated the hypocenters by using the VELEST software (Kissling et al., 1994).

The observed traveltimes of a seismic phase of a seismic source can be expressed as a nonlinear function of the velocity model m, hypocenter parameters h (including origin time), and station coordinates s (Kissling et al., 1994):

$$t_{obs} \quad = \quad f(s, h, m) \tag{3.1}$$

The observed arrival times and the station coordinates are known while the velocity model m and hypocentre parameters h are unknown therefore the problem cannot be solved directly. A velocity model was given and the locations of seismic sources were determined by using HYPO71 (Lee and Valdes, 1985). The theoretical traveltimes t_{calc} were then calculated. The appropriate velocity model and hypocenter parameters are accepted when the residual between t_{obs} and t_{calc} is minimum. Following the first-order Taylor series expansion of equation (3.1), the traveltimes residual can be expressed

(Kissling, 1988) as

$$t_{res} = t_{obs} - t_{calc} = \sum_{j=1,4} \frac{\partial f}{\partial h_j} \triangle h_j + \sum_{i=1,N} \frac{\partial f}{\partial m_i} \triangle m_i + er \tag{3.2}$$

where Δh and Δm are the adjustments of the hypocentre parameters and velocity model, respectively. Equation (3.2) can be expressed in matrix formulation representing the coupled relation between hypocenter and velocity model parameters (Kissling, 1988; Kissling et al., 1994) as

$$t = Hh + Mm + e = Ad + e \tag{3.3}$$

where t are the traveltime residuals, H is a matrix containing the partial derivative of traveltimes with respect to hypocentral parameters, h is a vector of hypocentral parameter changes, M is a matrix of partial derivatives of traveltimes with respect to model parameters, m is a vector of model parameter changes, e is a vector of traveltime errors, A is a matrix of all partial derivatives and d is a vector of hypocentral and model parameter adjustments. Equation (3.3) shows two separated matrix equations, the matrix equation containing the velocity model parameters and the one consisting of the hypocentral parameters only. The equations are solved by using a damped least square inversion method (Kissling, 1988).

Using the HYPO71 earthquake localization, the velocity model is static and the location of earthquakes are calculated based on this fixed velocity model. Using VELEST, I employed a "guess" initial velocity model and then the location of earthquakes and the velocity model are adjusted simultaneously. The calculation is performed continuously until the minimum values of the average of the RMS (Root-Means-Square error) for all earthquakes are achieved. The final results of the velocity model and hypocentral parameters could be trapped in a local minimum depending on the imposed initial model. Therefore, I imposed several possible initial velocity models and then performed the inversion. All final results are then compared and I choose the best solution of all inversion results. This procedure, proposed by Kissling et al. (1994), results the global minimum of a 1D velocity model. The best solution of the velocity model and the hypocentre parameters are then used for further analysis, for example for traveltime and attenuation tomography. The detailed procedures and the results of the 1D velocity modelling and earthquake relocation for the Tarutung region are provided in Chapter 4.

3.2 Traveltime tomography

The main objective of traveltime tomography is to obtain a seismic velocity structure (in this case a 3D structure) derived from traveltime data. There are at least four steps required in performing traveltime tomography (e.g., Rawlinson and Sambridge, 2003):

1. Model parameterisation: A region is gridded into several small cells. Initial parameters need to be specified including initial velocity model e.g., 1D global model or 1D local model calculated by VELEST.
2. Forward calculation: The predicted traveltime is calculated based on different ray or wave propagation traversing along a given velocity model.
3. Inversion: The calculation of model parameters to minimize the misfit between predicted traveltimes and observed data (measured traveltimes).
4. Analysis of solution robustness: The quality of the results is analysed by evaluating the resolution matrix and covariance matrix, complemented by synthetic tests.

3.2.1 Forward calculation

The content of this section is mostly summarized from the paper of Rawlinson and Sambridge (2003). Forward calculation in a traveltime tomography is the calculation of the minimum traveltimes between a source S and a receiver R through a velocity structure $v(\mathbf{x})$ which is expressed by:

$$t = \int_S^R \frac{1}{v(\mathbf{x})} dl \tag{3.4}$$

where dl represents the differential path length. The Eikonal equation expresses a propagation of seismic wavefront for an elastic medium as follows:

$$(\nabla_{\mathbf{x}} T)^2 = \frac{1}{[v(\mathbf{x})]^2} \tag{3.5}$$

where T is the traveltime of the wavefront. The ray equation can be derived from the Eikonal equation by considering a change in position $d\mathbf{x}$ in a small time step dt as:

$$\frac{d}{dl}\left(\frac{1}{v(\mathbf{x})}\frac{d\mathbf{x}}{dl}\right) = \nabla\left(\frac{1}{v(\mathbf{x})}\right) \tag{3.6}$$

Equation (3.6) can be used to derive a ray-path geometry of a seismic wave. In order to calculate the traveltime between a source and a receiver one needs to predict the propagation of a seismic wave. Several methods have been developed and used to determine a propagation path. Here I only describe the overview of shooting, bending, pseudo-bending, and finite difference method.

The shooting method of ray tracing is based on solving the ray equation (equation 3.6) given the boundary conditions (source and receiver coordinates). The rays are shot through the medium from a source to a receiver. The shooting is iterated and the solution is achieved when the seismic ray reaches the receiver correctly (Fig. 3.1).

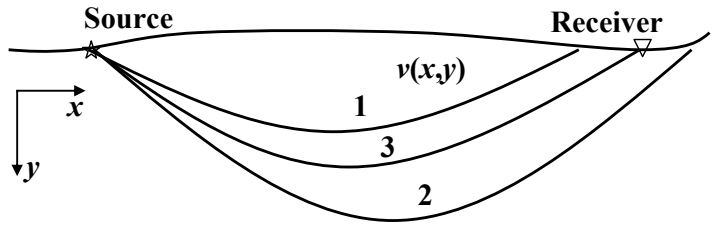

Figure 3.1: Shooting method scheme. The sketch is modified from Rawlinson and Sambridge (2003).

If the velocity block models are constant, at the boundary of cells the direction of refracted rays can be obtained by using Snell's Law:

$$\frac{\sin\theta_i}{v_i} = \frac{\sin\theta_r}{v_r} \tag{3.7}$$

where θ_i and θ_r are the incident and refracted angles of rays and v_i and v_r are the seismic velocities of the media that contain the incident and the refracted rays, respectively. For a 3-D structure, the ray-paths could be evaluated by solving the following set of equations (Sambridge and Kennett 1990):

$$\begin{aligned}
\frac{\partial x}{\partial t} &= v \sin i \cos j \\
\frac{\partial y}{\partial t} &= v \sin i \sin j \\
\frac{\partial z}{\partial t} &= v \cos i \\
\frac{\partial x}{\partial t} &= -\cos i \left(\frac{\partial v}{\partial x} \cos j + \frac{\partial v}{\partial y} \sin j \right) + \frac{\partial v}{\partial z} \sin i \\
\frac{\partial x}{\partial t} &= \frac{1}{\sin i} \left(\frac{\partial v}{\partial x} \sin j - \frac{\partial v}{\partial y} \cos j \right)
\end{aligned} \tag{3.8}$$

where i is the incident angle and j is the azimuth of the ray. Those coupled equations could be solved numerically by using the Runge-Kutta method. Having the solution of the ray-path the traveltime is determined by solving equation (3.4) numerically.

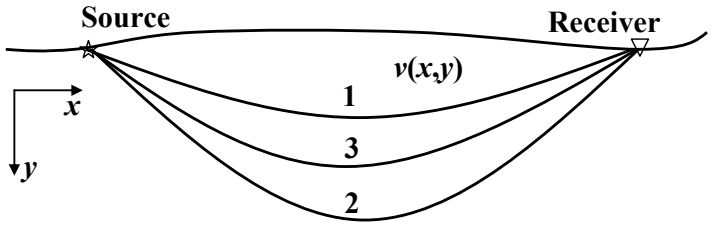

Figure 3.2: Bending scheme. The sketch is modified from Rawlinson and Sambridge (2003)

In the bending method, the initial ray-path between a source and a receiver is iteratively adjusted until the path satisfies Fermat's principle (Fig. 3.2) and the ray-path has an extremum time. The traveltime along the ray-path between a source and a receiver T_S^R is expressed by Julian and Gubbins (1977):

$$T_S^R = \int_S^R s dl \tag{3.9}$$

where $s = 1/v$ is the slowness and dl is the small segment of the arc length l. If the ray-path is a function of q (Cartesian coordinate can be expressed as $\mathbf{x} = x(q)+y(q)+z(q)$) then (Julian and Gubbins, 1977):

$$\frac{dl}{dq} = (\dot{x} + \dot{y} + \dot{z})^{\frac{1}{2}} \equiv F \tag{3.10}$$

where $\dot{x}$, $\dot{y}$, $\dot{z}$ are the differentials of the position with respect to q. In this case $q = l/L$ where L is the total length of the source-receiver path. The traveltime can be expressed as:

$$T_S^R = \int_{qS}^{qR} sF dq \tag{3.11}$$

The traveltime can be solved by employing the calculus of variation to the following Euler-Lagrange equations:

$$\begin{aligned} &\frac{d}{dq}\frac{\partial}{\partial \dot{x}}(sF) = \frac{\partial}{\partial x}(sF) \\ &\frac{d}{dq}\frac{\partial}{\partial \dot{x}}(sF) = \frac{\partial}{\partial x}(sF) \\ &\frac{dF}{dq} = 0 \end{aligned} \tag{3.12}$$

If an initial path traversing between the source and the receiver is defined as $\mathbf{x}^0(q)$, then the updated ray-path might be expressed as:

$$\mathbf{x}^1(q) = \mathbf{x}^0(q) + \xi^0(q) \tag{3.13}$$

where $\xi^0(q)$ is the perturbation to the initial path. Although equation (3.12) is nonlinear, by substituting equation (3.13) into equation (3.12) then the resulting equations for $\xi^0(q)$ can be linearized and solved (see Julian and Gubbins, 1977). The procedure is iteratively repeated until the convergence is achieved.

Um and Thurber (1987) introduced a faster method of ray tracing called pseudo-bending. In this technique, the ray-path is divided into multiple integration steps (Fig. 3.3). The path between a source and a receiver is initially estimated by an interpolated three point path. The center point of these points is then updated until the minimum traveltime is obtained. The paths between two points are then divided by half and all center points of all new and smaller paths are updated. The procedure is iteratively repeated until the change in traveltime satisfies some convergence critera.

Vidale (1988) applied a finite difference method to determine the traveltime reaching velocity nodes of a square grid parameterized region (See Fig. 3.4). For a 2-D grid with the slowness $s(x,z)$, the Eikonal equation (equation 3.6) can be written as:

$$\left(\frac{\partial t}{\partial x}\right) + \left(\frac{\partial t}{\partial z}\right) = [s(x,z)]^2 \tag{3.14}$$

where t is the traveltime of the wave propagation. If the traveltime to point A is known as t_A then the time for a seismic wave to travel to points B_i can be calculated by:

$$t_{B_i} = t_A + \frac{h}{2}(s_{B_i} + s_A) \tag{3.15}$$

where h is the distance among nodes and $s_{B_i}$and s_A are the slowness at nodes B_i and A, respectively.

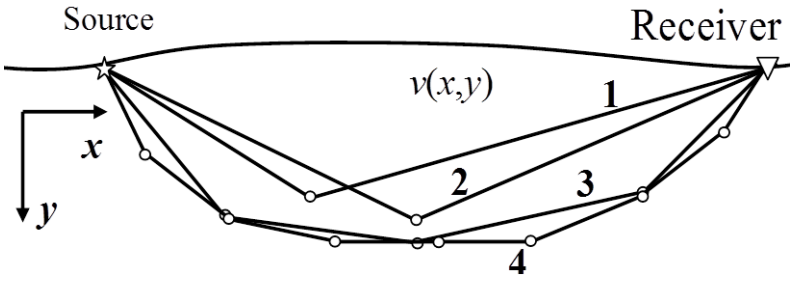

Figure 3.3: Pseudo-bending scheme. The sketch is modified from Rawlinson and Sambridge (2003).

If t_{B_1}, t_{B_2}, and t_{C_1} are the traveltimes at points B_1, B_2, and C_1, the Eikonal equation can be expressed as:

$$\begin{aligned} \frac{\partial T}{\partial x} &= \frac{1}{h}\left(t_{B_1} + t_{C_1} - t_A - t_{B_2}\right) \\ \frac{\partial T}{\partial z} &= \frac{1}{h}\left(t_{B_2} + t_{C_1} - t_A - t_{B_1}\right) \end{aligned} \tag{3.16}$$

If equation (3.16) is substituted into equation (3.14) then t_{C_1} can be obtained by:

$$t_{C_1} = t_A + \sqrt{2(h\bar{s})^2 - (t_{B_2} - t_{B_1})^2} \tag{3.17}$$

Following the above procedures, all traveltimes of all nodes t_{B_i} and t_{C_i} can be determined.

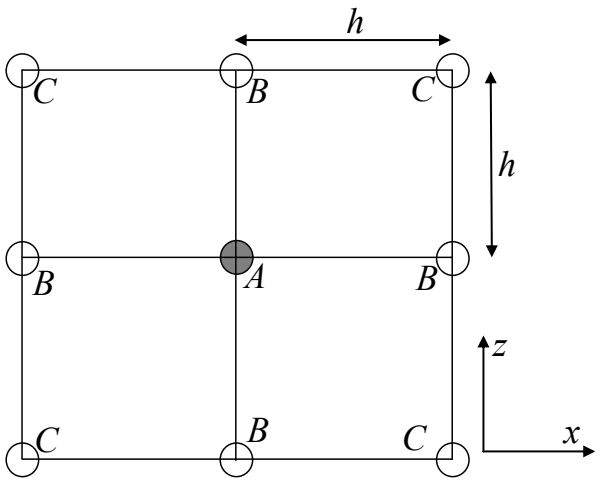

Figure 3.4: Finite difference method to find first arrival traveltime for a continuous velocity medium. The sketch is modified from Rawlinson and Sambridge (2003).

3.2.2 Inversion methods

In seismic tomography the inversion step is used to find the model parameters $\mathbf{m}$ satisfying the observed data $\mathbf{d}_{obs}$ related by a nonlinear function $\mathbf{g}$ as expressed by:

$$\mathbf{d} = \mathbf{g}(\mathbf{m}) \tag{3.18}$$

There are several approaches which have been used to solve equation (3.18). Backprojection methods are among the first methods used in seismic tomography originating from medical imaging. There are two types of back projection methods which are the Algebraic Reconstruction Technique (ART) introduced by Gordon et al. (1970) and the Simultaneous Iterative Reconstruction Technique (SIRT) developed by Gilbert (1972). ART has been used in cross-hole tomography by McMechan (1983) and in local earthquake tomography by Nakanishi and Yamaguchi (1986). The most commonly used inversion technique is the Damped Least Squares method (DLSQ). SIMUL2000, the code I use to perform a simultaneous 3D inversion for velocity model and hypocenter determination is based on DLSQ for the inversion. Fully nonlinear inversion methods have also been developed and used in seismic tomography (e.g., Sambridge and Mosegaard, 2002; Mosegaard and Sambridge, 2002). The damped least squares inversion method is discussed in the next subsection.

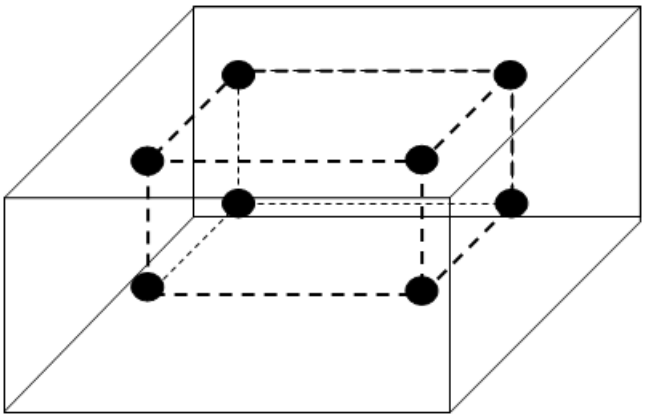

Figure 3.5: The scheme of a grid of nodes modified from Thurber (1993).

3.2.3 3D inversion for velocity model and hypocenter determination

In this work I apply a three dimensional simultaneous inversion package for velocity and hypocenter determination called SIMUL2000 (Eberhart-Phillips 1993; Thurber 1983, 1993). This method accounts for the nonlinear problem between velocity and earthquake location. The main objective of the method is to obtain the minimum misfit r_{ij} between the observed t_{ij}^{obs} and the calculated (predicted) arrival times t_{ij}^{cal} formulated as:

$$r_{ij} \quad = \quad t_{ij}^{\text{obs}} - t_{ij}^{\text{cal}} \tag{3.19}$$

Then the residuals of the linearized system can be written as (Thurber 1983):

$$r = \Delta t_e + \frac{\partial t}{\partial x_e}\Delta x_e + \frac{\partial t}{\partial y_e}\Delta y_e + \frac{\partial t}{\partial z_e}\Delta z_e + \sum_{n=1}^{N}\frac{\partial t}{\partial v_n}\Delta v_n \tag{3.20}$$

where Δt_e, Δx_e, Δy_e, Δz_e, and Δv_n are perturbations to the hypocentral parameters (earthquake origin time and location) and the velocity parameters, and $\partial t/\partial x_e$, $\partial t/\partial y_e$,$\partial t/\partial z_e$, and $\partial t/\partial v_n$ are the partial derivatives of arrival times with respect to the earthquake coordinates and velocity parameters.

The study area is parameterized by using a 3-D grid of nodes as shown in Fig. 3.5 which may be varied in vertical and horizontal directions. The velocity varies continuously in all directions with linear B-spline interpolation among nodes. The velocity at a certain point $V(x,\ y,\ z)$ is calculated by using an interpolation formula:

$$V(x,y,z) = \sum_{i=1}^{2}\sum_{j=1}^{2}\sum_{k=1}^{2} V(x_i,y_j,z_k) \left[\left(1-\left|\frac{x-x_i}{x_2-x_1}\right|\right)\left(1-\left|\frac{y-y_i}{y_2-y_1}\right|\right)\left(1-\left|\frac{z-z_k}{z_2-z_1}\right|\right)\right] \tag{3.21}$$

In SIMUL2000, the traveltimes are calculated by using an Approximate Ray Tracing (ART) method (Thurber, 1983). The minimum traveltime through a laterally averaged structure between a source and a receiver was estimated by using a 1-D ray tracer. A set of the ray-paths with radially varied curvature was constructed. The dips of the plane containing the paths are systematically adjusted. The ray-paths were then examined and the one with the shortest traveltime on the basis of the approximate traveltime is chosen as the true ray-path. The use of this method reduces the computational costs and improves the precision of the ray-paths.

To invert the traveltime residuals, equation (3.20) can be rewritten in a matrix notation:

$$\mathbf{d} = \mathbf{G}\mathbf{m} \tag{3.22}$$

where $\mathbf{d}$ is a matrix component of the residuals between observed and predicted traveltimes, $\mathbf{m}$ are the model parameters containing Δt, Δx, Δy, Δz, and Δv. $\mathbf{G}$ is a matrix containing the partial derivatives of traveltimes with respect to the model parameters. Equation (3.22) can be modified as (e.g., Menke, 1989; Stein and Wysession, 2009):

$$\mathbf{m}^{\text{est}} = \mathbf{G}^{-\text{g}}\mathbf{d} \tag{3.23}$$

where $\mathbf{G}^{-\text{g}}$ is a generalized inverse matrix of $\mathbf{G}$ which defined by:

$$\mathbf{G}^{-g} = (\mathbf{G}^T\mathbf{G})^{-1}\mathbf{G}^T \tag{3.24}$$

where $\mathbf{G}^T$ is a transpose matrix of $\mathbf{G}$**.** This approach accounts for an over-determined inverse problem.

However, a mixed determined (over-determined and under-determined) problem may occur in seismic tomography. To account for the problem a Damped Least Squares method is introduced (e.g., Menke, 1989; Stein and Wysession, 2009) formulated as:

$$\mathbf{m}^{\text{est}} = \left[\mathbf{G}^T\mathbf{G} + \epsilon^2\mathbf{I}\right]^{-1}\mathbf{G}^T\mathbf{d} \tag{3.25}$$

where ϵ^2 is a damping parameter and $\mathbf{I}$ is an identity matrix.

The application and results of the Vp and Vp/Vs tomography for the Tarutung region are described in Chapter 4. The quality of the tomography results was assessed by using synthetic models including checkerboard and characteristic feature tests. Additionally, spread function and resolution matrix analysis (Toomey and Foulger, 1989) is used to determine the resolution of nodes and the dependency of neighbouring nodes.

3.3 Attenuation tomography

Beside the Vp and Vp/Vs tomography, in this research I study the three dimensional upper crustal structure of the Tarutung geothermal region by using attenuation tomography. The seismic attenuation study enriches the understanding of the seismic structure of the region. Similar to traveltime tomography, attenuation tomography techniques are classified based on the path attenuation estimation and on the inversion of the seismic attenuation in three dimensions.

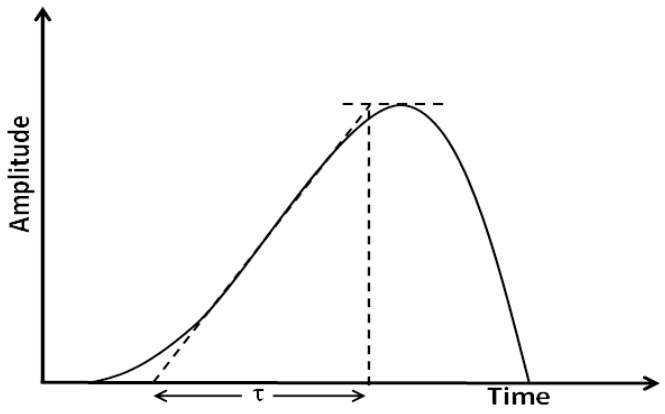

Figure 3.6: The description of rise time τ of a seismic wave defined as the tangent of the maximum slope of a seismic arrival pulse (after Gladwin and Stacey, 1974).

There are several ways to determine seismic attenuation along a ray-path. One method used to estimate the path attenuation is based on pulse rise time of seismic arrival pulses (Gladwin and Stacey, 1974). The pulse rise time is determined as the tangent of the point of maximum slope seismic arrivals as illustrated in Fig. 3.6. The relationship between seismic attenuation parameter Q and pulse rise time τ can be expressed as (Gladwin and Stacey, 1974):

$$\tau = \tau_0 + C \int_0^t Q^{-1} dt \tag{3.26}$$

where t is the traveltime, τ_0 is the initial rise time (at t=0) and C is a constant=0.53.

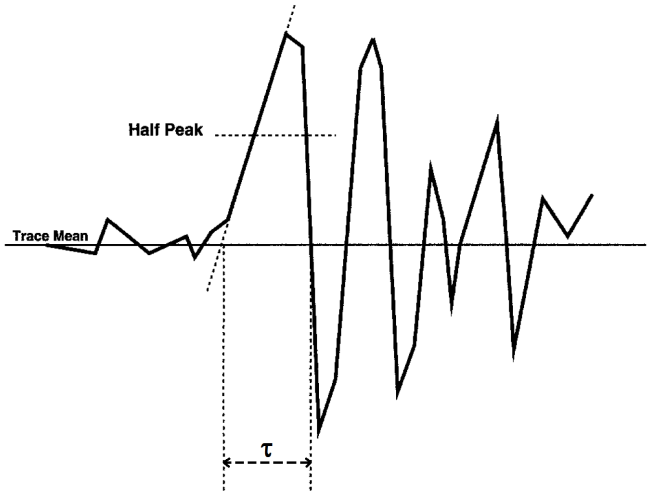

Figure 3.7: The pulse width is defined as the width of the half-peak of a seismic arrival (Wu and Lees, 1996).

Following the idea of Gladwin and Stacey (1974), Wu and Lees (1996) defined the pulse width τ as the width of the half-peak of a seismic arrival pulse as shown in Fig. 3.7. The seismic attenuation parameter Q along a seismic ray-path s can be obtained by inverting equation:

$$\tau - \tau_0 = C \int_{ray} \frac{1}{Qv} ds \tag{3.27}$$

where v is velocity of the seismic wave.

Another method for determining seismic attenuation is called frequency-shift method (Quan and Harris, 1997). The relationship between an amplitude spectrum of an incident seismic wave $S(f)$ and a recorded amplitude spectrum $R(f)$ could be expressed as (Quan and Harris, 1997):

$$R(f) = G(f)H(f)S(f) \tag{3.28}$$

The geometrical spreading, instrument response, source/receiver coupling, radiation patterns, and reflection/transmission factors are taken up in a fractor $G(f)$. The medium response $H(f)$ describing the attenuation effect along ray-path l may be defined as (Quan and Harris, 1997):

$$H(f) = \exp\left(-f \int_{ray} \alpha_0 dl\right) \tag{3.29}$$

The attenuation coefficient α_0 is influenced by the seismic attenuation parameter (quality factor) Q expressed as:

$$\alpha_0 = \frac{\pi}{Qv} \tag{3.30}$$

The combination of equation (3.28) and equation (3.29) provides:

$$\int_{ray} \alpha_0 dl = \frac{1}{f} \ln \left[\frac{GS(f)}{R(f)} \right] \tag{3.31}$$

If f_S is the centroid frequency of the input signal, f_R is the centroid frequency of the received signal, and σ_S is the variance of the centroid input frequency, the basic formula for attenuation tomography can be expressed as (Quan and Harris, 1997):

$$\sum_j \alpha_{oj}^i l_j^i = \frac{f_S - f_R^i}{\sigma_S^2} \tag{3.32}$$

where l_j^i is the length of i-th ray within the j-th block. The complete derivation of equation (3.32) can be found in Quan and Harris (1997). In this case the attenuation factor can be obtained by inverting equation (3.32). Having the velocity model v and the seismic coefficient α_0, the quality factor Q can be calculated.

In this study, I estimate the attenuation along the ray-path by using nonlinear spectral inversion following Rietbrock (2001), and Haberland and Rietbrock (2001). A nonlinear inversion/search method (Haberland, personal communication, 2013) was applied to determine the best fit between the synthetic and the observed spectra thus estimating signal moment, source corner frequency, and the path-averaged attenuation t^*. This method has similarly applied by Bohm et al. (2013). The 3-D quality factor Q is obtained by inverting for the attenuation parameter along the path t^*. The tomographic inversion procedure was similar to the one used for traveltime tomography. The detailed procedure of the path attenuation estimation, the inversion for the 3-D attenuation structure, and the interpretation of the attenuation tomography results of the Tarutung region are explained in Chapter 5.

3.4 Double-difference relocation

The double-difference relocation scheme is based on the measure of the traveltime differences among neighbouring events. The main idea of the method is to minimize the errors of earthquake locations caused by the lack of structure knowledge by using a relative relocation method. If the distance between two events recorded by the same station is much smaller than the source-receiver distance and the size of velocity het-

erogeneity then the ray-paths of those two events could be considered to be identical (Fig. 3.8). The change in hypocentral distance between two events i and j recorded by the same station k is obtained by (Waldhauser and Ellsworth, 2000):

$$\frac{\partial t_k^i}{\partial x}\triangle x^i+\frac{\partial t_k^i}{\partial y}\triangle y^i+\frac{\partial t_k^i}{\partial z}\triangle z^i+\triangle\tau^i-\frac{\partial t_k^j}{\partial x}\triangle x^j-\frac{\partial t_k^j}{\partial y}\triangle y^j-\frac{\partial t_k^j}{\partial z}\triangle z^j-\triangle\tau^j=dr_k^{ij} \quad (3.33)$$

where $dr_k^{ij}=\left(t_k^i-t_k^j\right)^{\text{obs}}-\left(t_k^i-t_k^j\right)^{\text{cal}}$ is the residual between observed and calculated traveltime between the two events which is also called double-difference. The partial derivatives of traveltimes t with respect to hypocentral coordinates (x, y, z) are the components of the slowness vector of the source-receiver ray-path. We should notice that in equation (3.33) the source is actually the centroid of the two hypocenters. In this scheme, $\triangle x, \triangle y, \triangle z, \triangle\tau$ are the changes required in the hypocentral parameters to make the model better fit the data. For all event pairs and all stations, equation (3.33) forms a system of linear equations that could be expressed in a matrix notation as follows (Waldhauser and Ellsworth, 2000):

$$\mathbf{WGm}=\mathbf{Wd} \quad (3.34)$$

where $\mathbf{W}$ is a diagonal matrix to weight each equation, $\mathbf{G}$ is an $M\times 4N$ matrix (M=number of double-difference observations; N=number of earthquakes) containing the partial derivatives, $\mathbf{d}$ is the double-difference vector, and $\mathbf{m}$ is a $4N$ size matrix of the length vector containing the deviation of hypocentral parameters needed to be determined $[\triangle x, \triangle y, \triangle z, \triangle\tau]^T$.

For small clusters and well-conditioned systems equation (3.34) could be solved by using the singular value decomposition (SVD) method. However, since the system to be solved becomes larger, the SVD method is not efficient. Therefore, the conjugate gradient algorithm LSQR (Paige and Saunders, 1982) is used to take into account for the sparseness of the matrix system. The inversion is applied to obtain the changes in hypocentral parameters and then the locations, the residuals, and the partial derivative in G are updated. An iterative inversion procedure is applied until a stable solution is achieved. In the iteration steps one could choose to use the SVD method for the first 3 iterations and then use the LSQR method. The application of the double-difference relocation method is used to study the detailed fault structure of the Tarutung pull-apart basin as described in Chapter 6.

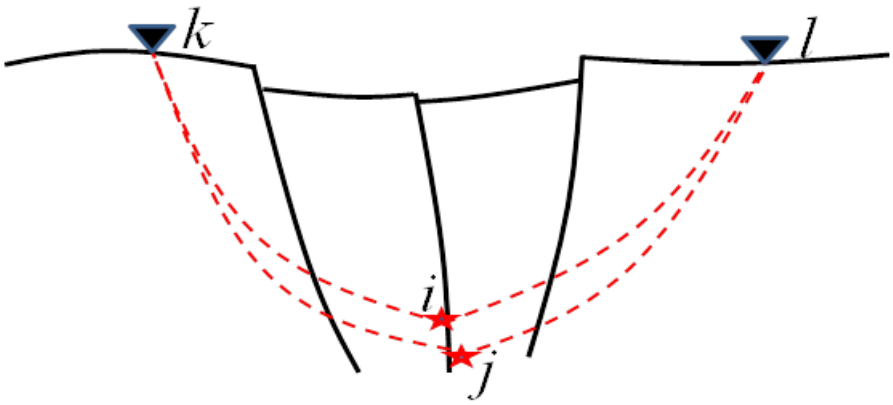

Figure 3.8: The illustration of two events (event-i and j) recorded by the same stations. The entire ray-path could be consider to be identical.

3.5 Focal mechanism

There are several ways used to determine the focal mechanism of earthquakes. One could evaluate the misfit between the observed and the synthetic source waveforms (Sipkin, 1994). This technique works best for broadband waveforms of long-period teleseismic data. Another method is called FOCMEC (Snoke et al., 1984) which determines the focal mechanism from P polarities and/or amplitude among P, SV, and SH). This method has been applied to study the focal mechanism of local and regional earthquakes. Another widely used, phase arrival based, focal mechanism determination method is called HASH (Hardebeck and Shearer, 2002). This technique is the improvement of the previous first polarity based focal mechanism method called FPFIT (Reasenberg and Oppenheimer, 1985).

The main aim of the inversion in the programs FPFIT and HASH is to obtain the double-couple fault-plane solution (source model) that fits well the observed phase motion polarities of a seismic event. Having azimuth and take-off angle leaving a source and passing a given velocity structure to seismic stations, the predicted first motion-polarities at stations are calculated for various source models. The source model is chosen as the solution when the calculated polarities fit best the observed ones. For each earthquake, E_j, the polarities at the k-th station caused by all possible source models M_i are calculated Aki and Richards (1980). A misfit function, $F_{i,j}$ between the observed and calculated polarities is defined by (Reasenberg and Oppenheimer, 1985):

$$F_{ij} = \frac{\sum\limits_{k} \left\{ \left| P_0^{j,k} - P_t^{i,k} \right| . W_0^{j,k} . W_t^{i,k} \right\}}{\sum\limits_{k} \left\{ W_0^{j,k} . W_t^{i,k} \right\}} \tag{3.35}$$

where $P_0^{j,k}$ and $P_t^{i,k}$ are the observed and the theoretical first motion polarities, respectively. $W_0^{j,k}$ is the observation weight assigned to the data and $W_t^{i,k}$ defined by:

$$W_t^{i,k} = [A(i,k)]^{1/2} \tag{3.36}$$

where $A(i,k)$ is the normalized theoretical P-wave radiation amplitude at the k-th station for a source model M_i.

In this study I use the HASH code (Hardebeck and Shearer, 2002) to determine the focal mechanisms of earthquakes in the Tarutung geothermal area (see Chapter 6). As some possible errors could occur in the determination of the hypocenters, the velocity models, and the first-motion polarities, HASH offers the possibility to conduct multiple trials for different source locations and velocity models. I used a well-defined 3D model and earthquake locations to calculate the take-off angles by using the SIMUL2000 program (explained in Chapter 4). The code provides focal mechanisms of a set of acceptable solutions and returns the average of the set of the solutions as the preferred solution including the strike, slip, and dip of earthquakes. It also includes the statistics of all provided solutions.

Chapter 4

Seismic Vp and Vp/Vs structure of the geothermal area around Tarutung (North Sumatra, Indonesia) derived from local earthquake tomography

Muksin[a,b], Klaus Bauer[a], Christian Haberland[a]

[a]German Research Centre for Geosciences GFZ, Potsdam, Germany
[b]Department of Physics, Syiah Kuala University, Banda Aceh, Indonesia
Contact: muksin@gfz-potsdam.de

Published 2014 in Journal of Volcanology and Geophysical Research, 260, pp. 27-42

Abstract

A passive seismic experiment with 42 short-period stations was setup for 10 months from May 2011 within a 20-30 km radius covering the Tarutung basin and the northern part of the Sarulla graben along the seismically active Sumatran fault (North Sumatra, Indonesia). The objective of the project is to investigate the geothermal setting based on the Vp and Vp/Vs structures and the distribution of seismicity. We recorded 2,856 local earthquakes by at least 8 stations which were reduced to 809 events having gap angle less than 180 degree. The initial earthquake locations were determined using simultaneous inversion for hypocenters and 1D velocity structure followed by 3D tomographic inversion. The resulting seismicity distribution, Vp and Vp/Vs structure reveal systematic differences between the Tarutung basin and the Sarulla graben. The Tarutung pull-apart basin is characterized by a complex structure reflected by a broader distribution of seismicity compared with the very narrow, rather vertical hypocenter distribution in the Sarulla graben, which was formed by fault-perpendicular extension and not by pull-apart tectonics. High Vp/Vs values near to the surface are imaged within the Sarulla graben and northeast of the Tarutung basin. These features are interpreted as fluid bearing sediments with fracturing indicating potentially favorable conditions for geothermal exploitation. The localized fluid flow northeast of Tarutung could be explained by the releasing step-over structure of the pull-apart basin and resulting dilatational stress regime in this part

of the basin. Heat sources are assumed to be located at greater depth in association with magmatic activities accompanying the subduction process, and the heat is transported along the Sumatran fault to shallow depth.

Keywords: Sumatran fault, local seismicity, P and S velocity structure, geothermal exploration.

4.1 Introduction

As Indonesia is one of the countries with the largest geothermal potential, the Indonesian government together with contracted companies developed power plants using geothermal energy in Sibayak and Sarulla (Sumatra), Wayang Windu, Kamojang and Dieng (Java), and Lahendong (Sulawesi), among others. The Center for Geological Resources, the Indonesian governmental agency for geothermal exploration, proposes Tarutung (Fig. 4.1) as one of several potential target regions for the future extension of geothermal exploration and exploitation. Tarutung is located in northern Sumatra and is characterized by a pull-apart basin structure formed along the Sumatran fault (Bellier and Sébrier, 1994). Geothermal potential is expected at this site because of geotectonic similarities with the already productive area around the Sarulla basin located approximately 30 km south of Tarutung. Initial exploration activities were undertaken under the guidance of Badan Geologi including magnetotelluric (MT) measurements and geological analysis covering mainly the northern part of the Tarutung basin (e.g. Niasari et al., 2012).

Since Tarutung and Sarulla are seismically active regions, we make use of these local earthquake sources and apply seismological methods to investigate the geological structure in the geothermal area as have been recently used by some authors (e.g. Chatterjee et al., 1985; Foulger, 1982; Jousset et al., 2011; Toomey and Foulger, 1989; Walck, 1988). Passive seismic methods provide the Vp and Vp/Vs structure (Poisson's ratio) which is related to lithology and to the characteristics of reservoirs.

Seismic properties (Vp and Vp/Vs) of a study area could reflect the properties of rocks, fluid and gas content, and lithology although they are influenced by variations of pressure, temperature, saturation, fluid type, porosity, and pore type in a complex way. Some authors, e. g. Haberland and Rietbrock (2001) and Zucca et al. (1994), applied attenuation tomography for compressional and shear waves to understand water saturation, pressure, temperature, characteristic of gas, and partial melting. The result of a passive seismic experiment for geothermal exploration could also be used as the base-line for monitoring of the production process. In this paper, we

describe a new passive seismic experiment in the Tarutung area (northern Sumatra, Indonesia) and derive the Vp and Vp/Vs structure and the seismicity distribution using high quality local earthquake data. We investigate the lithology in relation to the seismic properties and compare the results with the previous geophysical studies.

A pattern recognition analysis (Bauer et al., 2012) is performed to classify dominant features found within the Vp and Vp/Vs tomography images and to characterize these clusters by their dominant physical properties. Integration of different results such as Vp, Vp/Vs and seismicity distribution finally allows us to develop conceptual models for the Tarutung and Sarulla regions.

4.2 Geological, tectonic and geophysical setting

Tarutung and Sarulla are part of the North Tapanuli district which is located along the Sumatran fault further south of the Lake Toba (Fig. 4.1). The 1,900 km long dextral slip Sumatran fault accommodates a significant amount of the trench-parallel component of the oblique convergence between the Indo-Australian and Eurasian plates (Bellier and Sébrier, 1994; McCaffrey, 2009; Sieh and Natawidjaja, 2000). The change of rate and direction of the Indo-Australian plate motion causes the right step-over segmentation of the Sumatran fault (Sieh and Natawidjaja, 2000) which is responsible for the presence of the Tarutung pull-apart basin. In more detail, Bellier and Sébrier (1994) suggested that the Tarutung basin was formed when a new branch of the Sumatran fault was developing at the western flank of the Toba caldera as a consequence of a larger step-over of the previous fault system and subsequent formation of the great Toba caldera within this older step-over region. The Sarulla graben located south of Tarutung, on the other hand, is not a typical pull-apart basin, which was formed in a more complex setting. Following Hickman et al. (2004) the asymmetrical architecture of the Sarulla basin is related to the normal extension of the strands along the strike-slip zone. Analysing local seismicity, Weller et al. (2012) noticed the formation of strike-slip duplexes along the Sumatran Fault.

Another main feature of the Sumatran Fault System is the collocation with the volcanic arc including calderas in direct proximity to the fault. In general, the position of the volcanic arcs correlates with the geometry of the subduction zone (e.g. Tatsumi, 1989). In subduction zones with oblique convergence, prominent trench-parallel strike-slip fault systems often develop within the the magmatic arc.

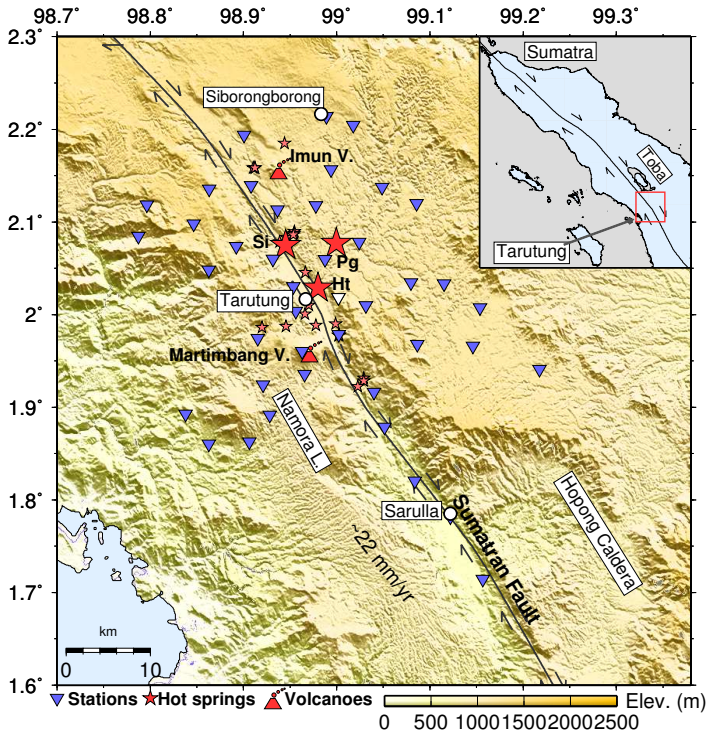

Figure 4.1: Tarutung area located in the south of Lake Toba characterized by the presence of the Tarutung pull-apart basin, Sarulla graben, Hopong caldera, Namora Langit field dome Martimbang and Imun volcano, and also geothermal manifestations (hot springs). Three big manifestations (indicated by the bigger red stars) called Panabungan (Pg), Sipoholon (Si), and Hutabarat (Ht). The seismic instruments (blue triangles) were deployed covering the area of Tarutung and Sarulla. The white triangle indicates the reference station used for inversion.

This is for example the case in the South-Chilean subduction zone, where the Liquene-Ofqui Fault Zone accommodates the northward motion of a continental forearc sliver relative to the South-American continent (Cembrano et al., 1996; Lange et al., 2010), or at the western margin of North America, where the San Andreas Fault System takes up most of the shear component (Teyssier et al., 1995). In Sumatra, the trench-parallel Sumatran fault is also collocated with arc volcanic centers, however, this might be pure coincidence (Sieh and Natawidjaja, 2000). Regardless of the causal dependencies of volcanism and fault development it appears reasonable that inter-relations between magmatic processes and the tectonic behavior of the fault exist, and they are important for the understanding of the geothermal system. Bellier and Sébrier (1994) argued in the mechanical weak area there is a close relation between the quaternary volcanic center and the Sumatran fault. Along the Tarutung area, there are three volcanoes located close to the fault line which are Imun, Helatoba, and Dolok Martimbang volcanoes as indicated by the red triangles in Fig. 4.1. Along the

Sarulla region, some volcanic related activity is observed such as the Namora-I-Langit dome field (northern of Sarulla) and the 9 km-diameter Hopong caldera located on the eastern side of Sarulla graben (Hickman et al., 2004). Along the Sumatran fault, one half of the hot fluid discharges is associated with the pull-apart basins and the other half is associated with the volcanic activity (Muraoka et al., 2010). Since there are many volcanoes and calderas close to the pull-apart basins and the graben, both, the basins and the volcanic activity together could play important roles in controlling the geothermal system.

Some previous seismological investigations were conducted in northern Sumatra including also the Tarutung area but the focus of these studies was on the larger-scale crustal structure of the Toba region (e. g. Koulakov et al., 2009; Stankiewicz et al., 2010b) and on the crustal and lithospheric structure of the subducted Investigator Fracture Zone (e.g. Weller et al., 2012). Seismicity recorded by regional stations is shown in Fig. 4.1, where earthquakes at depths shallower than 30 km with magnitudes of up to Mb 6.6 (USGS National Earthquake Information Center, 2012) are plotted as red circles. Using local traveltime tomography, Koulakov et al. (2009) found low and high Vp/Vs anomalies along the Tarutung and Sarulla basins. However, for the geothermal exploration purposes, this model was relatively coarsely parameterized both in horizontal and vertical direction and included only three stations around the Tarutung and Sarulla basins. Ambient noise tomography of the Toba region (Stankiewicz et al., 2010b) provided surface wave velocity images derived for distinct periods and corresponding pseudo-depth ranges. Following this investigation the Lake Toba is underlain by low surface wave velocity material most likely associated with remnants of magmatic bodies of the great Toba eruption 75 ka (e.g. Rose and Chesner, 1987), in agreement with the body wave tomography results of Koulakov et al. (2009). While Tarutung was partly covered by the network used by Stankiewicz et al. (2010b), the station distribution and ray coverage were not dense enough to resolve local features within our study area. Our new microseismic study with a dense network installed over a comparably small area provides structural images of seismic properties and the seismicity distribution, both improving the understanding of the tectonic setting and the geothermal system.

4.3 Experiment and data

The temporary network consisted of 42 short period seismic instruments deployed in the Tarutung and Sarulla region from mid of May 2011 to mid of February 2012 (Fig. 4.1). We used 40 three component short period (1 Hz) sensors and recorded

the signals using the PR6-24 Earth Data Logger (EDL) sampling at 100 sps. After two months we added two more stations equipped with 3 component 4.5Hz geophones and DSS CUBE data logger (Omnirecs) recording data with 100 sps to improve the coverage south of Tarutung where earthquakes occur frequently in the southernmost part of the Sarulla basin. The network covered the entire district of North Tapanuli along the mega fault between 1.71 N to 2.21 N and 98.79 E to 99.22 E with an average station spacing of around 5 km.

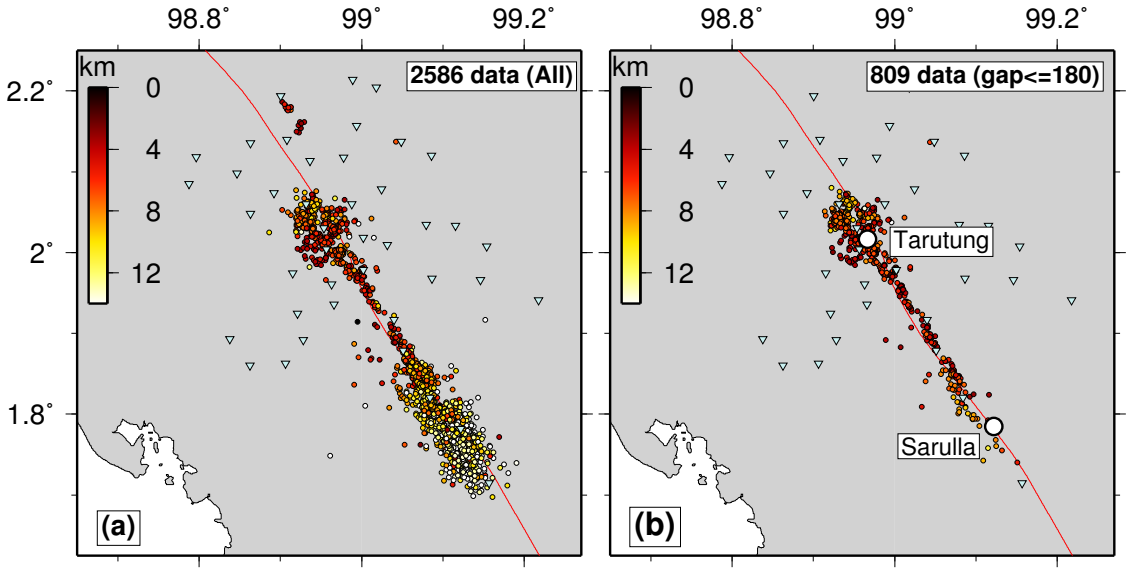

Figure 4.2: (a) Distribution of all local earthquakes recorded by the stations and located using HYPO71. (b) All events located within the network after application of the azimuthal gap criterion are shown (azimuthal gap smaller than 180 degrees).

The arrival times of direct P and S waves were detected using the optimized automatic picking routine of Nippress et al. (2010). We then manually revised the picking of the high quality waveforms (waveforms have a clear onset), excluded poor quality data and initially localized the events using HYPO71 (Lee and Valdes, 1985) based on a layered 1D velocity model modified from IASP91 (Kennett and Engdahl, 1991). The uncertainty of the P- and the S-arrivals are defined by the weighting factors of 0, 1, and 2 corresponding to the estimated picking uncertainty of 0.01 s, 0.05 s, and 0.1 s, respectively.

We recorded 2,586 events (Fig. 4.2a) along the Tarutung and Sarulla basins. However since the southernmost station did not work properly at all times, we had to exclude some more events with azimuthal gap angles larger than 180 degree, and which occurred at depths greater than 40 km. Another restriction is that we only used the events recorded by at least 8 stations which seems to be a good compromise between a

high data quantity (for reasonable model resolution) and required data quality. These constraints reduced the number of data to 809 events (Fig. 4.2b) containing 13,184 observed P and 5,922 S wave arrivals. This forms the catalog of initial hypocenters which is then successively used in the calculation of the minimum 1D model and the relocation of these hypocenters.

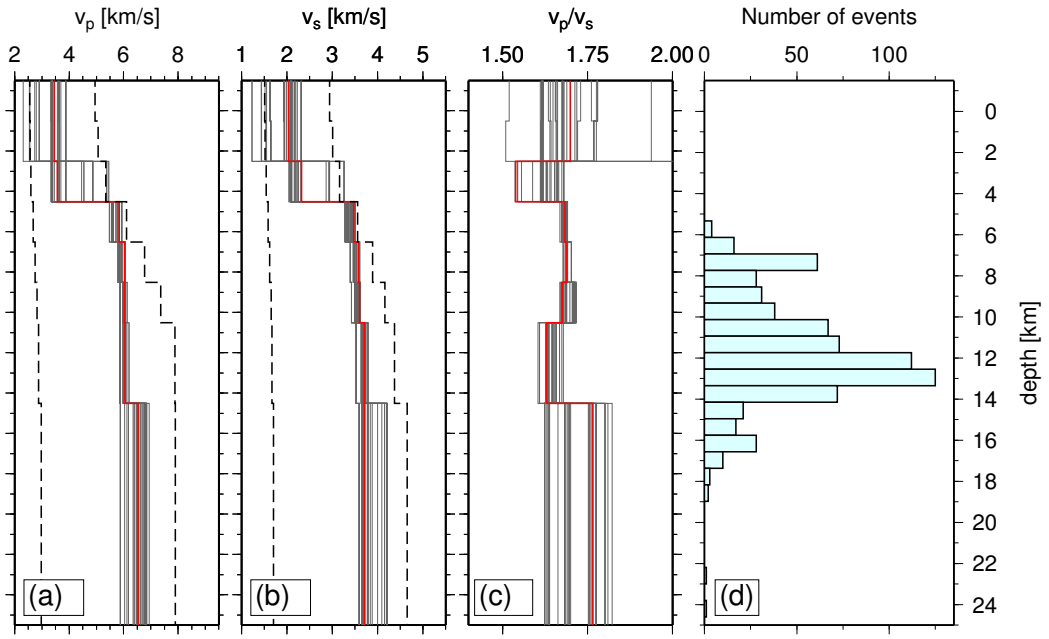

Figure 4.3: Results of 1D inversion using the VELEST software, showing (a) P velocity, (b) S velocity, and (c) Vp/Vs ratios as a function of depth. (d) Distribution of the hypocenters after the 1D inversion.

4.4 Methods of velocity modeling

The P and S wave traveltime data were used to develop Vp and Vp/Vs velocity models and to determine the seismicity distribution of local earthquakes. The work flow included (1) the inversion for the so-called minimum-1D-velocity model (Vp and Vp/Vs) and the relocation of hypocenters using the program code VELEST (Kissling et al., 1994), and (2) the simultaneous inversion for the 3D tomographic velocity structure (Vp and Vp/Vs) and the earthquake hypocenter using the program code SIMUL2000 (Eberhart-Phillips (1990); Eberhart-Phillips and Michael (1998); Evans et al. (1994); Thurber (1983)). The quality and uncertainty of the final results are investigated and discussed in the subsequent section.

The hypocenter locations from HYPO71 served as starting values for VELEST (Kissling et al., 1994), which was applied to relocate the hypocenters and simultaneously deter-

mine the 1D velocity model and the station corrections. For the inversion, we defined station X27 as the reference station (indicated by white triangle in Fig. 4.1) as it was located in the middle of the network and recorded the largest number of P and S arrivals.

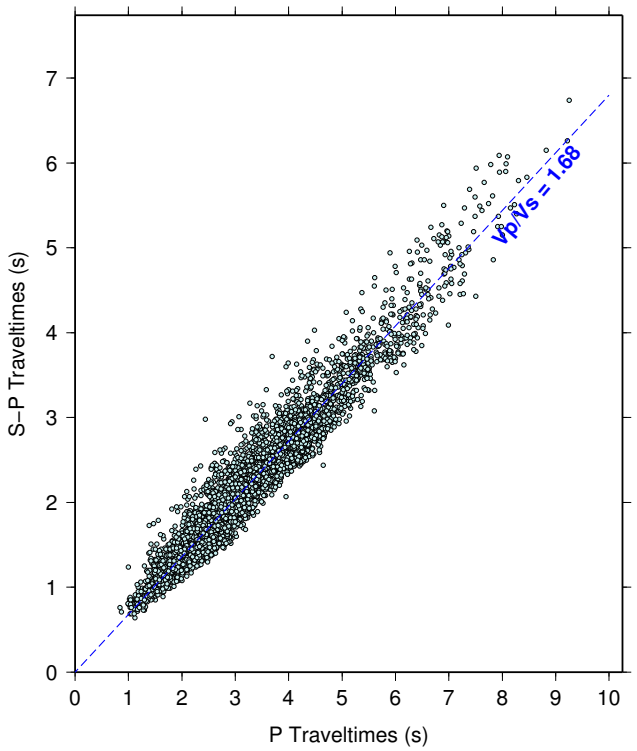

Figure 4.4: Wadati diagram showing P wave traveltimes plotted against differences between S and P wave traveltimes. The line fit provides an average Vp/Vs ratio of 1.68.

Ray tracing is performed to obtain the predicted traveltimes based on the initial velocity model. The inversion is then applied to adjust the 1D model, the hypocenter locations, and the station corrections. The forward calculation is re-applied using the new (inverted) velocity model and the new hypocenters, and the calculated and observed traveltimes are compared to calculate the RMS (root-mean-squared) misfit. This procedure is re-iterated by considering any possible combination of hypocenters, velocity models, and station corrections until the minimum RMS misfit of the solution is achieved. A Vp/Vs ratio of 1.68 used as initial value in the inversion was estimated from a modified Wadati diagram (Fig. 4.4). This value is smaller than the value of 1.77 determined by Weller et al. (2012) for the region South of our study area. On the other hand, Koulakov et al. (2009) obtained Vp/Vs values of 1.62 at 5 km depth for the Toba region including also parts our study area in a coarser model.

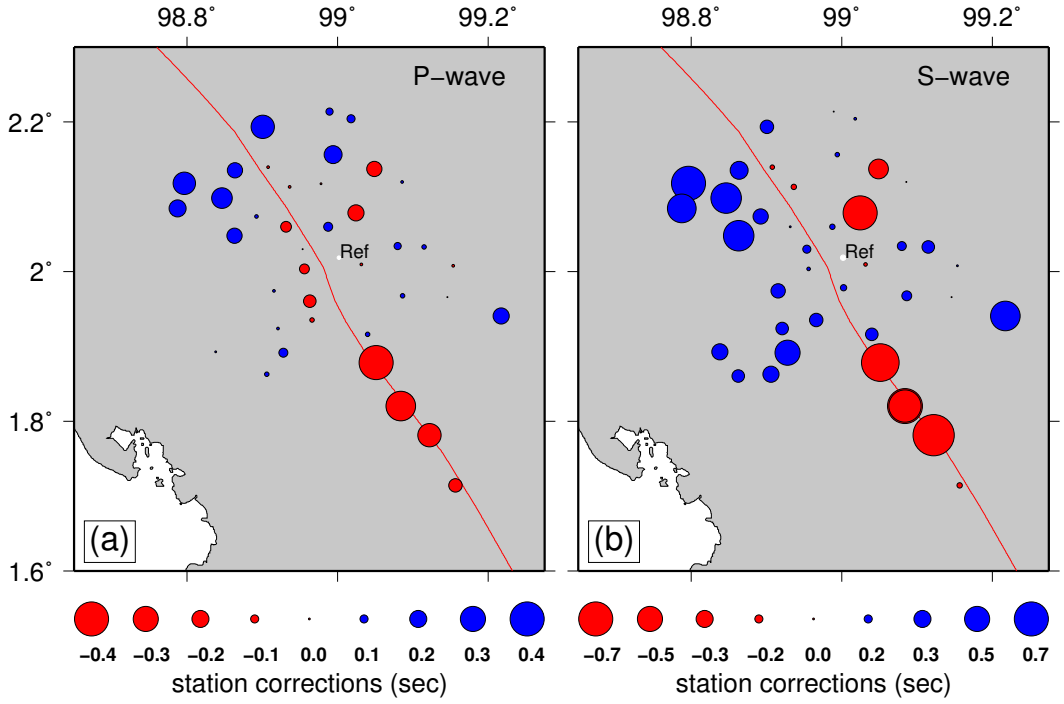

Figure 4.5: Station corrections (a) for P-waves and (b) for S-waves. The blue and the red circles represent positive and negative station corrections, respectively. The circle size correlates with the magnitude of the correction. The white dot indicates the reference station.

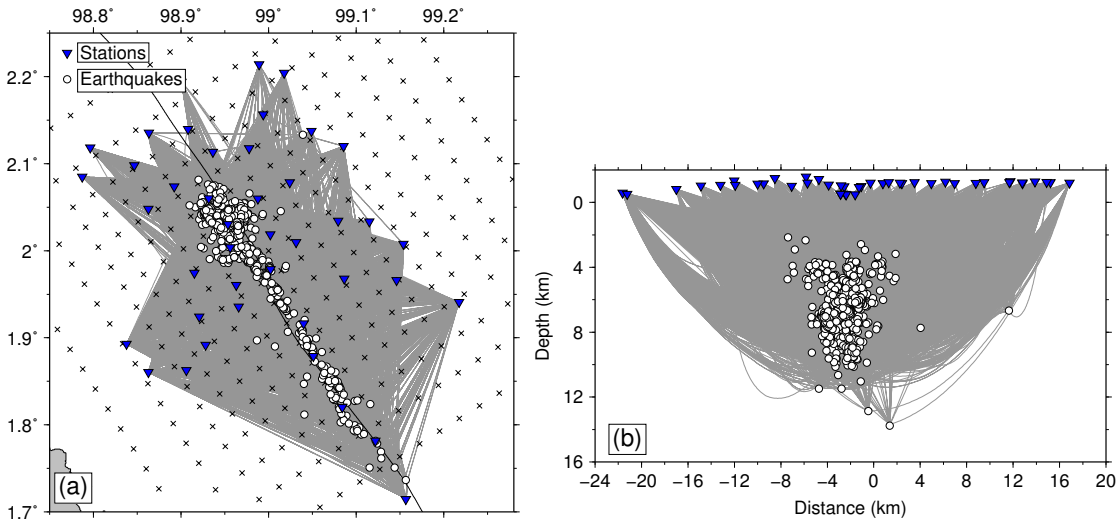

Figure 4.6: (a) The 3 x 3 km horizontal and (b) the 2 km vertical grid design used in the inversion. The stations (blue triagles) are connected to the hypocenters (white circles) by the gray ray-paths.

We imposed 45 initial 1D Vp models defined at depth nodes in 2 km intervals and determined the velocity for the S-wave using the average Vp/Vs value from the Wadati diagram analysis (see above). After the inversion, all inverted models from various initial models converge to the best global solution indicated by red lines in Fig. 4.3a, 4.3b, and 4.3c for Vp, Vs, and Vp/Vs, respectively. The data variance and the RMS residuals decrease from 0.1548 and 0.358 initially to 0.00644 and 0.0729 finally showing the reliability of the solution. The models are best resolved at $4 - 12$ km depth which is consistent with the hypocenter distribution as shown in Fig. 4.3d. The P-wave station corrections (Fig. 4.5a) show negative values (red circles) along the Sarulla and Tarutung basins which means that the stations along the basins mostly recorded delayed arrivals relative to the reference station X27. The negative values of the P-wave station corrections indicate the sediment coverage along the basins. Fig. 4.5b shows that the S-wave station correction is relatively balanced and stations along the Sarulla basin and in the northeast of Tarutung recorded S-wave arrivals later. We have experimented with some various possible sets of initial Vp functions (see Fig. 4.3) but at shallow depth all solutions of the 1D Vp models tend to be lower than 4.5 km/s.

To study the 3D velocity structure and relocate the hypocenters more precisely, we applied the well-recognized and commonly used 3D simultaneous inversion code SIMUL2000 (Eberhart-Phillips, 1990; Eberhart-Phillips and Michael, 1998; Evans et al., 1994; Thurber, 1983). The code allows the inversion for Vp and Vp/Vs instead of inversion for Vp and Vs because typically there are much smaller numbers of S-picks available compared to the number of P-picks thus the resolution of Vs is much lower than for Vp (Eberhart-Phillips, 1990). Furthermore, the Vp/Vs value and the corresponding Poisson's ratio are very sensitive to lithology, fracture density, and characteristic of fluids or gas which is important for understanding the geothermal system. The predicted ray-paths and traveltimes are calculated using an Approximate Ray Tracing (ART), and the residuals between the theoretical and the observed traveltimes are iteratively calculated using damped least-squares as described in Thurber (1983). At each iteration, the ray-paths, the hypocenters, and the velocity models are updated until a stable solution with a minimum RMS is achieved.

The best models and hypocenter locations obtained from the 1D inversion (VELEST; see above) are used as the initial values for the 3D simultaneous inversion. The area is rotated relative to the main Sumatran Fault, and the center of the region is chosen at 99.00 E and 2.00 N. The x-axis is set perpendicular to the Sumatran fault while the y-axis is set parallel. The region is laterally (in x- and y-direction) parameterized

by 3 x 3 km grid spacing, and by 2 km node spacing in depth direction (Fig. 4.6). The grid nodes spacing is set much coarser in the region outside of the network and deeper than 12 km since most earthquakes are located above this depth.

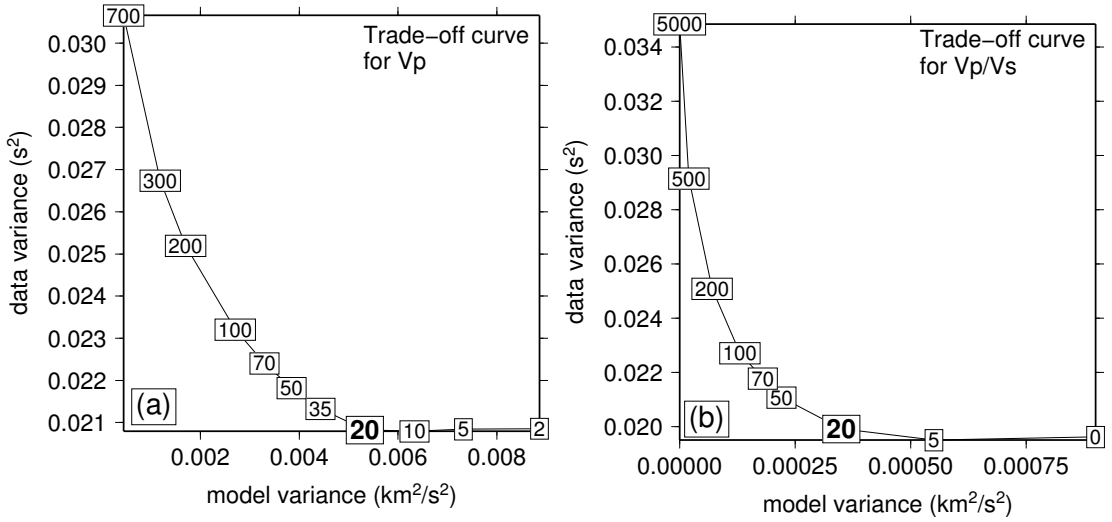

Figure 4.7: Trade off curve for (a) Vp and (b) Vp/Vs to determine optimal damping values. The damping values are chosen with 20 for both Vp and Vp/Vs as indicated by bold character.

The damping factors were empirically determined from the so-called trade-off curve between data and model variance (Eberhart-Phillips, 1986). The appropriate damping values were chosen where the data variance is minimized at a moderate model variance. To determine the damping factor for Vp, a large damping value for Vp/Vs is set fixed and a single-step inversion is conducted for various Vp damping values. After we obtain the appropriate damping value for Vp, we fixed this Vp damping and the similar procedure is performed by varying the Vp/Vs damping values. Regarding the result of this approach and several inversion tests, the appropriate damping factors are 20 for both the Vp and Vp/Vs inversion (Fig. 4.7).

4.5 Model quality and uncertainty

4.5.1 Resolution Matrix and Spread Function

The resolution of the inversion results is evaluated by the analysis of the model resolution matrix provided by the inversion code, and by the evaluation of the spread function which can be calculated from the model resolution matrix following the

procedure of Eberhart-Phillips and Michael (1998). The smearing information of each node provided by the resolution matrix is obtained by examining the relative size and pattern of the off-diagonal elements of the node. The spread function (described in more detail by Toomey and Foulger, 1989) accounts for both the sensitivity of each model parameter related with the size of the corresponding diagonal element within the model resolution matrix, and also for the dependency with neighboring model parameters represented by the pattern of the off-diagonal elements.

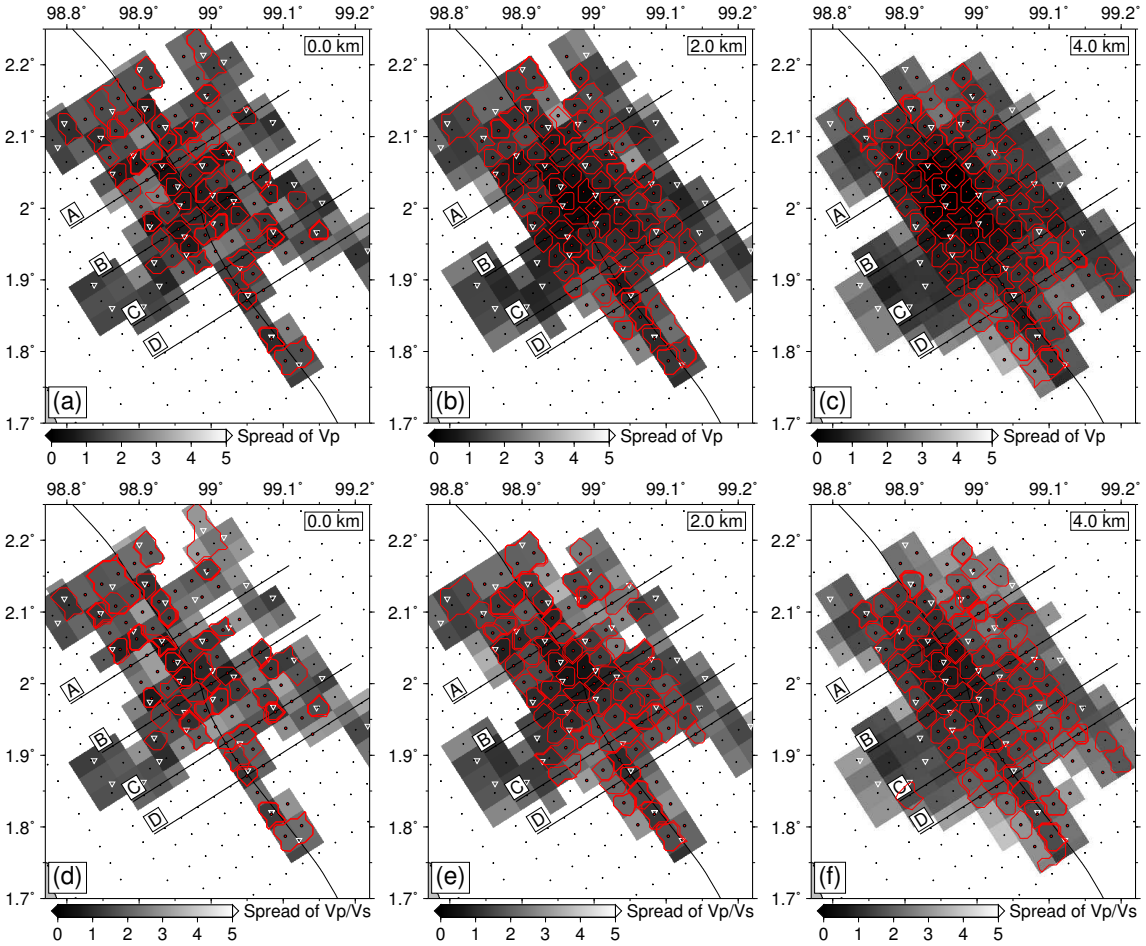

Figure 4.8: The horizontal layers of the spread values of the model at depth of 0, 2, and 6 km for Vp in (a), (b), and (c) and for Vp/Vs in (d), (e), and (f). The triangles represent the stations. The cross-sections A – D are related to the vertical spread values shown in Fig. 4.9. The red contour lines represent model resolution matrix.

Fig. 4.8 shows the spread values and the 70% model resolution matrix (indicated by the red contour lines) for horizontal layers of both the Vp (Fig. 4.8a – 4.8c) and the Vp/Vs models (Fig. 4.8d – 4.8f) at various depth. The spread values of the Vp and the Vp/Vs models are comparable but the Vp model seems to be slightly better

resolved and less smeared as indicated by the smaller spread values of Vp and more focused contour lines. At 0 km depth (Fig. 4.8a), the spread function is found patchy and smaller at the nodes close to stations because the rays tend to concentrate there.

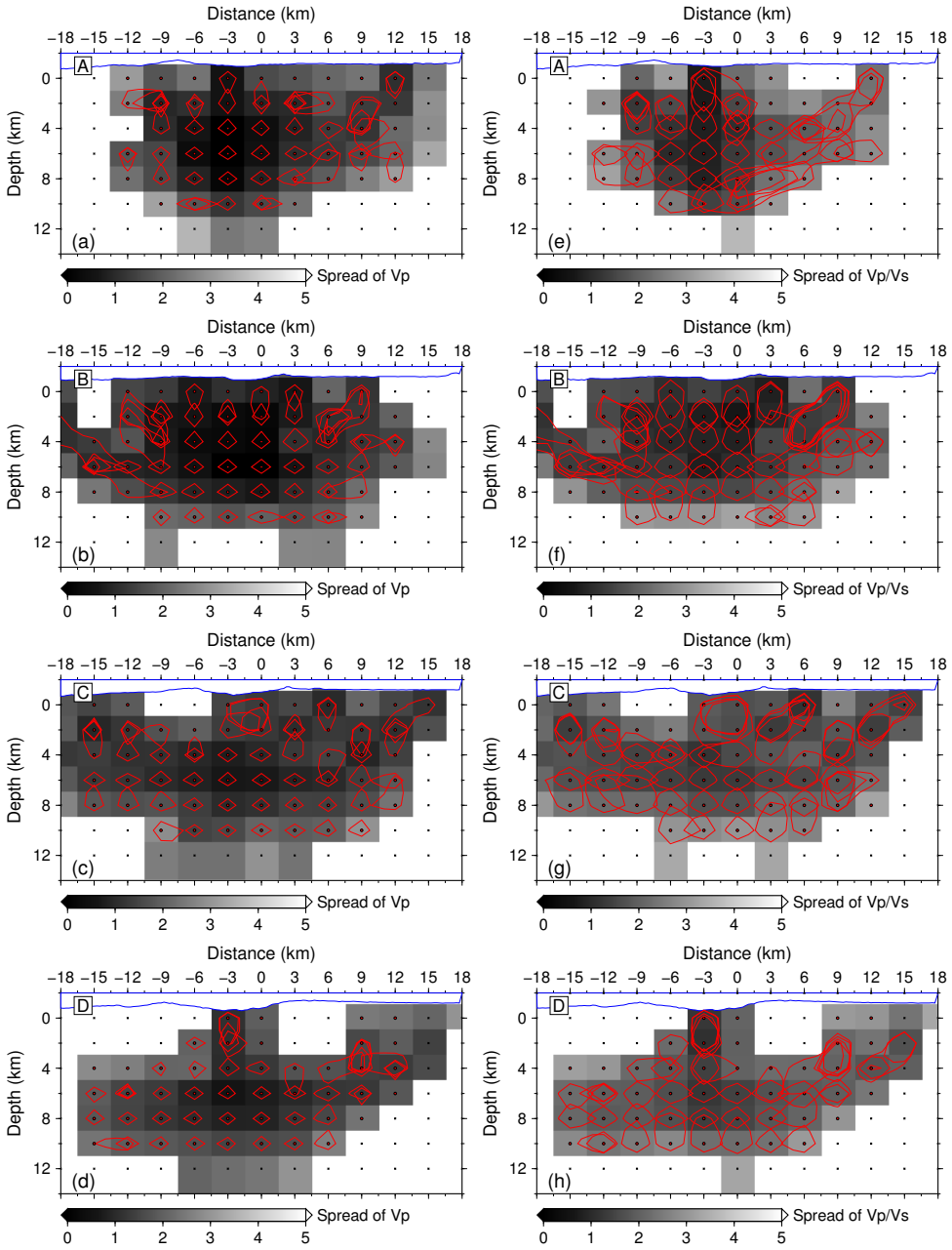

Figure 4.9: Vertical spread values for the Vp model along the cross-sections A - D in (a) - (d), and for the Vp/Vs model along the cross-sections A - D in (e) - (h). The cross-sections are taken perpendicular to the Sumatran fault shown in Fig. 4.8. The red contour lines represent model resolution matrix.

We found the horizontal smearing is relatively small compared to the vertical ones. At 2 km depth and deeper (Fig. 4.8b-c), the model is resolved better but further south

(Sarulla region) the model is resolved mainly along the fault which is in accordance with the distribution of stations and the events. Around Tarutung, the model is well resolved within 12 km distances to the left and to the right from the Sumatran fault line.

Fig. 4.9 shows the vertical spread values of Vp and Vp/Vs including the model resolution matrix along various cross-sections perpendicular to the fault as indicated in Fig. 4.8. The model is resolved at depths between 0 km and 10 km, where more smearing occurs in the Vp/Vs model than in the Vp model, especially in regions far from the fault line. The vertical spread values are generally below 3.0 and correlate with the high density of the rays. Due to the localization of the events and the stations along the Sarulla graben, above 3 km depth the model is only resolved along the fault as imaged along the cross-section D (Fig. 4.9d). In the Tarutung region, the model is well resolved around 12 km to the left or to the right of the fault and from 1 to 12 km in depth as indicated by the small spread values and small smearing effect along the cross-sections A, B, and C (Fig. 4.9a - 4.9c).

4.5.2 Recovery tests

In order to investigate which kind of anomalies could be reconstructed with our network geometry we carried out recovery tests for two different types of models: (1) checkerboard anomaly patterns and (2) models with characteristic features abstracted from our inversion results. For the first class of tests, the background model is perturbed by anomalies alternating with ± 15% against the background Vp and Vp/Vs, respectively. For the synthetic tests, we also re-determined the damping values for Vp and Vp/Vs and obtained almost identical values of damping to the real inversion.

The perturbations of ±15% are in agreement with our case study, where at shallow depth our Vp model range is 3.00-4.03 km/s while our Vp/Vs model range is 1.43-1.93. We produced two different types of checkerboards which contain 12 nodes and 8 nodes in each positive and negative anomaly. Positive and negative anomalies are indicated by red and blue colors, respectively.

Fig. 4.10 shows the horizontal view of the checkerboard of the Vp and Vp/Vs models at 2 km depth. The Vp and Vp/Vs models for the checkerboard containing 12 nodes in one anomaly are shown in Fig. 4.10a and 4.10b while Fig. 4.10c and d show those for the checkerboard containing 8 nodes in a checker block. Gaussian noise is added to the calculated traveltimes of P and S-P with the standard deviation of ±0.1 s in

accordance with the uncertainty of our manual picking.

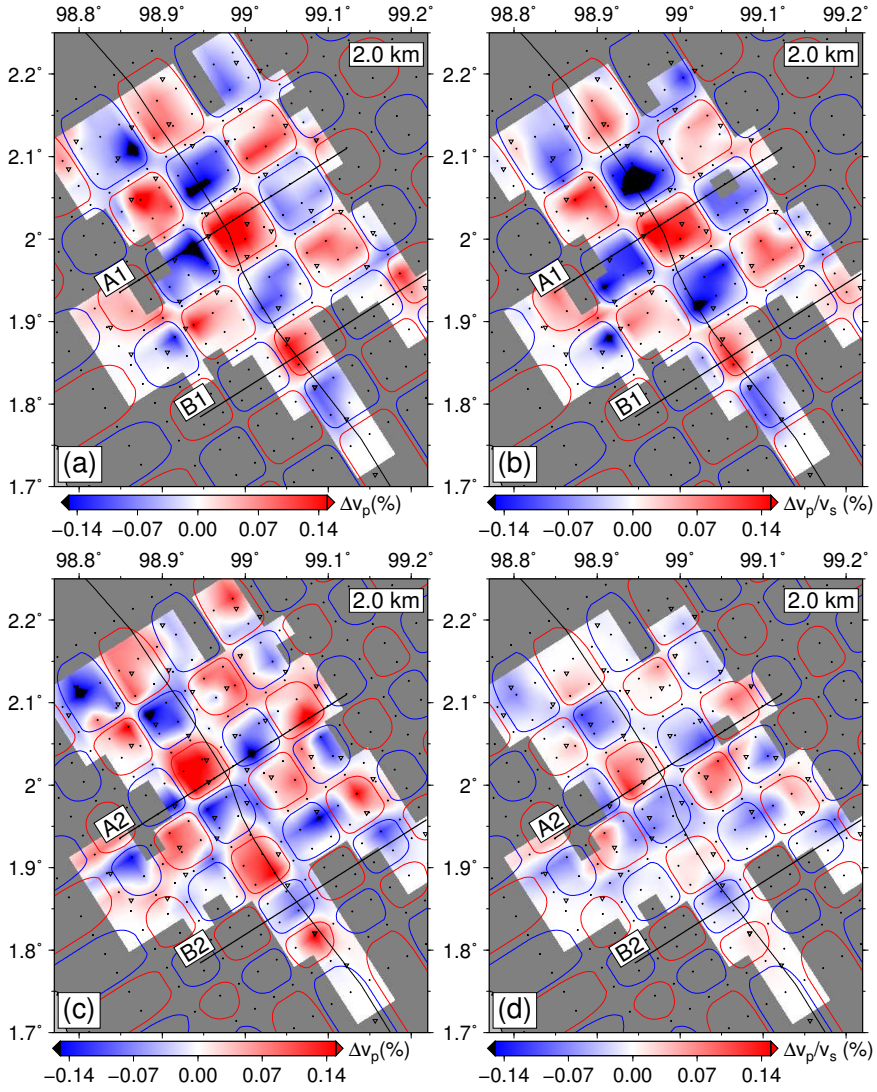

Figure 4.10: The map view of the checkerboard recovery at depth of 2 km for the model containing 12 nodes in each anomaly for (a) Vp and (b) Vp/Vs. The recovery of the checkerboard containing 8 nodes in an anomaly for (c) Vp and (d) Vp/Vs. The cross-sections A1 and B1 are related to the vertical model sections described in Fig. 4.11a-d and the cross-sections A2 and B2 are related to Fig. 4.11e-h The red and blue contour lines represent the high and low velocity anomalies.

The inversion is then conducted for both the Vp and the Vp/Vs with damping factors of 20 for both Vp and Vp/Vs as obtained from the trade-off curve analysis (Fig. 4.7) and as also used for the real inversion. In the area containing sufficient crossing rays, the checkerboard is well resolved both for Vp (Fig. 4.10a and Fig. 4.10c) and for Vp/Vs (Fig. 4.10b and d). The deeper part of the checkerboard pattern is better

resolved but at shallow depth, the checkerboard is reproduced well in the area close to the Sumatran fault since the earthquakes are concentrated along the fault particularly in the Sarulla region.

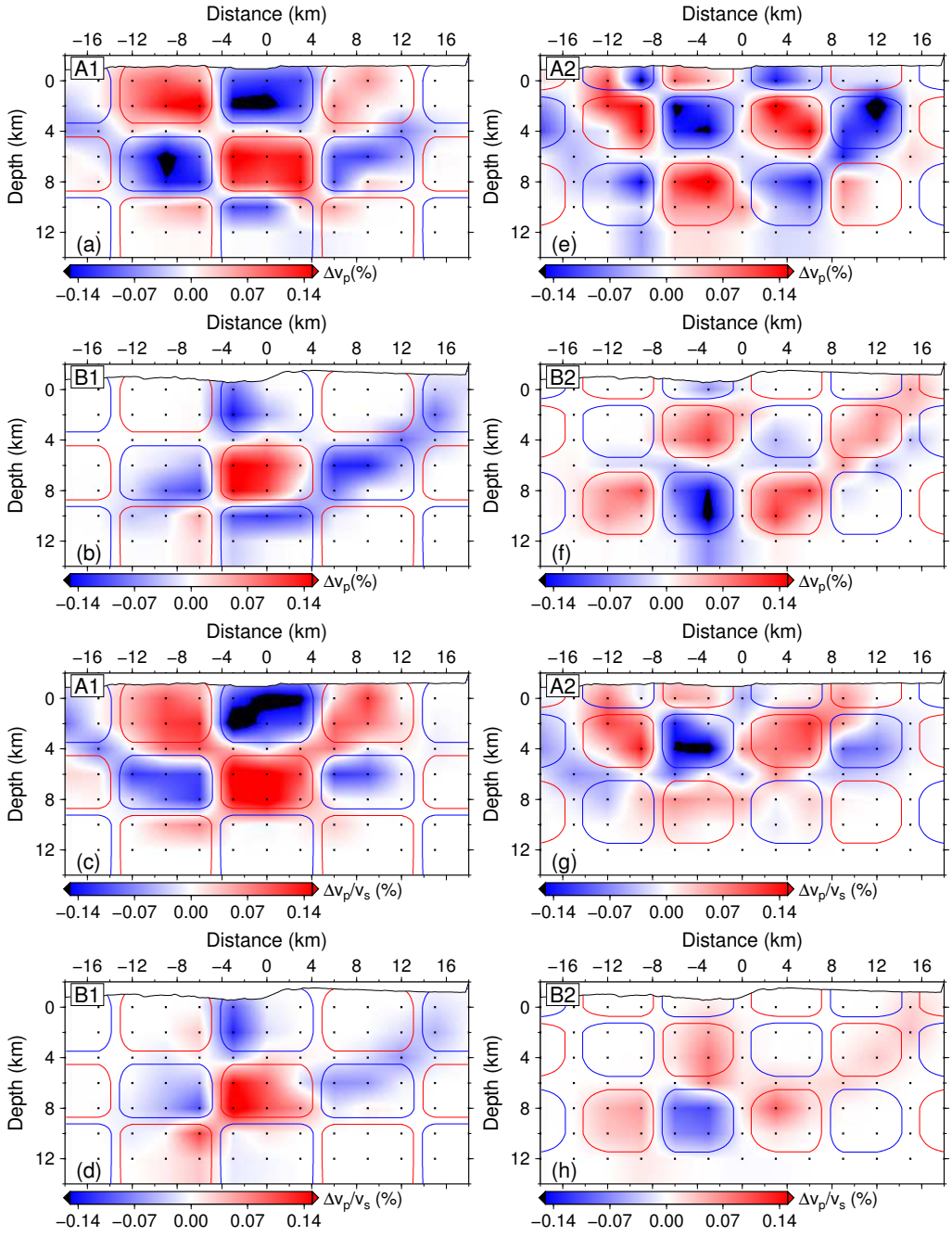

Figure 4.11: Cross-sections of recovered checkerboard models using different pattern size. Model with 12 nodes per anomaly recovered along transect A1 (Fig. a, c) , and along transect B1 (Fig. b, d) . Model with 8 nodes per anomaly recovered along transect A2 (Fig. e, g), and along transect B2 (Fig. f, h) . The cross-sections are taken perpendicular to the Sumatran fault as shown in Fig. 4.10. The red and blue contour lines represent the high and low velocity anomalies.

The checkerboard is also well reproduced in the vertical direction for both the Vp and Vp/Vs models as shown in Fig. 4.11. For the larger checker blocks, the vertical structure along the cross-sections A1 and B1 for Vp models are shown in Fig. 4.11a-b and for Vp/Vs models are shown in Fig. 4.11c-d. The vertical recovery of the checkerboard for smaller size of anomalies are shown in Fig. 4.11e-f for Vp, and in Fig. 4.11g-h for Vp/Vs. The vertical structure of the Vp model is reproduced slightly better than the Vp/Vs as the spread values of Vp is smaller than those of Vp/Vs. The anomalies for both the Vp and Vp/Vs model are resolved at depths above 10 km. In Tarutung, along the cross-section A1 and A2 (Fig. 4.11a, c, e, g) the checkerboards are reproduced well for both the Vp and Vp/Vs for the larger and smaller blocks due to the concentration of the rays within the area.

Along the cross-sections A1 and A2 (Fig. 4.11a, c, e, g), the shallow part of the checkerboard is resolved around 10 km to the left and to the right of the fault line which is consistent with the spread values. In the Sarulla region, the checkerboard above 4 km depth is recovered along the Sumatran fault as represented by the structure along the cross-section B1 and B2 (Fig. 4.11b, d, f, and h).

The Vp checkerboard anomalies along the fault in Tarutung along the cross-sections A1 and A2 (Fig. 4.11a and e) at depth between 2 - 8 km could be recovered with errors of ±5%. Recovery errors at shallower depth are within the range of ±15 %. At greater distances from the fault, recovery errors are in the range of ±7 % for Vp. The Vp/Vs checkerboard anomalies could be recovered with errors of up to ±10%.

We also designed a synthetic model abstracted from the results of the real data inversion as shown in Fig. 4.12 (lateral structure) and Fig. 4.13 (vertical structure). Anomalies of ±15% against the background Vp and Vp/Vs model were incorporated similar in shape to the real data inversion results. We assumed a low Vp structure along the Sumatran fault (Fig. 4.12a-c) associated with the graben and basins filled by unconsolidated material. We also included an anomaly with reduced velocities in the northeast of Tarutung along the cross-section A and in the southwest of Tarutung along the cross-section B (Fig. 4.12a-c). Positive anomalies in Vp/Vs values were assumed in the northeast of Tarutung and along the Sarulla basin (Fig. 4.12d-f) based on the real data inversion results.

The inversion of the abstracted model was carried out identical to the checkerboard test and the real data. In general, all anomalies are reproduced well both in horizontal and vertical directions. The anomalies are recovered by the average of 96% in the Tarutung area and 93% in the Sarulla area.

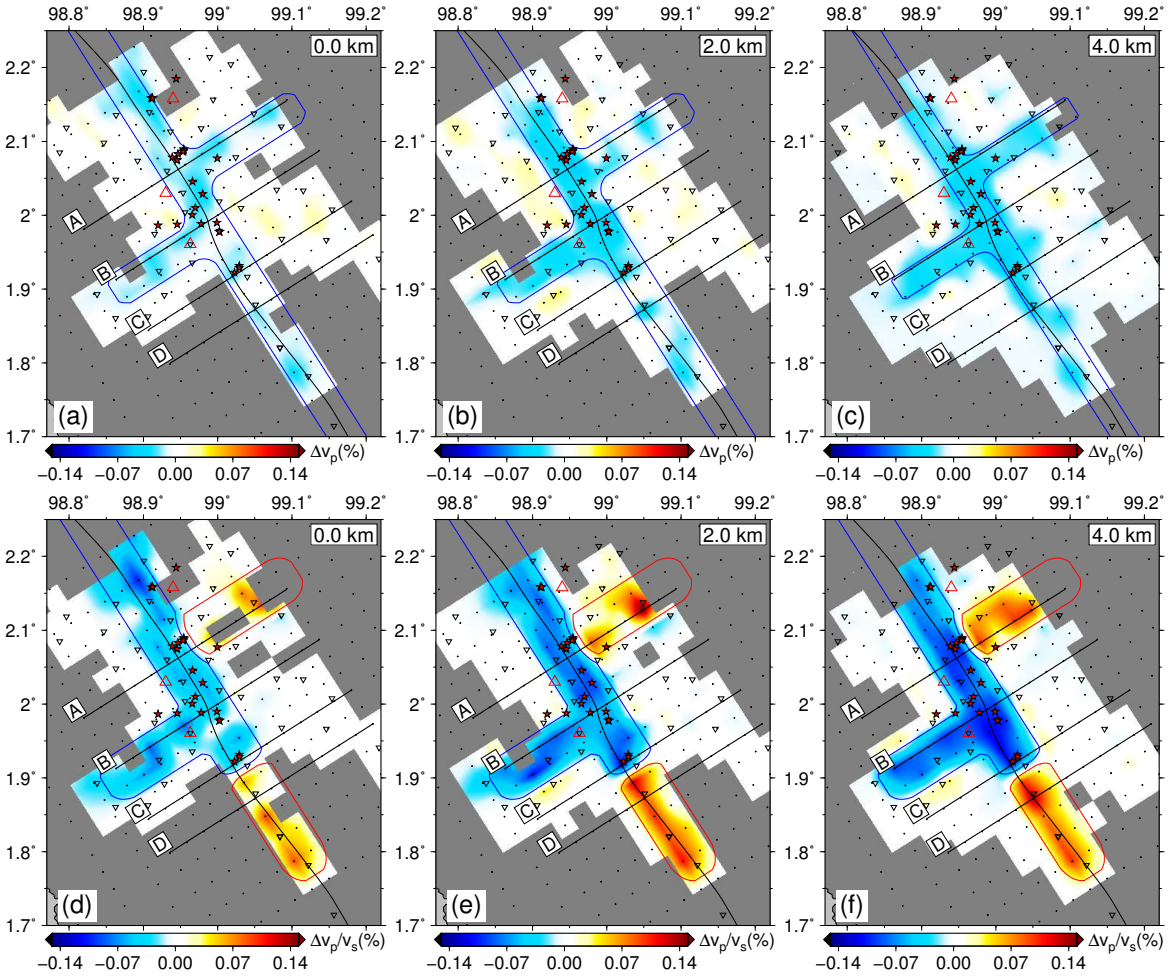

Figure 4.12: Horizontal slices of the recovered synthetic models at 0, 2, and 6 km depth for Vp in (a), (b), and (c), and for Vp/Vs in (d), (e), and (f). The cross-sections A – D are related to the vertical model described in Fig. 4.13. The red and blue contour lines represent the high and low velocity anomalies of the studied synthetic model.

The low Vp structure along the fault (Fig. 4.12a-c) is recovered within the network region which means the low Vp structure might be longer further northwest and southeast but could not be imaged due to the lack of the ray-paths. The shallow part of the northeastern structure along the cross-section A appears patchy both in Vp and Vp/Vs because of the moderate spread values near 99.20 E, 2.10 N. The high Vp/Vs anomaly in the northeast of Tarutung is resolved with moderate smearing. The high Vp/Vs anomaly in the Sarulla region is well resolved, with some degradation in recovery quality at shallow depth.

Comparison of the regions of good recovery of the synthetic structures and the distribution of the spread value suggests that nodes with spread values larger than 2 can

be considered as well resolved, and spread values between 2.0 and 3.0 are considered to be resolved but with moderate smearing.

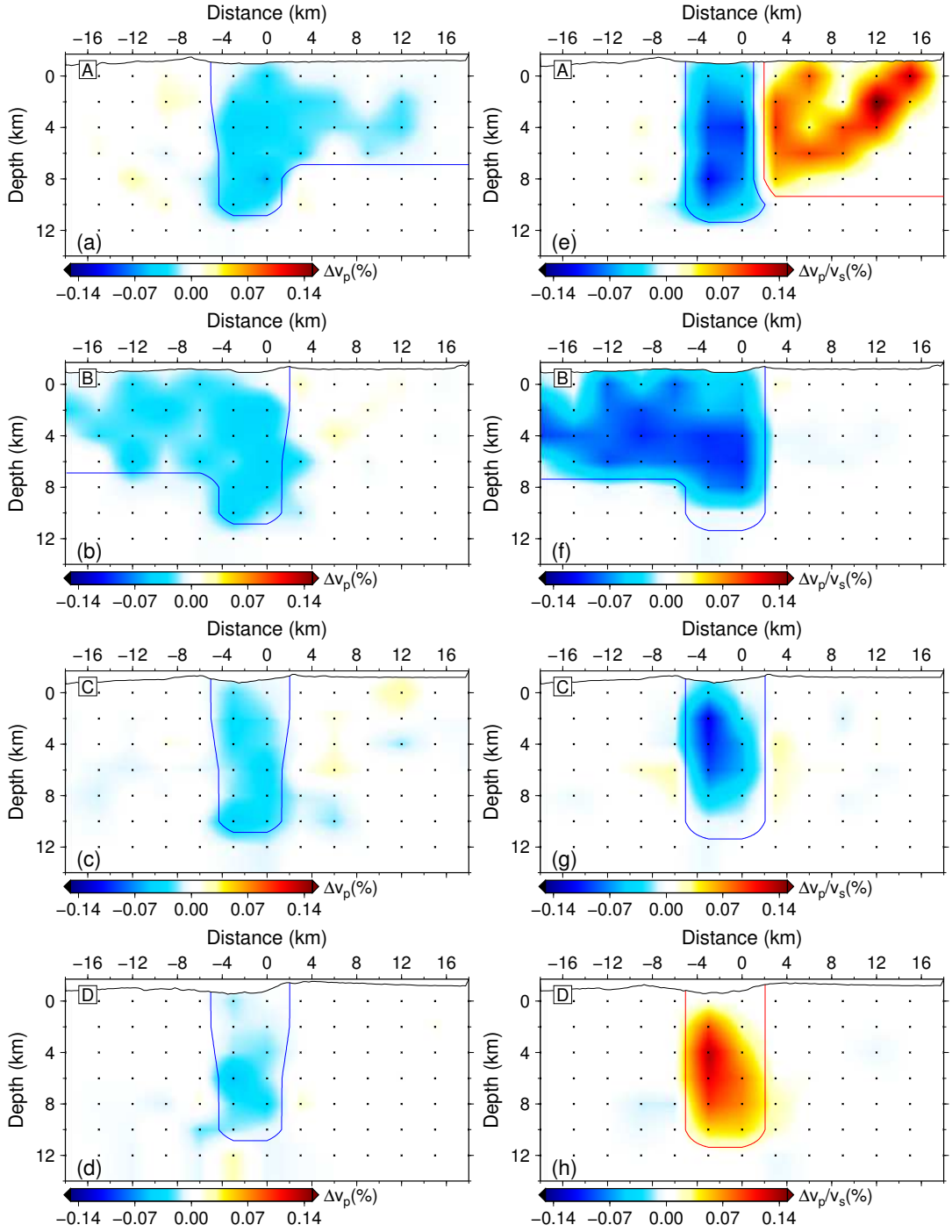

Figure 4.13: The vertical resolved synthetic model of the Vp along the cross-sections A – D in (a) – (d) and of the Vp/Vs along the cross-sections A – D in (e) – (h). The cross-sections are taken perpendicular to the Sumatran fault shown in Fig. 4.12. The red and blue contour lines represent the high and low velocity anomalies.

Well resolved regions include: (1) In Tarutung from cross-sections A to C around 10 km to the left and to the right of the Sumatran fault. However, moderate smearing is present at shallow depth (0 km), (2) Along the Sarulla basin at depth from 2 km. In our anomalies presentation, we only show the well resolved regions with spread values below 3 areas while the areas with less resolution are excluded (clipped). Regions with larger spread values are clipped. In conclusion, we think that in the well resolved regions (as defined above) the uncertainty of the absolute velocities is in the order of ±7% for Vp and better than ±10% for Vp/Vs.

4.6 Results and discussion

The resulting Vp and Vp/Vs models together with the distribution of local earthquakes provide detailed insights into the structure of the Sumatran fault system, the geometry of the sedimentary basins evolving in the study area along the fault, and the interplay between the geological structure and the geothermal system to be explored. We discuss the results from the perspective of each parameter (seismicity, Vp and Vp/Vs), followed by an integration of the different results summarized in a conceptual model for the study area.

4.6.1 Seismicity distribution

The distribution of the local earthquakes is in accordance with the geometry of the Sumatran fault as shown in Fig. 4.6 and is concentrated in the range between 2 km and 11 km depth. The broader distribution of earthquakes around Tarutung indicates the complexity of the fault system within the Tarutung pull-apart basin (see also Fig. 4.15a). To the south, the seismicity is strongly focused on the resembling shape of the Sumatran fault. Along the Sarulla region (the southernmost region), the earthquake distribution is an indication for a narrow and very steep fault (almost vertical, Fig. 4.15d and h) suggesting that there is no vertical segmentation of the fault in this region. Similar results with a narrow steep fault around Sarulla were obtained by Weller et al. (2012). A recent large earthquake occurred within this fault segment. Noteworthy we excluded a large number of events in the Sarulla region because of a gap angle larger than 180 degrees in order to keep the high accuracy of the hypocenters.

4.6.2 Vp structure

The new results are in agreement with previous tomographic investigations (Koulakov

et al., 2009) but provide more detailed insights into the local Vp structure based on the denser network used in our recent study. Comparing the larger scale features of our study with the Vp images of Koulakov et al. (2009), both investigations reveal low velocity regions at shallow depth along the Sumatran fault.

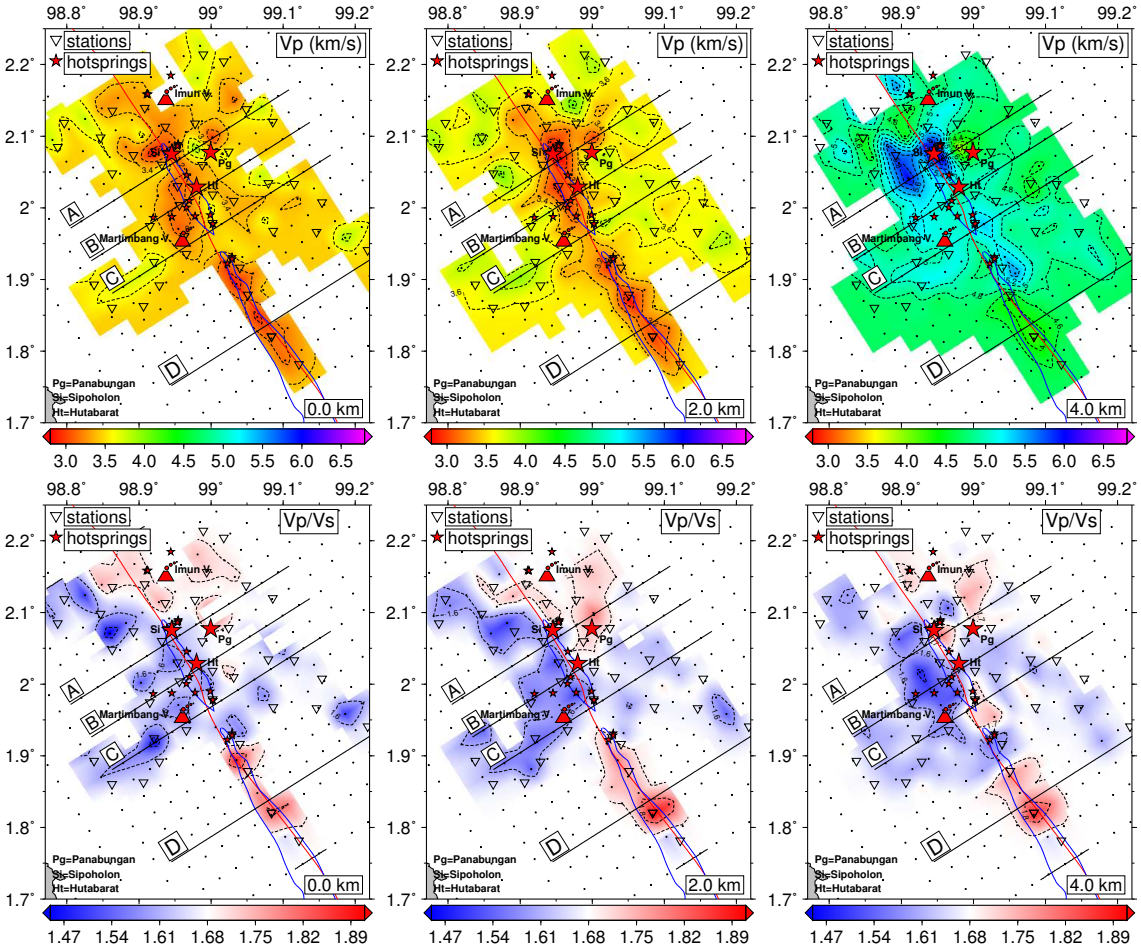

Figure 4.14: Horizontal slices of the models at depth of 0, 2, and 6 km for Vp in (a), (b), and (c), and for Vp/Vs in (d), (e), and (f). The cross-sections A – D are related to the vertical model described in Fig. 4.15.

In more detail, we found relatively low Vp values (around 3 km/s) at shallow regions above 2 km depth (Fig. 4.14 and 4.15). This low Vp at shallow depth reflects the presence of quaternary and Holocene sediments covering the Tarutung and the Sarulla region as also found in other regions along the Sumatran fault (McCarthy and Elders, 1997). More prominent low Vp zones are found along the Sumatran fault associated with the least consolidated sediment fillings within the Tarutung and the Sarulla basins. At depth of 2 km, the pattern of the low velocity zone (Fig. 4.14a) coincides

with the shape of the Tarutung and the Sarulla basins. The synthetic tests have shown that the given low Vp zone along the fault in the area between the cross-sections B and C is well resolved (Fig. 4.12b).

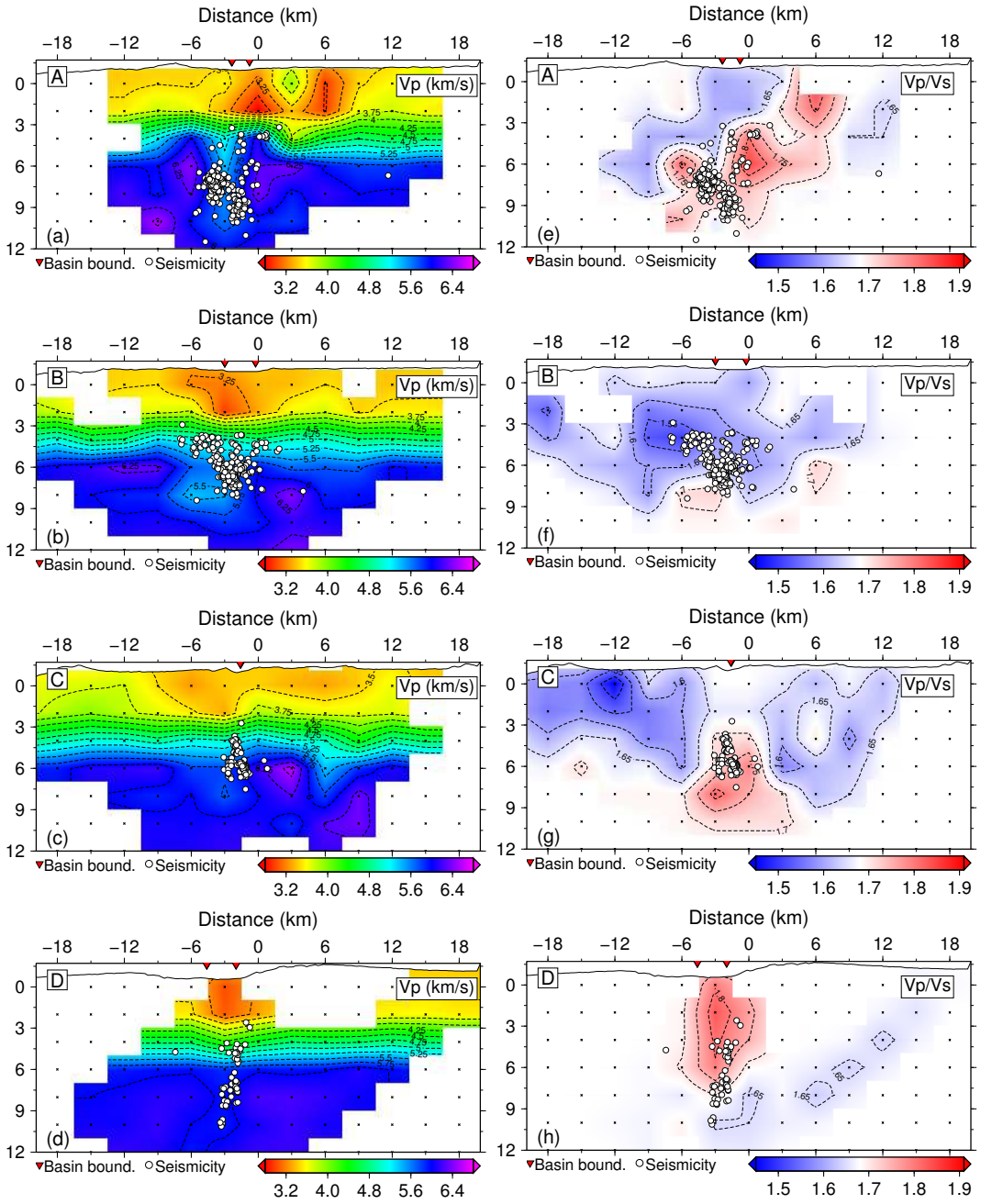

Figure 4.15: The vertical seismic structure for Vp along the cross-sections A – D in (a) – (d) and of for Vp/Vs along the cross-sections A – D in (e) – (h). The cross-sections are taken perpendicular to the Sumatran fault shown in Fig. 4.14.

Therefore, we conclude that the basin along the fault narrows or even vanishes in the area between 1.93^0 N, 99.1^0 E to 1.98^0 N, 98.99^0 E (Fig. 4.14b) indicating that the Tarutung and the Sarulla basins are not connected and have different settings.

The depth of both, the Tarutung and the Sarulla basins is expected at around 2 km as shown by the contour lines of the low Vp of the vertical structure below the fault line along the cross-sections A – D in Fig. 4.15a-d. An abrupt change in the Vp structure (~4 km/s) at around 4 km depth (Fig. 4.14c) represents the discontinuity of the uppermost layer of the structure as also indicated by the images of the vertical structure in Fig. 4.15.

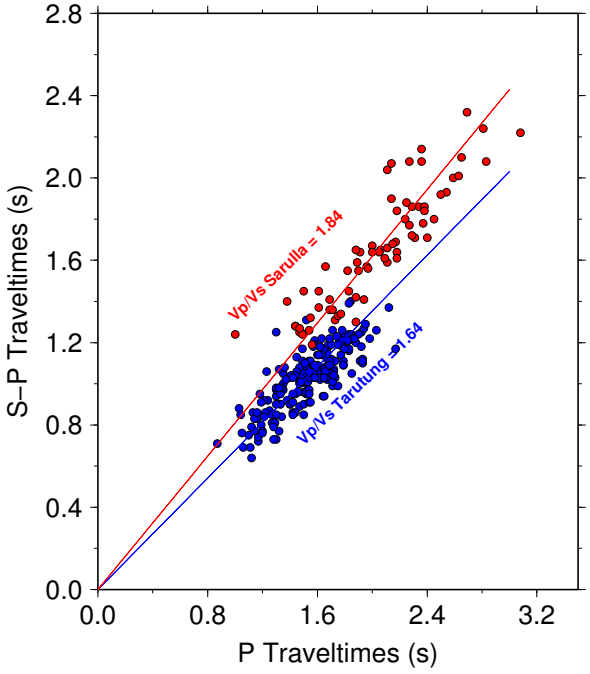

Figure 4.16: The wadati diagrams derived from data recorded by the stations along the Sarulla basin (Vp/Vs=1.84, red line and dots) and by the stations along the Tarutung basin (Vp/Vs=1.64, blue line and dots).

4.6.3 Vp/Vs structure

The basins imaged by low Vp values (around 2 km/s) show distinct characteristics in the Vp/Vs model. While the northern part of the Sarulla graben exhibits high Vp/Vs values (~1.8), the Tarutung basin is characterized by relatively lower Vp/Vs values (1.6). This kind of distinguishing is not only seen in the tomographic inversion results but also in the input traveltime data. In order to test the robustness of this feature,

we analyzed P and S-P traveltimes of stations and local events selected separately from the Tarutung and Sarulla basins which confirmed the difference of both basins as shown by the Vp/Vs average values in the Wadati diagram in Fig. 4.16. Typically, porous sedimentary rocks are characterized by higher Vp/Vs values. The increase of Vp/Vs with increasing fluid content is in agreement with the Gassmann theory developed for porous media (Gassmann, 1951). If such behavior can be taken as a general rule for sediments, we have to assume special geological conditions within the Tarutung basin which are responsible for the lower Vp/Vs values in this region.

Apart from the Tarutung basin and the Sarulla graben, we observe dominantly low Vp/Vs values (~1.6) west and both high and low Vp/Vs values east of the Sumatran fault. The lower Vp/Vs values (~1.6) in the western region could be associated with higher contents of quartz in granitic or andesitic rocks, because quartz is characterized by very low Vp/Vs values (Christensen, 1996). Indeed geological maps indicate the occurrence of granitic rocks in this area (Nukman and Moeck, 2013). On the eastern side of the main fault the Vp/Vs distribution appears more complex. As a first order feature, however, higher Vp/Vs values (1.75-1.8) are found in the northwestern region close to the Tarutung basin where also lower Vp values (3 km/s) were imaged. This could be an indication for sedimentary rocks influenced by the presence of fluids. Our results are in agreement with Koulakov et al. (2009) who imaged within their coarser tomographic grid a similar high Vp/Vs anomaly at shallow depth east of the Sumatran fault within the Tarutung region.

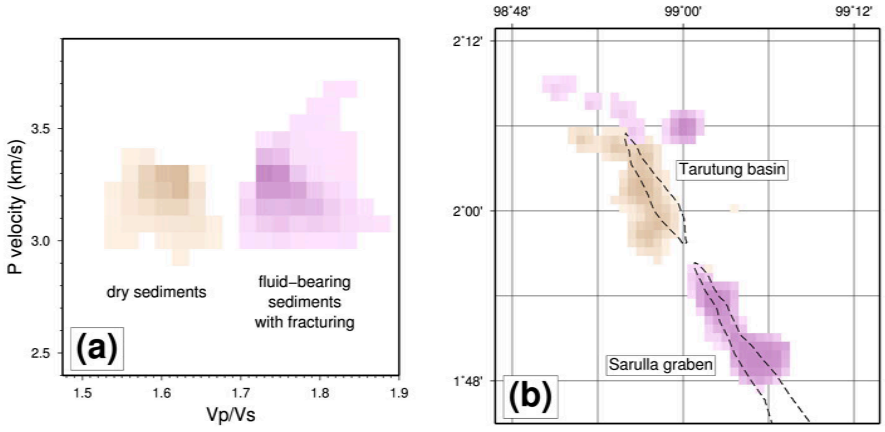

Figure 4.17: Results of a cluster analysis of Vp and Vp/Vs values derived for the sedimentary parts (low Vp regions) of the tomographic model. (a) Two clusters (brown and pink colors) with characteristic Vp and Vp/Vs were identified. (b) Geographic distribution of the cluster members in relation with the Tarutung basin and Sarulla graben.

4.6.4 Joint interpretation of Vp and Vp/Vs

Motivated by the previously mentioned arguments rising from the joint consideration of Vp and Vp/Vs we applied quantitative joint interpretation techniques to study the Vp and Vp/Vs signatures of the Tarutung and the Sarulla basins. The combined consideration of Vp and Vp/Vs in corresponding cross-plots is a well-established approach for the lithological interpretation of seismic velocity models (e.g. Holbrook et al., 1992). Distinct rock types can be identified in such cross-plots by application of statistical cluster analysis techniques (e.g. Bauer et al., 2003; Ryberg et al., 2012; Stankiewicz et al., 2010a). Here we make use of alternative clustering techniques which belong to the neural network pattern recognition and classification methods, called self-organizing maps (Kohonen, 2001).

We applied a self-organizing map work flow developed by Bauer et al. (2008) which includes preparation and normalization of data vectors, unsupervised learning, identification of clusters by usage of image processing techniques, and application of the learned knowledge to classify rock types. More details of this method can be found in Bauer et al. (2012). We applied the neural network clustering to the tomographic Vp and Vp/Vs images with particular focus on the regions with relatively low P velocities in order to highlight the characteristics of the Tarutung and Sarulla basins (Fig. 4.17). Two clusters were found which show a similar Vp range but differences in Vp/Vs (Fig. 4.17a). Plotting the members of each cluster with regard to the geographic coordinates reveals that the cluster with lower Vp/Vs (brown colors in Fig. 4.17) corresponds to the Tarutung basin, and the cluster with higher Vp/Vs (pink colors in Fig. 4.17) is imaged within the Sarulla graben and northeast of the Tarutung basin. In our interpretation we assume that dry sediments within the Tarutung basin are responsible for the lower Vp/Vs cluster while the higher Vp/Vs cluster is associated with the presence of fluids and fracturing both reducing Vs stronger than Vp and, hence, increasing Vp/Vs. In order to explain theses systematic differences we suggest conceptual models for Tarutung and Sarulla as described in the following.

4.6.5 Conceptual models for Tarutung and Sarulla

Based on differences in the seismicity distribution, the Vp and Vp/Vs structure, and geological and tectonic information known from Tarutung and Sarulla, we developed conceptual models for both regions with geothermal potential as shown in Fig. 4.18 and 4.19, respectively. The model for Tarutung covers the upper 12 km and consists of three layers interrupted by the Tarutung basin in the center of the model (Fig. 4.18). The subdivision into three layers is mainly based on the Vp structure (Fig. 4.15a-d),

with P velocities of 3-4 km/s in the upper layer, 4-5 km/s in the middle layer, and 5-6 km/s in the lower layer. We assume that this increase of P velocity with increasing depth is related to the reduction of porosity and also with petrologic differentiation of mainly volcanic rocks. The Tarutung basin in the central part of the model is characterized by the lowest P velocities indicating unconsolidated sedimentary rocks and young Toba tuff (Hickman et al., 2004) deposited within the pull-apart basin. To explain the low Vp/Vs values within the basin we suggest that these sediments are lacking significant amounts of fluids within the pore space. Such an interpretation is also supported by the modeling of low Vp and low Vp/Vs anomalies in porous volcanic rocks described by Husen et al. (2004). Instead, we assume that hot fluids are transported from greater depth along the deeper Sumatran fault zone into the shallow regions just northeast of the Tarutung basin using more permeable fluid pathways, also in agreement with the higher Vp/Vs values imaged within this part of the model.

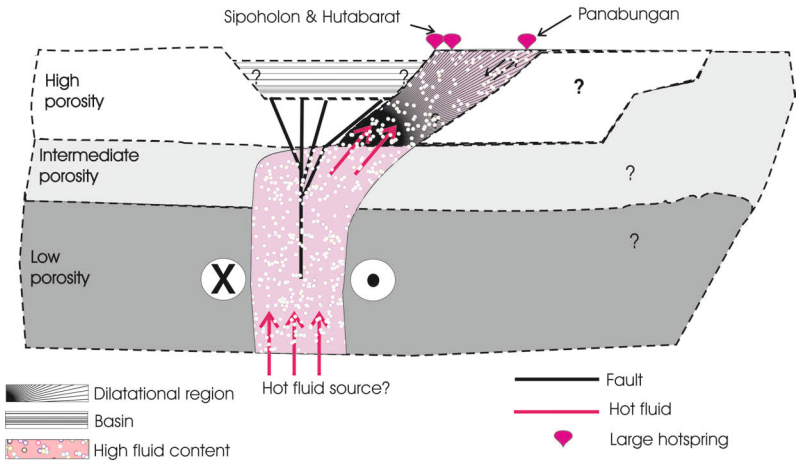

Figure 4.18: Conceptual model for the Tarutung basin based on the seismicity distribution, Vp and Vp/Vs structure derived by the tomography analysis containing three main layers. The hot fluid originated from below the fault and transported to the northeast around the three big hotsprings.

A possible tectonic explanation for such a fluid flow model could be that releasing right step-overs along right-lateral fault systems, as the Tarutung pull-apart basin, are related to extensional quadrants (Bellier and Sébrier, 1994), in our case northeast of the Tarutung basin. This is exactly the region where we observe the cluster of high Vp/Vs (pink colors in Fig. 4.17b), which we interpret as fluid bearing sediments with fracturing. Dilatational elements were also found by the structural geology investigations of Nukman and Moeck (2013) in this region. This interpretation is also

supported by the occurrence of the big hot springs of Panabungan, Hutabarat, and Sipoholon located northeast of the Tarutung basin.

The model along the Sarulla basin also consists of three main layers forming the background structure for the shallow graben located in the center (Fig. 4.19). Again we assume porosity changes and petrologic differentiation of mainly abundant volcanic rocks responsible for the vertical structuring of the background model. The Sarulla graben appears to reflect a simpler fault structure compared to the more complex Tarutung pull-apart basin. The Sarulla graben has been formed by the extension nearly perpendicular to the strike of the weak wrench fault (Hickman et al., 2004). A shallow zone of low Vp is directly linked with the rather narrow, vertically oriented distribution of earthquakes at greater depth, also in agreement with seismicity investigations of Weller et al. (2012). High Vp/Vs values are imaged both at the shallow parts of the graben and at greater seismogenic depths. We conclude that fluid flow occurs along the entire fault system transporting heat from greater depth to the surface. This interpretation is also expressed in the description of the pink colored cluster in Fig. 4.17a as fluid bearing sediments with fracturing imaged along the Sarulla graben in Fig. 4.17b.

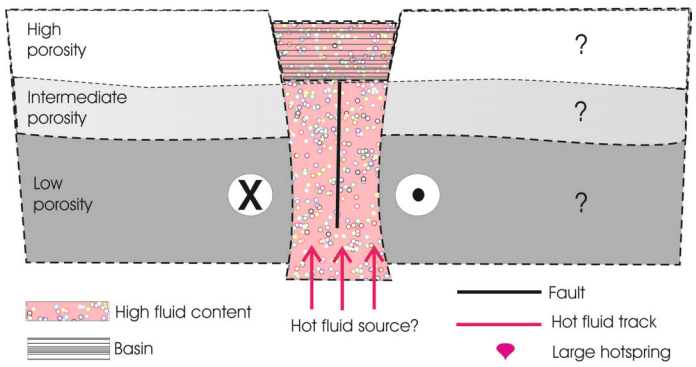

Figure 4.19: Conceptual model for the Sarulla graben based on the seismicity distribution, Vp and Vp/Vs structure derived by the tomography analysis. The hot fluid from below the fault is transported directly to the surface along the weak fault.

For both models (Fig. 4.18 and 4.19) the heat source is assumed to be located at much greater depth related to magmatic activities triggered by the subduction process, and the heat is transported along the permeable Sumatran fault to the shallow regions of the Tarutung and the Sarulla basins. We assume that the high permeability is related to a wider damage zone and fractured regions developing during strike-slip tectonics around a temporary impermeable gauge zone.

4.7 Conclusion

Seismological measurements for tomographic investigations using a dense network were conducted for geothermal exploration at a scale between micro and local seismicity which is new for Indonesia to our knowledge. High quality data could be collected and allowed us to resolve detailed features of Vp and Vp/Vs around the Tarutung basin and the Sarulla graben. We found systematic differences between both basins evolving along the Sumatran fault. Tarutung is a pull-apart basin formed by a releasing step-over (Bellier and Sébrier, 1994). As a consequence, the region northeast of Tarutung is influenced by a dominantly dilatational stress regime (Nukman and Moeck, 2013) which in our interpretation supports focussing of fluid transport from greater depth into this area. High fluid content and fracturing in this part of the Tarutung region is reflected by high Vp/Vs values in the tomography model. Along the Sarulla graben we imaged a less complex fault structure which shows high Vp/Vs values within a narrow fault zone both at greater depth and also in the shallow part above the near-vertical seismogenic region. We infer that fluids and heat are transported along the permeable Sumatran fault within this narrow structure directly to the surface. Similar observations of localized high Vp/Vs anomalies and their interpretation as fluid-rich regions were also reported from the San Andreas fault system (e.g. Thurber et al., 1997). As a main result of our study we conclude that high Vp/Vs regions can be imaged at high resolution and that they potentially indicate regions of high fluid content and fracturing as one possible explanation. In combination with other methods, such as magnetotellurics and structural geology, this can be used to constrain potential areas for geothermal exploitation.

Future steps to be applied to our high quality data set will included high resolution studies of seismicity including fault-plane solution, attenuation tomography, and ambient noise analysis. The results will then allow us to further constrain the conceptual models developed in this paper.

Acknowledgements

First of all we wish to thank all participants of the seismological field experiment who helped during deployment, service trips, and re-collection of instruments. The equipment and related software was provided by the Geophysical Instrument Pool Potsdam (GIPP). This work was carried out under the umbrella of the project “Sustainability concepts for exploitation of geothermal reservoirs in Indonesia” funded by the Federal Ministry of Education and Research (BMBF) in Germany. We are thank-

ful to the Ministry of Research and Technology, the Center for Geothermal Resources of Indonesia, and the Tarutung local government for the collaboration and helpful support during the field experiment. The authors wish to thank Dr. Inga Moeck and Muhammad Nukman for fruitful discussions on the geological setting of the study area based on their field observations. We wish to thank the reviewers for suggestions and helpful comments on the manuscript.

Chapter 5

3-D upper crustal structure of the geothermal system in Tarutung (North Sumatra, Indonesia) revealed by seismic attenuation tomography

U. Muksin[1,2], Christian Haberland[1], Klaus Bauer[1], M. Weber[3]

[1]German Research Centre for Geosciences GFZ, Potsdam, Germany
[2]Department of Physics, Syiah Kuala University, Banda Aceh, Indonesia
[3]Institute of Earth and Envinronmental Science, the University of Potsdam
Contact: muksin@gfz-potsdam.de

Published 2014 in Geophysical Journal International, 195(3), pp. 2037-2049

Summary

The geothermal potential in Tarutung is controlled by both the Sumatran fault system and young arc volcanism. In this study we use the spatial distribution of seismic attenuation, calculated from local earthquake recordings, to image the 3D seismic attenuation of the area and relate it with the temperature anomalies and the fluid distribution of the subsurface. A temporary seismic network of 42 stations was deployed around Tarutung and Sarulla (south of Tarutung) for a period of 10 month starting in May 2011. Within this period, the network recorded 2,586 local events. A high-quality subset of 229 events recorded by at least 10 stations was used for the attenuation inversion (tomography). Path-average attenuation (t^*_{p}) was calculated by using a spectral inversion method. The spread function, the contour lines of the model resolution matrix, and the recovery test results show that our 3-D attenuation model (Q_{p}) has good resolution around the Tarutung basin and along the Sarulla graben. High attenuation (low Q_{p}) related to the geothermal system is found in the northeast of the Tarutung basin suggesting fluid-pathways from below the Sumatran fault. The upper part of the studied geothermal system in the Tarutung district seems to be mainly controlled by the fault structure rather than by magmatic activities. In the southwest of the Tarutung basin, the high attenuation zone is associated with

the Martimbang volcano. In the Sarulla region, a low Q_p anomaly is found along the graben within the vicinity of the Hopong caldera.

Keywords: Seismicity and tectonics; Body waves; Seismic attenuation; Seismic tomography.

5.1 Introduction

The Tarutung region is one of the geothermal areas in Sumatra that the Indonesian government (the Center for Geological Resources) is planning to exploit. The geothermal potential in the region is manifested by several hot springs (represented by red stars in 5.1) along the Tarutung basin. The most prominent geothermal manifestations are Sipoholon, Panabungan, and Hutabarat (see large red stars in Fig. 5.1). As Tarutung is located on the Tarutung basin along the Sumatran fault and surrounded by young volcanoes and calderas, the whole tectonic system of the area is considered to play a significant role for the geothermal system (Muksin et al., 2013a).

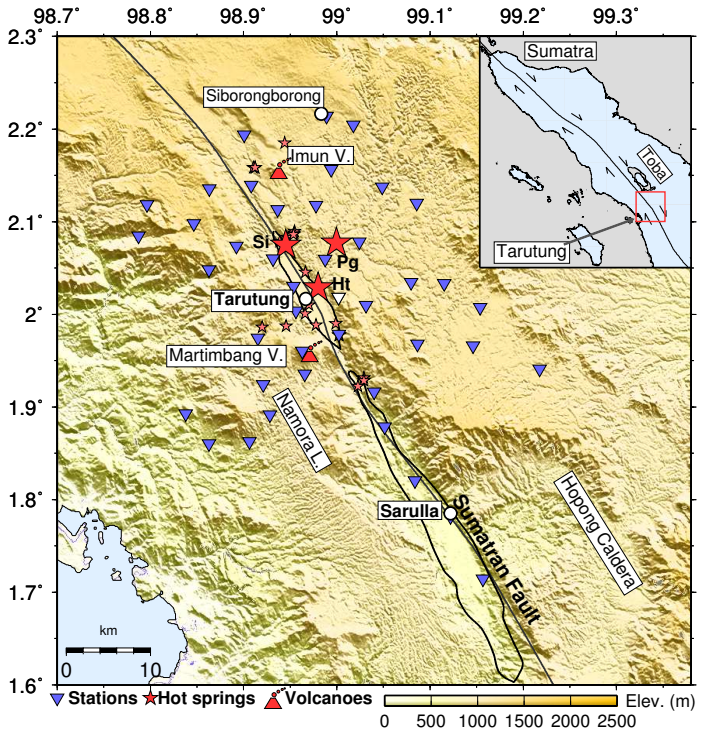

Figure 5.1: The seismic network deployed in Tarutung for 10 months. The Tarutung region is located just south of Lake Toba (inset map). Three main hot springs, represented by the large red stars, are located in Sipoholon (Si), Hutabarat (Ht), and Panabungan (Pg).

Geophysical methods were applied for a first evaluation of the geothermal potential around Tarutung including shallow seismics, geoelectrics, and magnetotellurics (Niasari et al., 2012). Since Tarutung is located in a seismically active region along the Sumatran fault, passive seismic methods can be also utilized. Previous seismological studies at a larger scale including the Tarutung area were conducted at the near Toba caldera by using Vp and Vp/Vs tomography (Koulakov et al., 2009) and ambient noise tomography (Stankiewicz et al., 2010b). However, these two studies were not resolving details of the Tarutung geothermal area. Therefore, a dense new passive seismological experiment was conducted in 2011 to achieve the resolution required for geothermal exploration around Tarutung (Muksin et al., 2013a). The resulting Vp and Vp/Vs tomographic images revealed the geometry of the Tarutung and Sarulla basins as well as potential fluid path ways indicated by high Vp/Vs anomalies (Muksin et al., 2013a).

In Tarutung the existing Vp and Vp/Vs models (Muksin et al., 2013a) can be complemented by studying seismic attenuation (Q^{-1}). In attenuation tomography, authors generally associate high intrinsic attenuation anomalies with high fluid flow, saturated rocks or cracks, and/or high temperature or pressure zone (Evans and Zucca, 1988; Haberland and Rietbrock, 2001; De Lorenzo et al., 2001; Zucca and Evans, 1992; Zucca et al., 1994). On the opposite, low to moderate attenuation is usually associated with dry and compact rocks. It has been proposed that attenuation is related to a variety of physical mechanisms rather than to chemical composition (e.g. Sato et al., 1989). Laboratory experiments have shown that seismic energy is dissipated through grain boundary interaction or intra-granular relaxation (Sato et al., 1989). The dissipation is different from one to another composition related to internal mechanisms. The presence of some amount of water in cracks or pores may attenuate seismic energy which lowers Q (Karato, 2003). This mechanism is called viscous dissipation which includes shear relaxation and pressure change within cracks or pores (Mavko et al., 1979; Walsh, 1995). Another attenuation is caused by thermally activated mechanisms which includes grain boundary relaxation and sliding (Sato et al., 1989). Melting or partial melting will dissipate seismic energy because of the pressure gradient within rocks and also lattices or atoms within materials are more mobile therefore seismic energy is easier to be absorbed. The sensitivity of intrinsic attenuation on temperature and fluid saturation (e.g. De Siena et al., 2010; Haberland and Rietbrock, 2001; Martínez-Arévalo et al., 2005; Zucca et al., 1994) makes it an ideal parameter to study geothermal prospects. In addition, other processes such as geometrical spreading, multipathing and focusing/defocusing due to structural heterogeneities, reflection and transmission at structural boundaries, as well as scattering

can cause redistribution of seismic energy thus potentially contributing to the total or apparent attenuation (Q_t^{-1}).

In the Geysers geothermal field (USA), increased attenuation was found within the reservoir and the attenuation was higher at greater depth interpreted as fluid-saturated rocks (Zucca et al., 1994). High attenuation in the western central Andes correlates with the location of the magmatic arc and was associated with thermally weakened crust and partial melting (Haberland and Rietbrock, 2001). Supported by the Vp and Vp/Vs tomography results and other geophysical data, attenuation tomography was able to distinguish gas and fluid reservoirs as well as hydrothermal basins in Campi Flegrei (De Siena et al., 2010). Priyono et al. (2011) revealed high P and S wave attenuation anomalies beneath the Mt. Guntur complex, West Java Indonesia, consistent with low P and S velocity. High attenuation was also found in a sediment basin and beneath the magmatic arc in central and east Java (Bohm et al., 2013).

The main aim of the study is to further constrain the nature of the geothermal system. The paper describes regional setting and experiment, data analysis and inversion for Q_p, and finally provides an integrated interpretation of Q_p together with the existing Vp and Vp/Vs models to improve the understanding of the geothermal system and its relation to the tectonic setting of the region. Several time-domain and frequency-domain methods have been developed to estimate attenuation of observed seismograms at various scales. The coda-Q (Q_c) estimation regularly used in crustal scale studies (e.g., Chung et al., 2009) utilizes the amplitude decay of the later parts of the seismogram as a function of time (and frequency; Aki and Chouet, 1975). Q_c is often found to be frequency-dependent, and considered to be related to scattering and intrinsic attenuation (e.g., Aki and Chouet, 1975; Frankel and Wennerberg, 1987). Alternatively, the analysis of spectra of certain phases (e.g., P, PP, S, SS; often body waves) is applied to global (e.g. Hwang et al., 2011), regional, and local data. Spectral division is often used to remove some of the factors influencing seismic spectra (e.g. source effects, site effects) without knowing their exact form (e.g. Flanagan and Wiens, 1990; Sanders, 1993). Spectral inversion (including source parameters, site effects, attenuation) was successfully applied to data sets covering a broad range of scales, from the local scale (Boatwright et al., 1991; Rietbrock, 2001; Scherbaum, 1990) to the regional scale (Schurr et al., 2003). Pulse rise time (Gladwin and Stacey, 1974), pulse-widths (Wu and Lees, 1996) and frequency-shift (Quan and Harris, 1997) methods are also utilized in the lab and on a local scale. In this paper we use a spectral inversion method to derive the path-averaged attenuation parameter t^* from body P-waves and invert for the 3-D distribution of the Quality factor Q_p using attenuation

tomography.

5.2 Regional setting

The variation of the geometry and morphology of the subduction zone beneath Indonesia reflects the changes in rate and direction of the Indo-Australian plate motion. In Java, the Indo-Australian plate motion is perpendicular to the trench correlating with the steep subduction zone. In Northern Sumatra, the plate motion becomes more oblique and even almost parallels the trench in Andaman which could be related to the more gradual subduction zone (Pesicek et al., 2010). The oblique convergence between the Indo-Australian and Eurasian plates along Sumatra has produced the lateral-slip Sumatran fault accommodating the trench-parallel component (Bellier and Sébrier, 1994; McCaffrey, 2009; Sieh and Natawidjaja, 2000).

The 1,900 km long Sumatran fault is segmented into 19 sections, locally represented by several pull-apart basins (Sieh and Natawidjaja, 2000). The variation of the Indo-Australia plate motion is also related to the slip rate along the Sumatran fault. Derived from stream offsets observed on SPOT images, the recent slip rate increases from less than 10 mm/yr in the Sunda strait at the southernmost, to ll-19 mm/yr in central Sumatran, and 23 $\pm$ 2 mm/yr around Tarutung and Toba (Bellier and Sébrier, 1995). Along the Sumatran fault, the earthquakes are mostly strike-slip with the maximum magnitude of Ms 7.7 but some normal fault earthquakes occurred within the pull-apart basins (Sieh and Natawidjaja, 2000). This normal faulting indicates simultaneous strike-slip motion and transform-normal extension within a strike-slip fault zone (Bellier and Sébrier, 1994).

The Tarutung district covers the area of 98.70 E to 99.40 E and 1.60 N to 2.30 N centered around the diamond-shaped pull-apart basin with clearly defined borders. The Tarutung basin is located between the two main features of the Sumatran fault, the Toba caldera in the north and the bifurcation in the south. The Tarutung pull-apart basin is characterized by a presently active fault zone produced as a result of a larger step-over of the previous fault system in the Toba area and subsequent formation of the great Toba caldera within this older step-over region (Bellier and Sébrier, 1994). To the south of Tarutung, there is an asymmetrical basin called Sarulla graben characterized by normal faults that parallel the weak major strike-slip fault (Hickman et al., 2004).

The volcanic arc, including the young volcanism along the Sumatran fault, correlates

with the geometry of the fault and the Sunda trench (Sieh and Natawidjaja, 2000). The Tarutung basin is surrounded by the Martimbang, Helatoba (outside of the map), and Imun volcanoes as shown in Fig. 5.1. The yet undated Martimbang volcano is characterized as a young andesite basaltic cone (Hickman et al., 2004), while the Helatoba and Imun might have been created in Pleistocene (Gasparon, 2005). Along the Sarulla graben, the volcanism includes the Hopong caldera, Namora-I-Langit dome field, and Sibual-buali volcano (south of Sarulla) which are related to the weakening of the strike-slip fault. Along the Sumatran fault, around 50% of the geothermal manifestations are associated with pull-apart basins while the other half is related to volcanic activities (Muraoka et al., 2010). In the case of the Tarutung and Sarulla geothermal areas, both, the pull-apart basins and volcanic activities, might contribute to controlling of the geothermal system.

5.3 Experiment and data

Fig. 5.1 shows our temporary network consisting of 42 short period seismic instruments installed in the Tarutung and Sarulla region for 10 months starting May 2011 with an average station spacing of around 5 km. 40 stations were equipped with three component short period (1 Hz) sensors, and digital PR6-24 Earth Data Loggers sampling at 100 sps. Two additional stations were equipped with three component 4.5 Hz geophones and DSS CUBE data logger (Omnirecs) recording data with 100 sps.

An automated picking procedure (Nippress et al., 2010) was used to identify the P and S wave arrivals from local events which we then manually checked and revised. Our catalog includes 2,586 events recorded by at least 8 stations. Waveforms with ambiguous onset were excluded. The HYPO71 routine (Lee and Valdes, 1985) was then applied to determine the initial hypocenters. Eventually, 809 high quality events with gap angles smaller than 180 degrees were relocated by using 1D and 3D inversion for velocity structure and hypocenter relocation. Details of this data analysis as well as the resulting seismicity distributions and Vp and Vp/Vs structure can be found in Muksin et al. (2013a). Among these 809 events, only 229 events with high quality waveforms are used in the seismic attenuation tomography (discussed in the next section).

5.4 Methods

5.4.1 Formulation of seismic attenuation

The amplitude spectrum $A_{\mathrm{ij}}(f)$ of body/P wave of a source j observed at receiver i can be expressed in the following way (Sanders, 1993; Scherbaum, 1990):

$$A_{ij}(f) = S_j(f) \cdot R_i(f) \cdot I_i(f) \cdot B_{ij}(f) \cdot G_{ij} \tag{5.1}$$

where f is frequency, $R_{\mathrm{i}}(f)$ is the receiver site effect, $I_{\mathrm{i}}(f)$ is the instrument response, and G_{ij} is the geometrical spreading which we assume to be frequency-independent. The source spectrum $S_{\mathrm{j}}(f)$ can be described following e.g. Scherbaum (1990) as:

$$S_j(f) = \frac{\Omega_0}{1 + \left(f^{\gamma}/f_{cj}^{\gamma}\right)}, \tag{5.2}$$

where Ω_0 represents the long-period spectral level, γ is the high frequency decay rate, and f_{cj} is the corner frequency. Equation (5.1) is equivalent to a Brune type ω^2 source model (Brune, 1970, 1971; Hanks and Wyss, 1972) when $\gamma = 2$. The attenuation spectrum of seismic P waves is defined as (Sanders, 1993):

$$B_{ij}(f) = \exp\left(-\pi t_{ij}^{*} f\right) \tag{5.3}$$

The path-averaged attenuation t^* is determined from the rock-properties along the ray-path, in particular from the (specific) attenuation $Q_{\mathrm{p}}^{-1}(r)$ and the seismic P-wave velocity $Vp(r)$ (see e.g. Scherbaum, 1990) as:

$$t_{ij}^{*} = \int_{ray} Q_p^{-1}(r) v^{-1}(r) dr + \tau_i^{*} \tag{5.4}$$

The parameter Q_i^{-1} is a constant accounting for the attenuation beneath the station (so-called station correction). Assuming Q_{p} to be frequency independent, the amplitude spectra from the combination of equation (5.1), (5.2), and (5.3) can be expressed by

$$A_{ij}(f) = \frac{\Omega_{0\mathrm{j}}^{'} \exp\left(-\pi t_{ij}^{*} f\right)}{1 + \left(\frac{f^2}{f_{cj}^2}\right)} \tag{5.5}$$

where $\Omega_{0\mathrm{j}}^{'}$ is the signal moment taking up the source moment $\Omega_{0\mathrm{j}}$ and all frequency-

independent factors possibly influencing the spectrum between the source and the receiver (e.g. Haberland and Rietbrock, 2001).

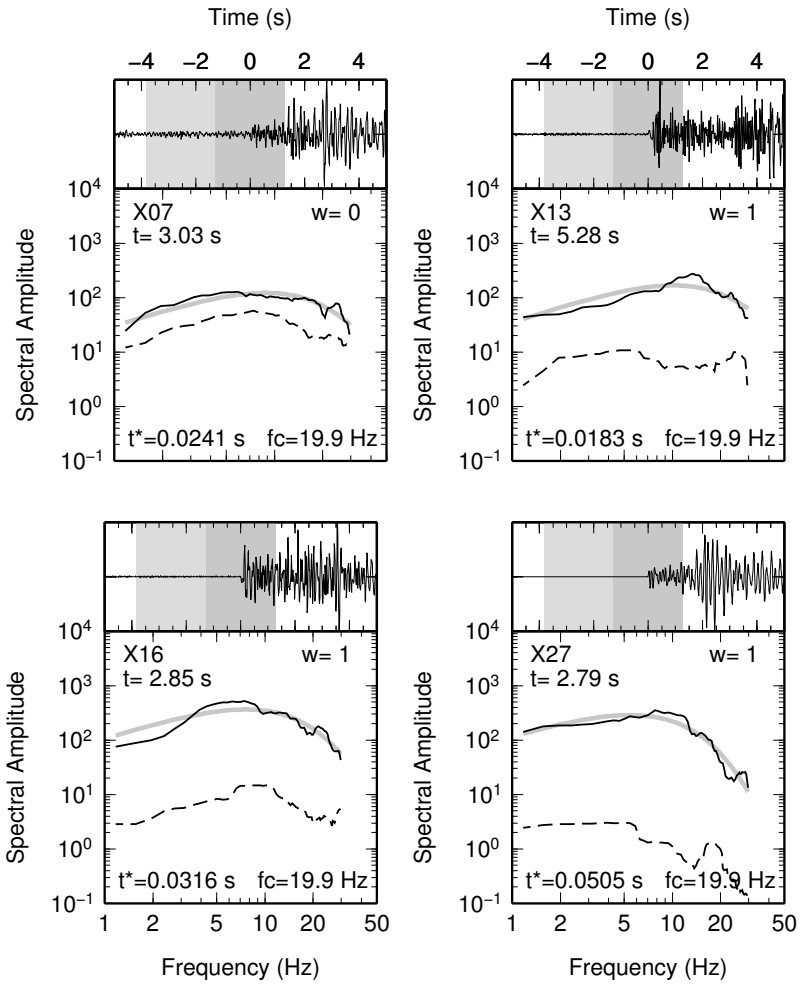

Figure 5.2: The calculation of t^*-values using spectral analysis of four records (stations X07, X13, X16, X27) of an event (the location is shown in Fig. 5.3) occurred on 20th November 2013. t is traveltime, w is the weight representing the quality of the waveforms, and f_c is the source corner frequency. The top panels show the normalized time series. The signal is within the darker shading windows following the noise in the lighter shading windows. The bottom panels show the noise spectrum (dashed lines), signal spectrum (black lines), and estimated spectrum resulting from spectral inversion (light-bold lines).

To estimate the above mentioned attenuation parameters, a 2.56 s time window centered at the P-wave arrivals was analyzed using a multi-taper technique (Park et al., 1987). We also analyzed the time window before the P wave arrival to assess the signal to noise ratio (Fig. 5.2). In the inversion we simultaneously calculate the following free parameters: 1) individual seismic attenuation along the propagation path

t^*_{ij} for each observation of an event, 2) individual signal moment Ω'_{0j}, and 3) a single source corner frequency f_{cj} for all records of an event using a non-linear spectral inversion method (e.g. Rietbrock, 2001; Eberhart-Phillips and Chadwick, 2002). It is well known that the source corner frequency f_c and the t^* values have a quite similar effect on the shape of earthquake spectra yielding ambiguities when inverting single spectra (e.g. Scherbaum, 1990; Boatwright et al., 1991). The approach of inverting for individual seismic attenuation parameters t^*_{ij} and a single source corner frequency f_{cj} common for all observations of an event proved to reliably separate these factors when a sufficiently large number of spectra are used (Rietbrock, 2001; Haberland and Rietbrock, 2001; Eberhart-Phillips and Chadwick, 2002; Bohm et al., 2013).

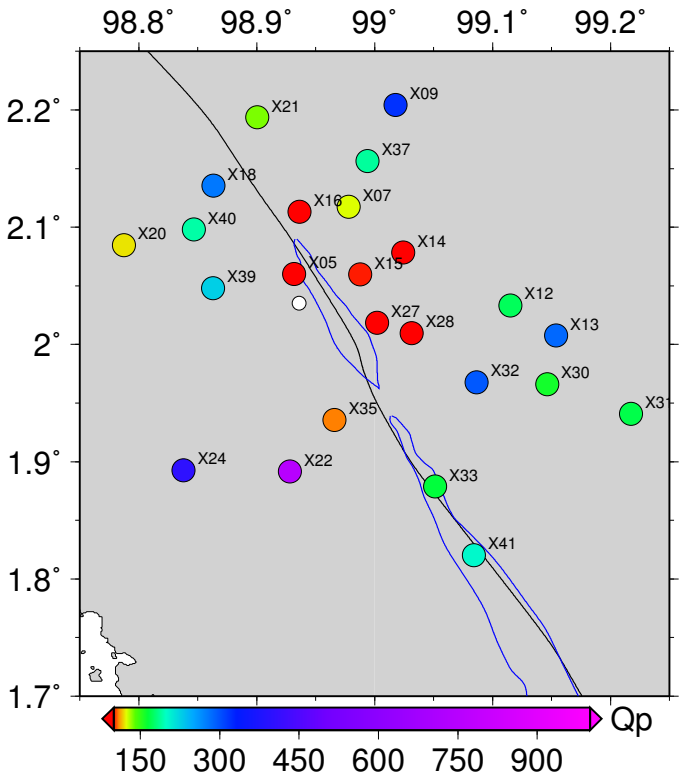

Figure 5.3: Estimated Q_p values of all observing stations of an event marked by the white circle. The corresponding t and t^*-values are shown in Fig. 5.2 for 4 stations showing low Q_p values for station closed to the basin, located in the northeast of Tarutung.

In this inversion a frequency band between 1 (at the lower boundary) and 10 to 30 Hz (at the upper boundary), depending on noise, was analyzed. Only events having at least 10 usable observations were included (i.e. with a signal to noise ratio higher than 1.4) resulting in a final data set of 3968 t^*-values of 229 events which were used in the tomographic inversion. The misfit between observed and synthetic spectrum is

used as weight w in the tomographic inversion for Q_p. Fig. 5.2 shows four examples of the spectral analysis of an event located in the Tarutung basin and Fig. 5.3 shows the Q_p values recorded by each station (Fig. 5.4 gives the location of the 229 events used).

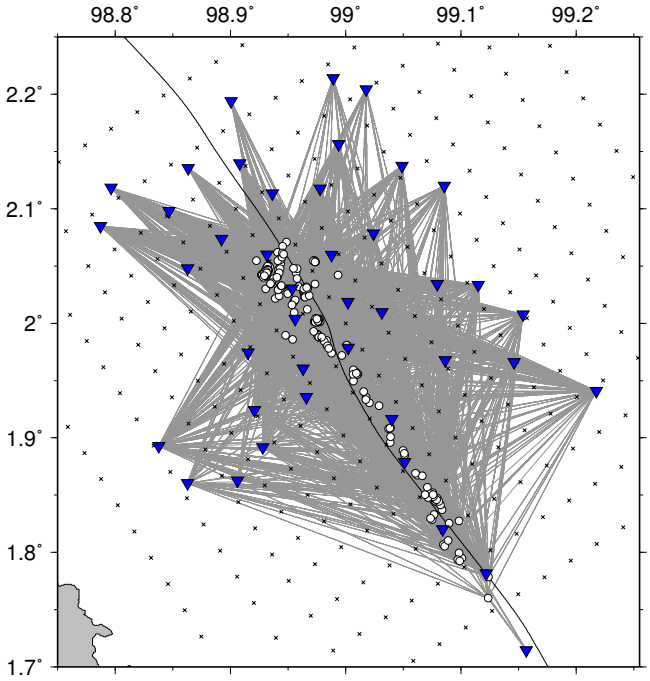

Figure 5.4: The design of the 3 x 3 km grid node spacing rotated parallel the Sumatran Fault. The gray lines represent the ray-paths propagate from events (white circles) to stations (blue triangles). The small cross marks represent the nodes.

The uncertainty of the data is derived from the assessment of t^* of similar source receiver ray-paths for which we expect similar values. We divided the region into 500 x 500 x 250 m cells and analyzed all t^*-values originating from an identical cell and recorded by the same station. We considered the cell containing at least two events recorded by the same station and finally we obtained and analyzed 436 data points. Fig. 5.5a shows the t^*-values having consistent deviation values relative to their averages. The standard deviation of the t^*-data of similar ray-paths is found to be 0.006 s as shown in Fig. 5.5b. We assume that this value is representative for the uncertainty of our t^*-data set. Some previous studies found a variation of data uncertainty depending on the t^*-values (i.e. Haberland & Rietbrock 2001 observed higher uncertainties for larger t^*-values), however our data shows a relatively constant data uncertainty. Very similar t^*-values of almost the same ray-paths (from different, however, closely located earthquakes having different source characteristic)

corroborates the assertion that our spectral inversion method can indeed successfully separate between path and source effects.

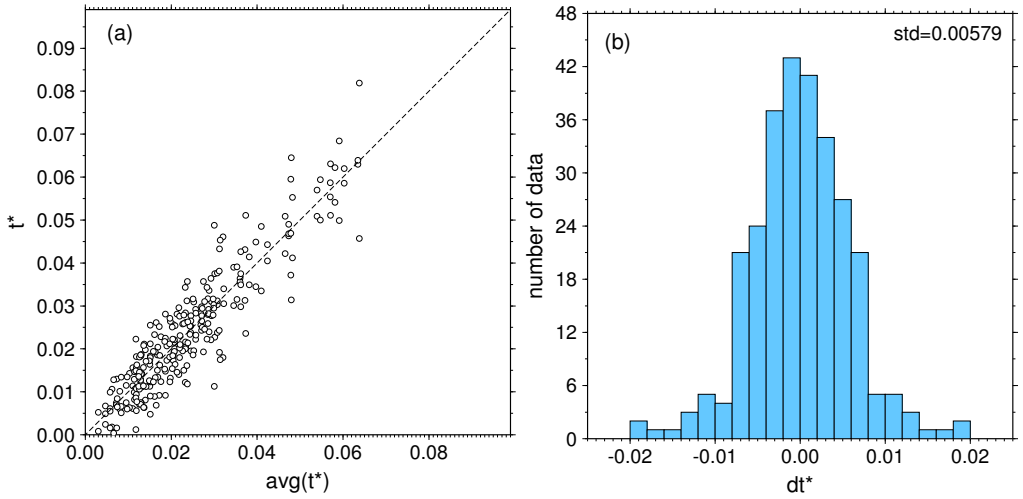

Figure 5.5: For estimating the uncertainty of the derived t^*-values, we compared the t^*-values of similar ray-paths, i.e from collocated earthquakes (within 500x500x200 m blocks) observed at a particular station. (a) Comparison between t^*-values and the average of t^* of each cell, (b) The standard deviation is 0.006 s which we assume to be the average uncertainty of the t^*-values.

5.4.2 Attenuation tomography

Having determined the t^*-values of all source-receiver configurations, the 3D absorption structure Q_p^{-1} was derived by using the SIMUL2000 tomographic inversion code (Thurber, 1983; Eberhart-Phillips and Michael, 1998; Rietbrock, 2001). The 3D model grid was centered at 99.0^0 E and 2.0^0 N and was oriented following the trend of the major structures within the study area. The node spacing was chosen as 3 x 3 km laterally (Fig. 5.4) and 2 km vertically in the central part of the model. Outside this area or deeper than 16 km (the maximum of the events depth), the grid nodes are spaced coarser. We use the same grid spacing as in the traveltime tomography (Vp, Vp/Vs)(Muksin et al., 2013a). Considering an average station distance of around 5 km we choose a lateral node spacing of 3 km. Vertical node spacing is chosen smaller since the velocity structure is layered vertically (Kissling et al., 1994) and seismicity is distributed in a narrow depth range (between 6 to 16 km). Muksin et al. (2013a) demonstrated that with this chosen node spacing the consistent and stable Vp and Vp/Vs velocity models were achieved with very low RMS values.

The Q_p inversion was started from a homogeneous model with a constant Q_p of

165. This value is the average of all the path-averaged quality factor $Q_{\mathrm{p}}(r)$ for all source and receiver pairs. The P velocity model was taken from the 3D traveltime tomography of Muksin et al. (2013a). P velocity, hypocenter coordinates, and origin times were not modified during the Q_{p} inversion. The trade-off curve between the variance of data misfit and the model variance was used to determine the damping factor for the inversion (Eberhart-Phillips, 1986).

5.4.3 Assumptions and limitations

Our method is based on a number of assumptions, which are summarized here. Often, a frequency-dependent Q_{p} is assumed (often a power law formulation, $Q(f) = Q_0 f^{\alpha}$, with $0 < \alpha < 1.0$), from laboratory studies (e.g. Faul et al., 2004) to regional (Atkinson, 2004) and global studies (e.g. Anderson and Given, 1982). We have checked this assumption in our data and ran different inversions for different values of α. The best overall spectral fit was achieved with $\alpha = 0.0$, however, moderate values of α between 0.0 and 0.2 gave similar good spectral fits. This finding confirms results from other studies which also found best fits for frequency-independent Q (Rietbrock, 2001; Bohm et al., 2013). However, frequency-independent Q would be higher, and this should be considered when comparing results to different studies (see e.g., Eberhart-Phillips and Chadwick, 2002). Nevertheless, we interpret mainly the relative attenuation anomalies (shape, location, and size) and not the absolute Q values, so this issue is not affecting our conclusions.

We assume that both intrinsic and scattering attenuation contribute to the total (or apparent) measured attenuation. In the interpretation we assume that Q_{p} is dominated by intrinsic attenuation and not by scattering; however, we have not quantified it yet (topic for future study). Nevertheless, we think that intrinsic attenuation is more prominent in our data since we do not observe long coda indicating strong scattering effects in our records and we analyze the early part of the seismogram mainly including direct wave energy. We assume a frequency-independent geometrical spreading. Due to the spherical divergence the amplitude of body waves in a homogeneous medium decrease with $1/r$. Realistic velocity models are known to produce a more complex amplitude behavior, and head waves, surface waves and guided waves even show frequency-dependent geometrical spreading (e.g., Yang et al., 2007; Morozov, 2010). In our data set we only expect body P waves (Pg up to ~40 km) for which we expect a $1/r$ geometrical spreading, not Pn, Sn, Sg, Lg, and surface waves. We calculate the attenuation from the spectral decay - frequency-independent geometrical spreading would not bias our t^* estimates.

We assume an ω^2 source model (e.g. Aki, 1967; Aki and Richards, 1980). For a dataset from Japan and using a similar analysis technique Rietbrock (2001) found that the ω^2 model gave significantly better spectral fit than the ω^3 model. We expect a similar behavior in our dataset.

5.5 Resolution and recovery tests

The quality of our tomographic model is examined by evaluating the model resolution matrix and the spread function (Toomey and Foulger, 1989). The spread values (represented by the gray color scale in Figs 5.6e-f and 5.7g-i) describe how well a model node parameter is resolved and how other nodes at some distance influence the resolution of a particular node. To assess the smearing of each node, we visualize the contour lines of the model resolution (represented by red contour lines in Figs 5.6e-f and 5.7g-i) for each node (Eberhart-Phillips and Michael, 1998). The model nodes with small spread function values and localized contour lines are considered to be well-resolved. The quality of the inversion results is also investigated by using two different recovery tests: checkerboard tests and synthetic tests with characteristic models.

The checkerboard recovery tests complement the resolution matrix analysis providing the information of how the inversion could resolve arbitrary given anomalies. For the checkerboard tests the background model $Q_\mathrm{p} = 165$ (according to the background model for the real inversion) is perturbed by -100 and +250, respectively, for the low and high Q_p anomalies. Each anomaly covers four grid nodes laterally and 2 in vertical direction as shown in Fig. 5.6a and b. The high and low Q_p imposed anomalies are indicated by red and blue colors, respectively.

The characteristic synthetic model was constructed based on the results of the real inversion and the tectonic setting of the area to investigate the resolution of the expected anomalies. In the characteristic models we imposed high attenuation anomalies (low Q_p) along the basins, around the Martimbang young volcano (south-west of Tarutung) and in the north-east of Tarutung where the major fluid discharges are situated. The low Q_p for the characteristic synthetic model is derived by perturbing the background model $Q_\mathrm{p} = 165$ by -100. The characteristic synthetic model is represented by the red shapes in Fig. 5.6c and d. To simulate realistic conditions in these recovery tests, we added Gaussian noise with a standard deviation of 0.0058 s to the synthetic t^*-data for both, the checkerboard and characteristic models, based on the uncertainty estimations described in section 4.2.

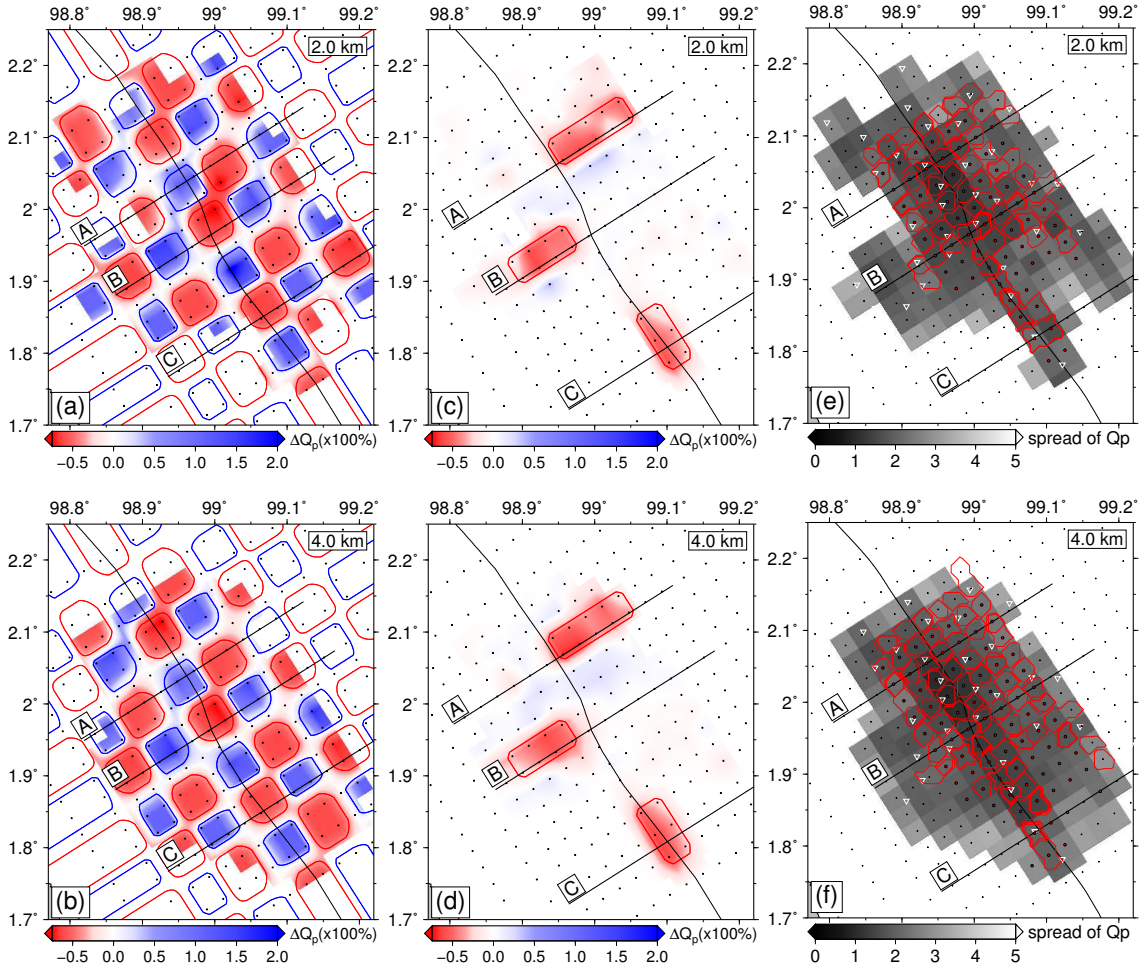

Figure 5.6: The checkerboard, characteristic models, spread function, and resolution matrix at depth of 2 and 4 km used to analyze the quality of the results. (a) and (b) show the checkerboard recovery results. The blue (red) boxes indicate the high (low) Q_p-values. (c) and (d) represent the characteristic feature recovery tests. (e) and (f) show the spread values (represented by the gray color bar) and the contour lines of model resolution matrix (red contour lines) in map view.

Some smearing in the checkerboard tests is produced among blocks containing similar anomalies represented by the presence of the shaded anomalies with small amplitude. The analysis of smearing is complemented by the analysis of the resolution matrix designated by the red contour lines in Figs. 5.6e-f. The checkerboard test results show that the high and low attenuation anomalies could be resolved and the images are not influenced by the distribution of the events. The application of the error (Gaussian noise) does not significantly alter the inversion results of the synthetic tests which means that the error of the data is still in a tolerable range.

Small spread function values (represented by the gray color bar in Fig. 5.6e-f) with

the 70% smearing contour line at different depth indicate well-resolved nodes with relatively less horizontal smearing in the vicinity of the Tarutung basin (in the north) where the major geothermal manifestations are located.

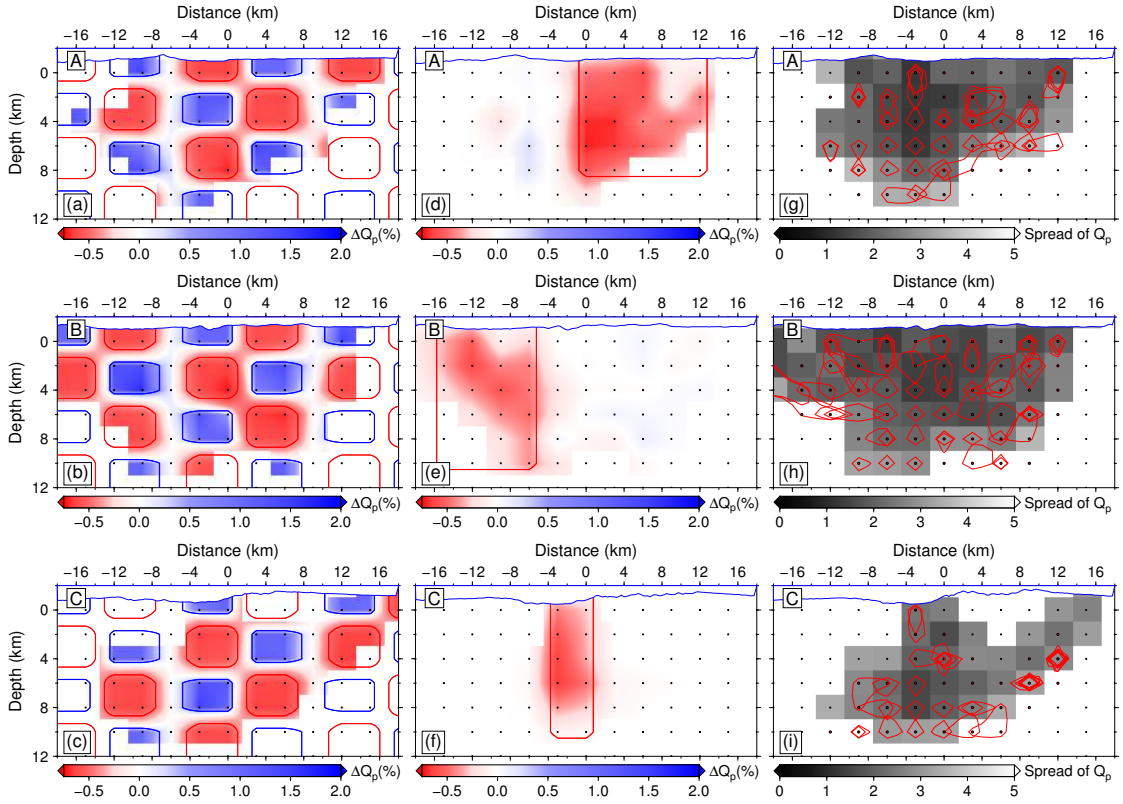

Figure 5.7: (a)-(c) Checkerboard recovery results along the cross-sections A, B, C indicated in Fig. 5.6a-b. (d)-(f) The characteristic feature recovery tests along the cross-sections A, B, C drawn in Fig. 5.6c-d. (g)-(i) The spread values (represented by the gray color bar) and the contour lines of model resolution matrix (red contour lines) in vertical view along the cross-section A, B, C indicated in Fig. 5.6e-f.

In accordance with the spread function, both, the checkerboard and the characteristic models are resolved and better recovered at deeper regions. These synthetic tests show that similar high attenuation anomalies located in the northern part around Tarutung could be imaged in the inversion of the real data. To the south, along the Sarulla graben, the nodes are well-resolved only along the Sumatran fault as the stations could only be located along the accessible roads close to the Sumatran fault. The nodes outside the fault line are influenced by the nodes along the fault line as indicated by smearing contours of the model resolution matrix. Therefore, the only anomalies resolved are the ones along the main fault or in the vicinity of the Sarulla graben as demonstrated by the recovery tests (Figs 5.6a-b).

Fig. 5.7 shows the vertical view of the spread function values (represented by gray color scale) and the smearing contour lines (red contour lines), as well as the recovery test results along the lines indicated in Fig. 5.6 which indicates a good resolution of our inversion results around the Tarutung basin (in the north of Tarutung district). The nodes out to 8 km to the right and the left from the Sumatran fault line are resolved, but experience smearing effects by their neighbors. Vertically, both the checkerboard and the characteristic anomalies are well resolved around the Tarutung basin and only anomalies close to the fault are recovered in Sarulla.

The comparison of the distribution of the spread function with the region with good recovery of the synthetic structures indicates that model regions with a spread value of 2.5 and below are well resolved. Accordingly, we show only these model regions in Fig. 5.6 and Fig. 5.7.

5.6 Results and discussion

Fig. 5.8-left shows the map view of the attenuation structure of the region at different depth levels while Fig. 5.9-left displays the vertical images of the structure along the cross-sections (A, B, C, and D marked in Fig. 5.8). In order to enrich the discussion, we complement Fig. 5.8 with the map view of the Vp (Fig. 5.8-middle) and Vp/Vs structure (Fig. 5.8-right). We also include the vertical view along the four cross-sections of the Vp (Fig. 5.9-middle) and the Vp/Vs structure (Fig. 5.9-right) obtained from Muksin et al. (2013a). The results of the analysis of the data and the model quality from the spread function and the recovery tests confirmed the good resolution of the 3-D Q_{p} structure of the Tarutung geothermal area. Accordingly, we only show the structure located in the areas containing well-resolved nodes based on small spread function values. We have experimented applying different damping parameter for station correction used in damped least-square inversion to investigate the ambiguity of the tomography results. The higher damping parameter we apply, the lower station correction we observe. With different damping parameter, even with an extreme damping parameter (zero station correction), the shape of the anomalies is relatively stable but the amplitude of the anomalies becomes more prominent and larger. Here, we use the damping parameter for station correction which produces the station correction in the average of ~0.003 s which is smaller than the data uncertainty 0.006 s.

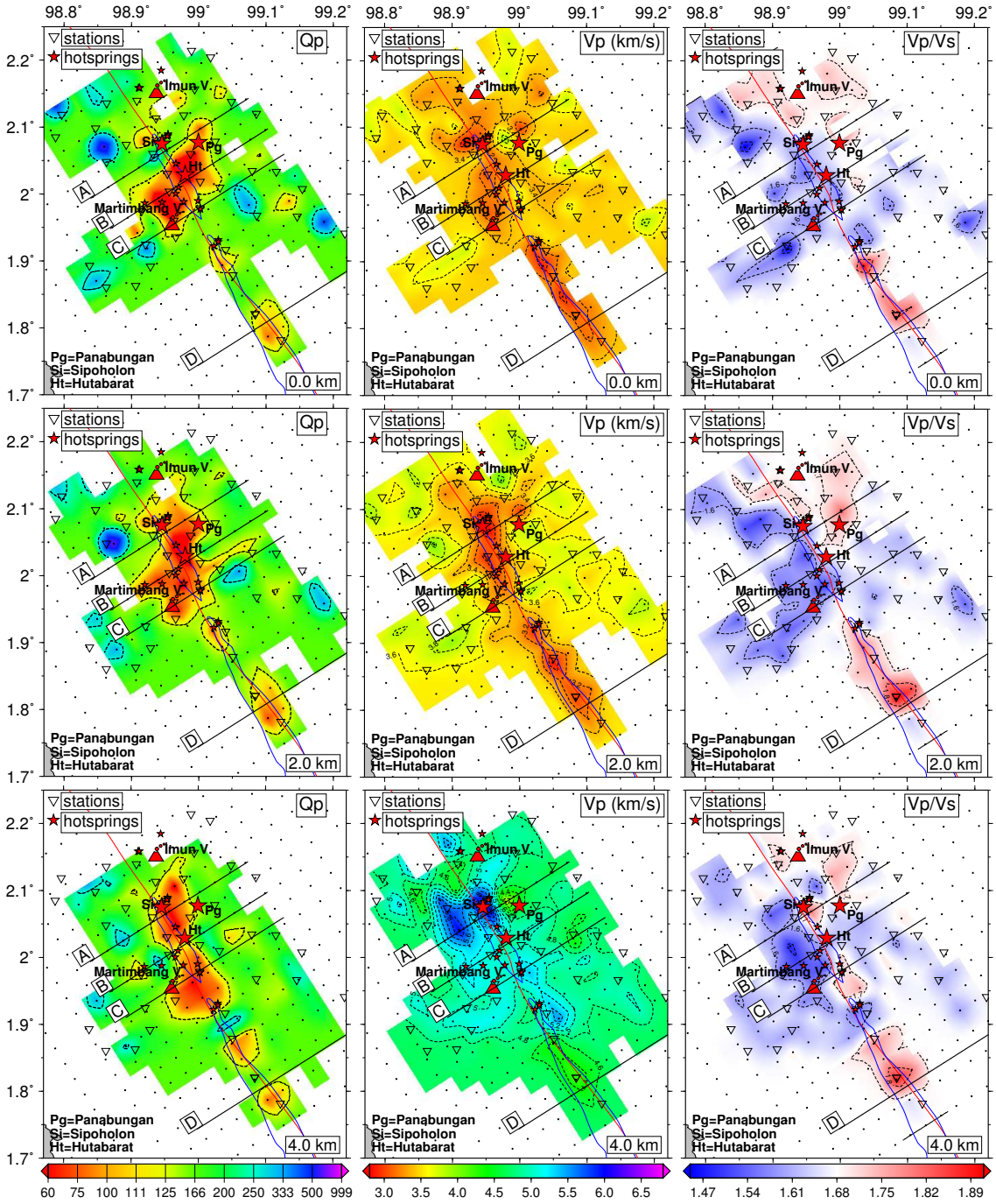

Figure 5.8: The map view of the attenuation structure (LEFT), the Vp structure (MIDDLE), and the Vp/Vs structure (RIGHT) at depth of 0, 2, and 4 km. The structure along the profile A, B, C, and D are shown in Fig. 5.9. The blue contour lines along the fault symbolize the Tarutung basin (in the north) and Sarulla graben (in the south). The Vp and Vp/Vs structure are obtained from Muksin et al. (2013a).

In general the low Q_{p} anomalies (high attenuation zones) are in a good agreement with the low Vp anomalies. We observe four different groups of high attenuation zones (Fig. 5.8) with Q_{p}< 100: (1) along the Tarutung basin at depth shallower than ~2 km, (2) in the north-east of the Tarutung basin where the three major and high temperature geothermal manifestations (Sipoholon, Hutabarat, and Panabungan) are located, (3) within the vicinity of the Martimbang young volcano, just southwest of Tarutung basin, along the cross-section B in Fig. 5.8, and (4) along the Sarulla graben especially within the area of the Hopong caldera (see also Fig. 5.1).

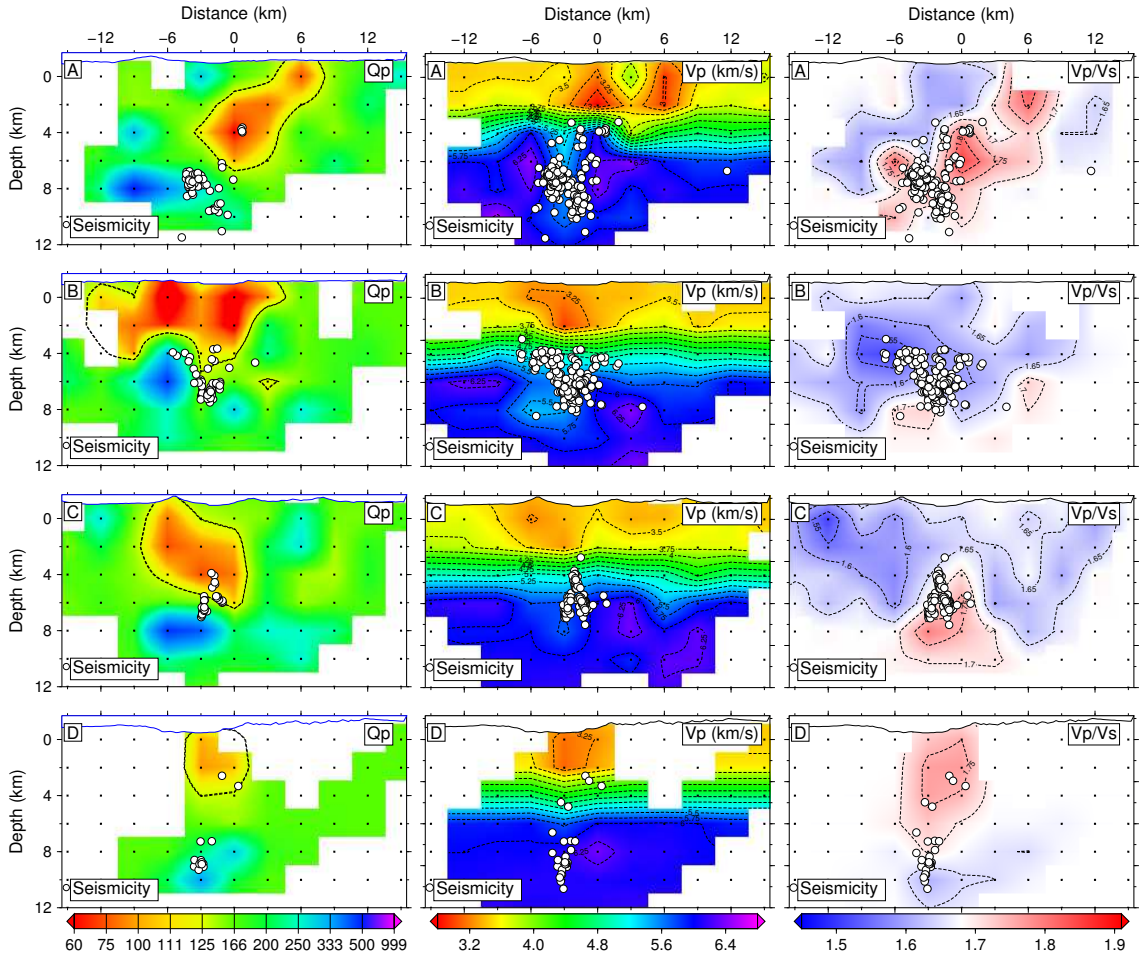

Figure 5.9: The vertical cross-section along the 4 profiles (A, B, C, and D indicated in Fig. 5.8) of: the Q_p structure (LEFT), the Vp structure (MIDDLE), and the Vp/Vs structure. The Vp and Vp/Vs structures are obtained from Muksin et al. (2013a).

From the description above, seismic attenuation seems to be mainly controlled by physical properties such as temperature, pressure, and porosity (Mavko, 1980; Sato

et al., 1989). Hence, the attenuation tomography results complement the velocity models and contribute to a consistent interpretation. The material properties related to the attenuation and seismic velocity derived from laboratory works and tomography results are presented in Table 5.1.

Table 5.1: Summary of material properties related to attenuation and seismic velocity based on laboratory experiments (lab) and field experiments (field)

Characteristic of Q, Vp, Vp/Vs and other geophysical properties	**Lab/ Field**	**Reference**
Qp decreases rapidly with increasing temperature	Lab	Sato et al. (1989)
Low Qp correlated with the increase of the melting volume correlating and high temperature	Lab	Mavko (1980)
Qp decreases as the increase of fluid content	Field	Haberland & Rietbrock (2001)
Sedimentary basin and magmatic in Central Java (Qp < 100; low Vp; high electrical conductivity)	Field	Bohm et al. (2013)
Ventura basin California (low Qp < 100)	Field	Hauksson & Shearer (2006)
Low Vp and High Vp/Vs is related to high fluid saturation	Field	Julian et al. (1996); Husen et al. (2004); Haberland et al. (2009)
Low Q, low Vp, and low Vs beneath Mt. Guntur complex	Field	Priyono et al. (2011)
Gas filled volume beneath the Yellowstone caldera (Low Vp and Low Vp/Vs)	Field	Husen et al. (2004)
Change from liquid to vapor-rich state after extensive exploitation in the Geyser geothermal field (Low Vp and Low Vp/Vs)	Field	Julian et al. (1996)
CO2 emission beneath the Mammoth Mountain in the Long Valley caldera (Low Vp and Low Vp/Vs)	Field	Julian et al. (1998)

5.6.1 Tarutung Basin and Northeast Tarutung

The attenuation result shows high attenuation along the Tarutung basin with Q_{p} lower than 100 at shallow depth (< 2 km) (Fig. 5.8-left and Fig. 5.9-left). This low Q_{p} correlates with the low velocity (Muksin et al., 2013a) (Fig. 5.8-middle and Fig. 5.9-middle) and high electrical conductivity measured by the magnetotellurics (Niasari et al., 2012). Low Q_{p} zones related to the sedimentary basin are also found in other areas as briefly described in Table 5.1. Bohm et al. (2013), for example, found high attenuation ($Q_{\mathrm{p}} < 100$) in Kendeng Basin south of the modern volcanic arc in Central Java. At shallow depths Hauksson and Shearer (2006) found low Q_{p} (<=100) along the Ventura and Los Angeles basin in southern California, USA. We suggest that the low Q_{p} along the Tarutung basin is related to unconsolidated material and high porosity of the sedimentary deposit mostly filled by the Toba tuff 74,000 years ago from the great Toba eruption (Hickman et al., 2004).

The lowest Q_{p}-values (~40) are observed in the area of the geothermal manifestation in the north-east of Tarutung. Usually, within the volcanic and geothermal areas, significantly low Q_{p} values are observed. Wu and Lees (1996), for example, observed an average of Q-values of ~30 within the area of Coso hotsprings, California-USA. High attenuation in the north-east of Tarutung (Fig. 5.8-left and profile A in Fig. 5.9-left) is in good agreement with a high Vp/Vs zone (Fig. 5.8-right and profile A in Fig. 5.9) and is also consistent with a high electrical conductivity anomaly obtained from a preliminary modeling of magnetotelluric data (Niasari et al., 2012). We suggest that this region of high attenuation, low Vp, high Vp/Vs, and high electrical conductivity is related to high fluid content. This conclusion is supported by the fact that the anomaly is surrounded by the three prominent geothermal manifestations. These three major manifestations have different physical characteristics. In Panabungan and Hutabarat, the hot springs have a similar temperature of 50^0C and 53^0C, respectively, high fluid flow rate, and are localized in small areas. On the other hand, in Sipoholon, the temperature of the hot spring is higher ($\sim 60^0$C) and several small hot springs with less flow rate are distributed within a wider area and also characterized by the presence of travertine.

Although these three major manifestations have different temperature and apparent characteristic, they seem to originate from the same source from below the fault as shown in profile A of Q_{p} structure in Fig. 5.9-left, as also confirmed by the Vp/Vs tomography (profile A of the Vp/Vs structure of Fig. 5.9-right). We suggest that hot fluids from the same source are moving along different path ways to the surface resulting in the variations of the physical characteristics of the geothermal manifestations

(such as temperature and rock porosity). The reason of the northeastern trend of the fluid flow remains unsolved. To the east the rocks might be more permeable as also indicated by low resistivity (Niasari et al., 2012). Alternatively (or in addition), to the northeast of the Tarutung basin several normal faults are found (indicating dilatation in this region) which could act as pathways for the fluid. From this analysis and our interpretation we conclude that the shallow geothermal system in the northeast of Tarutung is more controlled by the fault structure rather than by volcanism.

However, the high Vp/Vs anomaly is located more to the east, while the low Q_{p} zone is located closer to the basin. We suggest that Vp/Vs is more sensitive to high fluid content and images the higher flow rate geothermal potential represented by Panabungan manifestation. The Q_{p}, on the other hand images the higher temperature geothermal potentials represented by the manifestation Sipoholon and Hutabarat and also the higher flow rate geothermal potential (Panabungan).

5.6.2 Martimbang volcano

Just to the southwest of the Tarutung basin, high attenuation is found in the vicinity of the Martimbang volcano (Fig. 5.8-left). At 2 to 3 km depth, the area of high attenuation (low Q_{p}) is located just below the volcano. However, Muksin et al. (2013a) could not find a high Vp/Vs anomaly (Vp/Vs structure in Fig. 5.8-right) below the Martimbang volcano. Both Q_{p} and Vp/Vs are influenced by the physical properties such as pressure, temperature, and pore fluids. According to laboratory results (Sato et al., 1989) and tomography results (e.g. Artemieva et al., 2004), attenuation significantly depends on temperature of rocks. On the other hand, compared with attenuation, Vp/Vs values depend less significant on temperature changes (Wang and Nur, 1990) and the effect might be too small to be observed in the tomography anomaly (Husen et al., 2004).

Several authors (e.g. Priyono et al., 2011) suggested that low Q_{p}, Vp, and Vs beneath volcanoes are related to magmatic system. Others associate the low Vp/Vs anomalies within geothermal or volcanic areas with an increase of gas content. Husen et al. (2004), for example, interpreted a low Vp and low Vp/Vs zone as a gas filled volume beneath the Yellowstone volcanic field. Julian et al. (1996) observed a significant decrease in Vp/Vs in the most exploited reservoir in the Geyser geothermal production field because of the change from liquid to vapor-rich state after extensive exploitation. Julian et al. (1998) found a low Vp/Vs anomaly related to the CO2 emission beneath the Mammoth Mountain on the southwestern rim of Long Valley caldera, California

(USA). The decrease in Vp/Vs due to the gas content pore fluid is caused by the very low bulk modulus of gas compared with that of liquids. Takanami et al. (2000) suggested that low Q and low seismic velocity beneath the Sawauchi volcanic front in northeastern Japan is related to a high temperature zone without partial melting (very locally partial melting). However, in the area of the Martimbang volcano, there is no gas or vapor manifestation observed. In conclusion, we suggest that the low Q_{p} in the region without Vp/Vs anomaly (normal Vp/Vs) below the Martimbang volcano is associated with high temperature structure with a small amount of fluid or high temperature without or with a small amount of partial melting. At 4 km depth (Q_{p} structure in Fig. 5.8), the high attenuation anomaly is located close to the Sumatran fault. This high attenuation could be interpreted as the pathway of the magma and/or hot fluid/gas of the Martimbang volcano fed from below the fault and transported to the left (southwest) of the fault as described in profile C in Fig. 5.9-left.

5.6.3 Sarulla region

The limited resolution of the inversion only allows us to image the structure in Sarulla region just below the Sumatran fault. We found low Q_{p} anomaly along the basin, consistent with low Vp, low Vs and high Vp/Vs (Muksin et al., 2013a). The low Vp and high Vp/Vs along the Sarulla graben is associated with a weak fault zone, caused by the volcanism, where numerous earthquakes occur along the graben. The high Vp/Vs could be also influenced by the high pressure of high temperature fluid flow in the area as revealed by drilling results (Hickman et al., 2004). However, the low Q_{p} zone is located more to the south within the vicinity of the Hopong caldera (See Fig. 5.1 for the topography comparison). Therefore, we interpret low Q_{p} as being caused mainly by the presence of hot magma below the caldera and also by graben sediment. The heat source is still fed to the caldera along the fault system from below directly to the surface (Profile D of Q_{p} and Vp/Vs structure in Fig. 5.9). Therefore, the presence of the Hopong caldera could significantly contribute to the control of the geothermal system in this area.

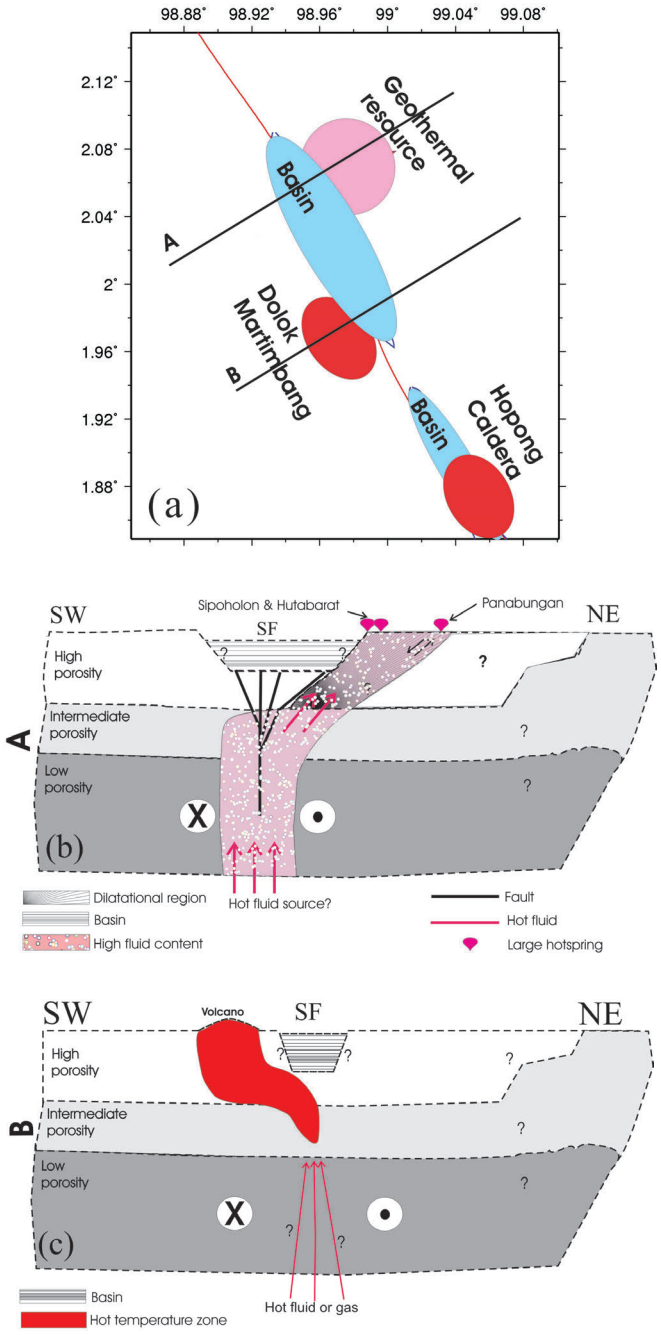

Figure 5.10: The new conceptual model derived from the attenuation tomography and complemented by the Vp/Vs tomography results (Muksin et al., 2013a) describing 4 different clusters in Tarutung (a) The map view of the new conceptual model of the Tarutung geothermal field, (b) The structure of the Tarutung geothermal area along the cross-section A, and (c) The magmatic system of the Martimbang volcano indicated by the profile B. The hot fluid/ gas is fed along the fault and transported to the southwest of the Sumatran fault.

5.6.4 Conceptual structure of the Tarutung region

From the results and the discussion above we can summarize the features of the attenuation properties derived from the attenuation tomography and complemented by the Vp and Vp/Vs tomography as shown in Table 5.2 and in the conceptual model in Fig. 5.10. The layering in the model is derived from the Vp structure while characteristics of the geothermal system are derived from the Vp/Vs and the Q_{p} structure.

Table 5.2: Low Qp zone associated with the characteristic of the structure

Areas	**Characteristic**	**Interpretation**
Along the basin	Low Qp (< 100), and low Vp	Sedimentary deposit
Southwest of the basin	Low Qp (< 100), normal Vp and Vp/Vs	Martimbang volcano
Northeast of the basin	Low Qp (< 100), low Vp and relatively low Vp/Vs	Hot fluid related area coincides with the location of the large hot springs
South of Tarutung (along the Sarulla graben)	Low Qp (< 100), low Vp, low Vs, and high Vp/Vs	Hopong caldera and weak fault zone

The Tarutung area consists of three main clusters (Fig. 5.10a): The Tarutung basin, the magmatic system (southwest of Tarutung basin) and the geothermal resource (northeast of the Tarutung basin). The shape of the Tarutung basin (light blue Fig. 5.10a) obtained from the Vp model (Muksin et al., 2013a) correlates well with the geometry of the basin derived from the topography with depth of around 2 km (Fig. 5.8-middle). The geothermal potential manifested by the three big hot springs (Sipoholon, Hutabarat, and Panabungan) in the eastern Tarutung is imaged by the red zone. The hot fluid for all geothermal potentials is fed from below the fault (Fig. 5.10b). We found almost exactly similar pattern between the high Vp/Vs and high attenuation anomalies in the northern Tarutung (profile A in Fig. 5.10a). Therefore the attenuation tomography validates and strengthens the previously proposed conceptual model obtained from Vp and Vp/Vs tomography (Muksin et al., 2013a) as shown in Fig. 5.10b.

The red zones in the southwest of the Tarutung basin and in Sarulla (Fig. 5.10a) represent the magmatic system in the region. Fig. 5.10c describes the magmatic system of the Martimbang volcano where the partial melt diapir is transported from the mantle along the fault zone. The conceptual model along the Sarulla basin is similar to the one proposed in the Vp and Vp/Vs conceptual model (See Fig. 19 in Muksin et al., 2013a).

5.7 Conclusion

We have produced a well resolved Q_{p} structure of the Tarutung geothermal area correlating with geothermal prospects and volcanism. Our study confirms that attenuation tomography is a powerful tool for the exploration of a geothermal site in a seismically active region. In Tarutung, the high attenuation zones are found along the Tarutung basin associated with the basin sediment and in the northeast of Tarutung where the geothermal potentials are located. We image the magmatic system of the Martimbang volcano in the southwest of the Tarutung basin showing the magma is fed along the fault and transported to the south west of the Sumatran fault. The low Q_{p} along the Sarulla graben is interpreted as the presence of the hot magma below the Hopong caldera. The geothermal system in Tarutung seems to be controlled mainly by the fault setting where the source of the hot fluid is originated from below the fault and transported to the northeast.

Acknowledgements

This work is part of the project "Sustainability concepts for exploitation of geothermal reservoirs in Indonesia-capacity building and methodologies for site deployment" funded by the German Federal Ministry of Education and Research (BMBF) under grant 03G0753A. At the Indonesian side, we wish to thank the Center for Geological Resources (the Indonesian governmental agency responsible for geothermal exploration) and the local government of North Tapanuli (Tarutung), North Sumatra for their support. The instruments for the experiment were provided by the Geophysical Instrument Pool Potsdam (GIPP). The authors wish to thank Prof. Dr. Inga Moeck and Mochamad Nukman for fruitful discussions on the geological setting of the study area based on their field observations. Particular thanks go also to all colleagues who participated in the field work. We would like to thanks to Dr. Nick Rawlinson and the anonymous reviewer for their positive and constructive comments and suggestions.

Chapter 6

Detailed fault structures in the Tarutung geothermal area derived from local earthquake data

Umar Muksin[1,2], Christian Haberland[1], Mochammad Nukman[1,3], Klaus Bauer[1], Michael Weber[1]

[1]German Research Centre for Geosciences GFZ, Potsdam, Germany
[2]Department of Physics, Syiah Kuala University, Banda Aceh, Indonesia
[3]Department of Geophysics, Gadjah Mada University, Jogjakarta, Indonesia
Contact: muksin@gfz-potsdam.de

Published 2014 in Journal of Asian Earth Sciences, 96, pp. 123-131

Abstract

The Tarutung Basin is located at a right step over in the northern central segment of the dextral strike-slip Sumatran Fault System (SFS). Details of the fault structure along the Tarutung Basin are derived from the relocations of seismicity as well as from focal mechanism and structural geology. The seismicity distribution derived by a 3D inversion for hypocenter relocation is clustered according to a fault-like seismicity distribution. The seismicity is relocated with a double-difference technique (hypoDD) involving the waveform cross-correlations. We used 46,904 and 3,191 arrival differences obtained from catalogue data and cross-correlation analysis, respectively. Focal mechanisms of events were analyzed by applying a grid search method (HASH code). Although there is no significant shift of the hypocenters (10.8 m in average) and centroids (167 m in average), the application of the double-difference relocation sharpens the earthquake distribution. The earthquake lineation reflects the fault system, the extensional duplex fault system, and the negative flower structure within the Tarutung Basin. The focal mechanisms of events at the edge of the basin are dominantly of strike-slip type representing the dextral strike-slip Sumatran Fault System. The almost north-south striking normal fault events along extensional zones beneath the basin correlate with the maximum principal stress direction which is the direction of the Indo-Australian plate motion. The extensional zones form an en-echelon pattern indicated by the presence of strike-slip faults striking NE-SW to NW-SW events. The

detailed characteristics of the fault system derived from the seismological study are also corroborated by structural geology at the surface.

Keywords: focal mechanism, seismicity, structural geology, extensional duplex, flower structure, Sumatran Fault, pull-apart basin.

6.1 Introduction

The convergence between the Indo-Australian and Eurasian plates has produced the subduction zone beneath Indonesia. The shape of the subduction zone beneath Sumatra collocates with the volcanic arc (Fig. 6.1) as also often found in other areas (e.g. Tatsumi, 1989). In case of oblique subduction, a trench-parallel strike-slip fault system can occur along the volcanic arc. The Liquiñe-Ofqui Fault Zone accommodating the northward motion of a continental forearc sliver relative to the South-American continent (Cembrano et al., 1996; Lange et al., 2008) and the San Andreas Fault System taking up most of the shear component (Teyssier et al., 1995) are among the examples of this case. The 1650 km long strike-slip Sumatran Fault accommodates the trench-parallel shear component of this convergence along the magmatic arc (Bellier and Sébrier, 1995; McCaffrey, 2009; Sieh and Natawidjaja, 2000). Therefore, the shape of the SFS corresponds to that of the Sumatran subduction zone and the Sumatran volcanic arc (Sieh and Natawidjaja, 2000).

A geomorphological study of Sieh and Natawidjaja (2000) revealed that the SFS is partitioned into 19 major sections, mostly caused by the changes in the rate and direction of the Indo-Australian plate motion along Sumatra. This segmentation is characterized by several pull-apart basins caused by dilatational step-overs ((Muraoka et al., 2010; Sieh and Natawidjaja, 2000). Though the SFS is segmented, the magnitudes of earthquakes were large enough to devastate the region, such as the 1994 Mw 6.8 Liwa and the 2013 Mw 6.2 Aceh earthquakes.

The segments of the SFS show different characteristics (Sieh and Natawidjaja, 2000). In the southern part of the Sumatra island, the Sunda segment (6.75S to 5.9S) is characterized by normal and dextral faulting on the surface, as also indicated by normal fault earthquakes on the western side of the graben while reverse slip was found along the Kemuring segment (5.3-4.35 S). In central Sumatra, the SFS is characterized by the presence of a bifurcation around 0 - 1.7 N composed of segments (Sieh and Natawidjaja, 2000). Weller et al. (2012) observed a dextral strike-slip duplex system of the bifurcation linked by smaller sinistral strike-slip faults. The mechanism of the extensional duplex system along a bent strike-slip fault is responsible for the presence

of a flower structure as described in detail by Woodcock and Fischer (1986).

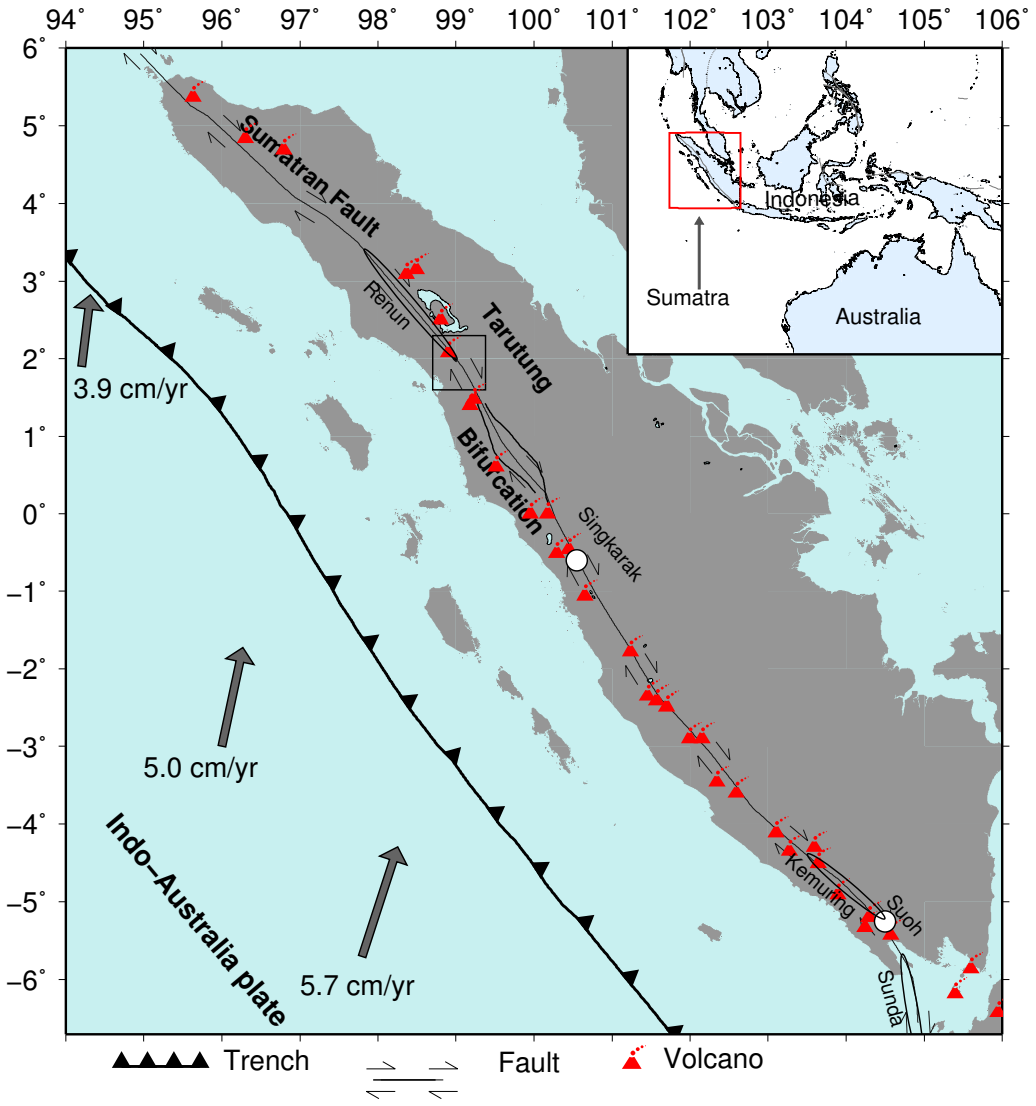

Figure 6.1: Regional tectonic setting of Sumatra and Tarutung district (box) is located between the Toba caldera and the bifurcation.

More to the north of the bifurcation, the SFS is characterized by the Renun segment which is the longest segment and one of the largest graben along the SFS traversing the western flank of the Toba caldera (Sieh and Natawidjaja, 2000). The Tarutung district, characterized by the Tarutung Pull-Apart Basin in the north and the Sarulla graben in the south is located between these two major features, the Toba caldera and the bifurcation segments (Fig. 6.1). Bellier and Sébrier (1994) suggested that the Tarutung Pull-Apart Basin was developed due to a larger step-over of the previous fault system and as the latest evolution of the great Toba caldera within the older

step-over region.

The Tarutung Basin hosts several geothermal manifestations (Fig. 6.2). At least 18 springs (i.e. cold and warm) discharge along the Tarutung Basin margins (Nukman and Moeck, 2013) and about 13 hot springs discharging in the Sarulla area (Gunderson et al., 1995). It has been suggested that the geothermal system in the Tarutung region is controlled by the fault system (Muksin et al., 2013a). Along the SFS, normal faults along pull-apart basins play an important role as major discharge zones for geothermal fluids (Muraoka et al., 2010). Therefore, it is important to study the fault system in the Tarutung region to understand the structural controls on the geothermal system in the region. This paper presents the fault structure along the Tarutung Basin derived from local earthquake seismicity, as well as the focal mechanism analysis enriched by geological field investigation.

6.2 Data and Methods

6.2.1 Previous work

The research started with the deployment of 42 short period seismic instruments for 10 months starting in May 2011, in the district of North Tapanuli, Sumatra, Indonesia (Fig. 6.2). The network covered the area of the Tarutung Basin in the north and the Sarulla graben in the south. The details of the seismic experiment and the data preprocessing are explained in (Muksin et al., 2013a) and (Muksin et al., 2013b). An automatic picking algorithm (Nippress et al., 2010) was used to detect the arrivals of P and S waves of earthquakes and then the arrivals were revised manually. We used HYPO71 (Lee and Valdes, 1985) with the velocity model based on the global model of IASP91 (Kennett and Engdahl, 1991) to produce the first estimate location of 2,586 earthquakes. The earthquake localization was then improved by using the simultaneous 1D inversion for hypocenter relocation and velocity (VELEST software, Kissling et al., 1994). The best velocity models and the earthquake location are achieved when the data variance decreases and the RMS misfit of the solution is minimum. We only accepted those events for the relocation recorded at least by 10 stations with an azimuthal gap angle less than 180^0.

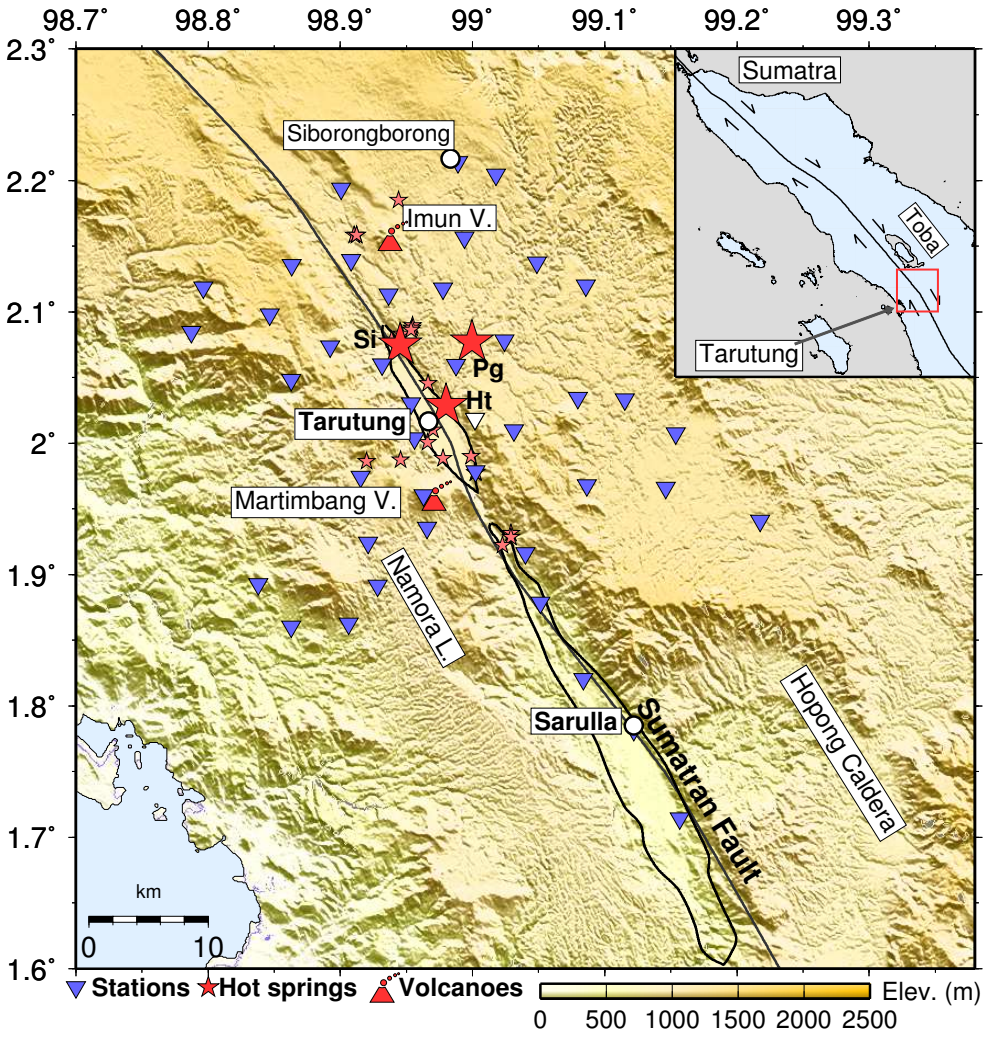

Figure 6.2: Station distribution covering the Tarutung and the Sarulla basin deployed for 10 month starting May 2011.

For simplification, the earth structure initially was assumed to consist of layers forming a 1D velocity model. We applied HYPO71 (Lee and Valdes, 1985) based on the global 1D velocity model of IASP91 (Kennett and Engdahl, 1991) to produce the first estimate location of 2,586 earthquakes. The earthquake localization was further improved by using the simultaneousinversion for hypocenter relocation and 1D velocity structure (VELEST software, Kissling et al., 1994). In In extension to the previous step (application of HYPO71 based on a fixed velocity-depth function), the 1D velocity model was now modified during the inversion together with the hypocenter locations to better explain the travel time data. Only events with a minimum of 10 station recordings were used in this inversion and subsequent steps. More details of the inversion using VELEST can be found in Muksin et al. (2013a). The final

1D layered velocity model obtained by VELEST was used to construct an initial 3D velocity structure. The 3D model consists of regularly spaced grid nodes with individual velocity values. A tomographic inversion was then carried out to determine the optimum velocity structure and seismicity distribution within this 3D model using the SIMUL2000 software (Eberhart-Phillips and Michael, 1998; Evans et al., 1994; Thurber, 1983). The iterative inversion procedure includes Approximate Ray Tracing (Thurber, 1983) to predict travel times, comparison with observed travel time data, and updates of velocity values and hypocenter locations using a damped least-squares algorithm. The iteration process is repeated until the RMS misfit between observed and predicted travel times is minimized. The details of the 3D tomographic inversion are presented in Muksin et al. (2013a).

6.2.2 New relocation and focal mechanism

The seismicity resulting from the 3D tomographic inversion was then relocated using a double-difference relocation scheme (hypoDD) (Waldhauser and Ellsworth, 2000). In general, earthquakes which occur along the same fault segment can be assumed to show similar source mechanisms, and, hence, produce similar waveforms at a receiver. The main idea of this technique is to minimize the residuals between the observed and the calculated traveltimes of neighboring events observed at one particular station. Two closely located events are considered to be neighboring, if the distance between the events is much smaller than the event-station distance and the size of the velocity heterogeneity (Waldhauser and Ellsworth, 2000). High-resolution relative hypocenters will be obtained when the residuals are minimized. The conjugate least squares inversion method is used in this technique.

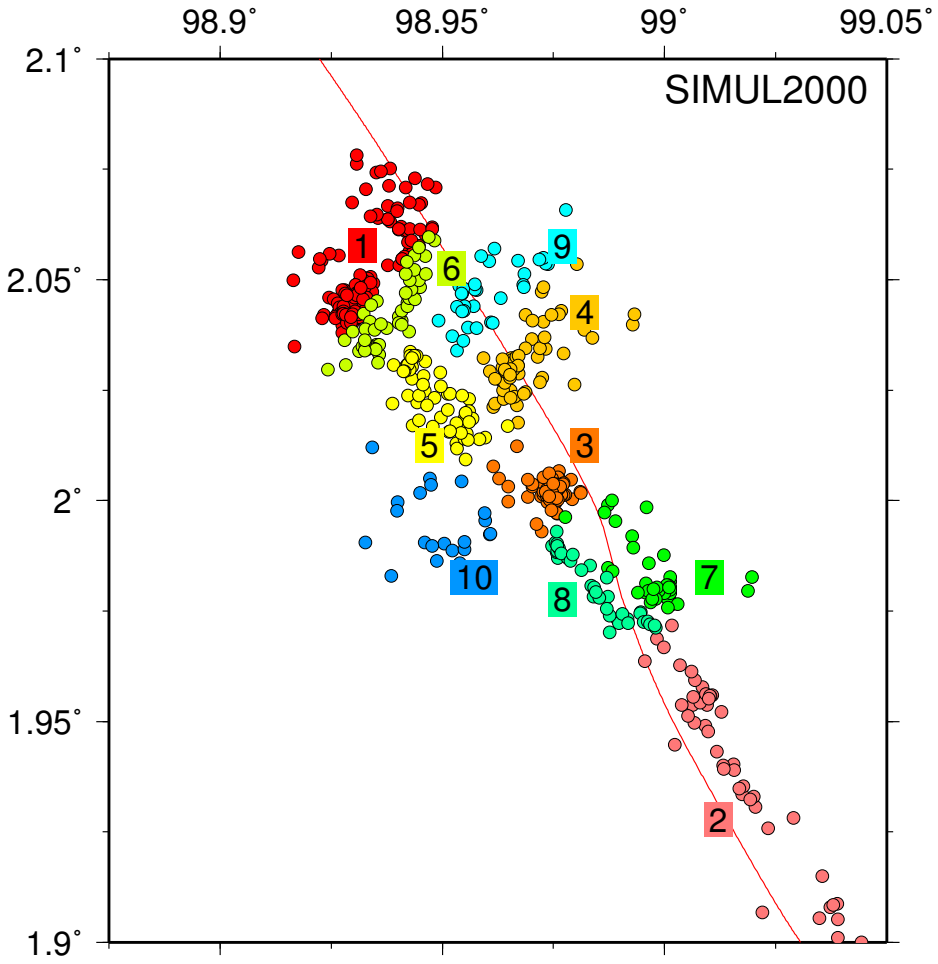

Figure 6.3: The clusters of the seismicity distribution obtained from the 3D inversion based on the delineation. The earthquakes are then relocated by using double-difference technique. Different colors represent different group of events.

We used the cross-correlation of waveforms in the relocation procedure. The resulting delineation of the earthquake distribution seems to form a micro-fault system around the basin. We then clustered the earthquakes into 10 groups based on this lineation (Fig. 6.3) indicated by different colors. The clustering was carried out in space. The maximum distance between an earthquake pair in each cluster was set 1 km. This configuration is plausible since input for the hypoDD was from the result of a 3 x 3 km grid size SIMUL2000 routine.

Using the double-difference relocation, the residual between the observed and the predicted arrival times for pairs of earthquakes recorded by a similar receiver is evaluated. The velocity model used in hypoDD relocation is the one obtained from VELEST which was also used for the initial model for the 3D tomographic inversion

(Muksin et al., 2013a). We used 46,904 and 3,191 arrival differences obtained from catalogue data and cross-correlation analysis, respectively. The neighbor threshold used was 10 links, with stations no more than 80 km from the event pairs. We constrained the arrival time differences obtained from cross-correlation less than 0.05 s and a correlation factor greater than 70%.

We calculated the focal mechanism of the events based on the visually inspected and manually picked first polarity of the P waves using the HASH software (Hardebeck and Shearer, 2002). In the analysis of the focal mechanism, we only include seismic events having more than 8 polarity records. The take-off angles for each observation are calculated based on the ray tracing in the 3D velocity model obtained from SIMUL2000. The seismicity distribution and the focal mechanisms are then compared with the surface geological field survey to better analyze the fault structure of the region.

6.2.3 Structural geology observation

Fault kinematic results from Tarutung rock outcrops by Nukman and Moeck (2013) are used to constrain the interpretation of the fault system in the area. The fault kinematics are derived from a striations and subsidiary fractures analysis (Nukman and Moeck, 2013). The measured trend of fractures, veins, and lineaments of thermal manifestations are also used in the fracture analysis by comparing their fracture attitude to the main fault orientation (Nukman and Moeck, 2013). Most of the structural measurements are taken from rock unit of Miocene to Recent age.

6.3 Results

From the hypoDD relocation we found, that after 16 iterations the average RMS of waveform cross-correlation and earthquake catalogue are 0.33 ms and 0.47 ms, respectively.

Table 6.1: Statistics of hypoDD relocation of 10 main clusters after 16 iterations. CC refers to cross-correlation and CT means catalogue.

Cluster	Number of events	Events mean shift				CC-RMS (ms)	CT-RMS (ms)
		x(m)	y(m)	z(m)	t(ms)		
1	188	33.5	25.5	9.9	0.1	0.59	0.49
2	151	2.5	3.2	16.7	0.6	0.20	0.47
3	76	7.7	7.2	7.9	0.1	0.46	0.53
4	58	1.8	0.9	14.7	0.4	0.35	0.44
5	58	4.6	5.7	1.3	0.0	0.24	0.47
6	52	4.3	3.6	1.2	0.1	0.41	0.50
7	39	1.1	1.5	11.5	0.3	0.31	0.43
8	39	0.2	1.8	4.1	0.1	0.32	0.47
9	34	1.9	1.6	4.7	0.4	0.32	0.55
10	21	0.9	1.0	1.8	0.2	0.15	0.42

Table 6.2: The mechanism quality criteria used in the focal mechanism calculation.

Quality	Average misfit	RMS fault-plane uncertainty	Station distribution ratio	Mechanism probability	Number of events
A	≤ 0.15	$\leq 25^0$	≥ 0.5	≥ 0.8	0
B	≤ 0.20	$\leq 35^0$	≥ 0.4	≥ 0.7	31
C	≤ 0.30	$\leq 45^0$	≥ 0.3	≥ 0.6	23
D	Maximum azimuthal gap $\leq 90^0$, maximum takeoff angle gap $\leq 60^0$				376
E	Maximum azimuthal gap $> 90^0$, maximum takeoff angle $> 60^0$				26
F	Fewer than 8 polarities				269

The average change in the hypocenter is 10.8 m and the average shift of centroids is 167 m. The largest change is contributed to the relocation of the first cluster which contains the largest number of earthquakes. The use of the double-difference relocation reduced the number of events from 809 to 735 because the outlier events were excluded. The summary of the relative relocation statistics is provided in Table 6.1.

Fig. 6.4 shows the hypocenter location resulting from the 3-D inversion (SIMUL-2000) and the relative relocation (hypoDD). In general, the use of the relative relocation does not significantly change the hypocenter location. However, it significantly sharpens the lineation of the earthquakes along the main SFS and along the secondary fault

system around the Tarutung Basin.

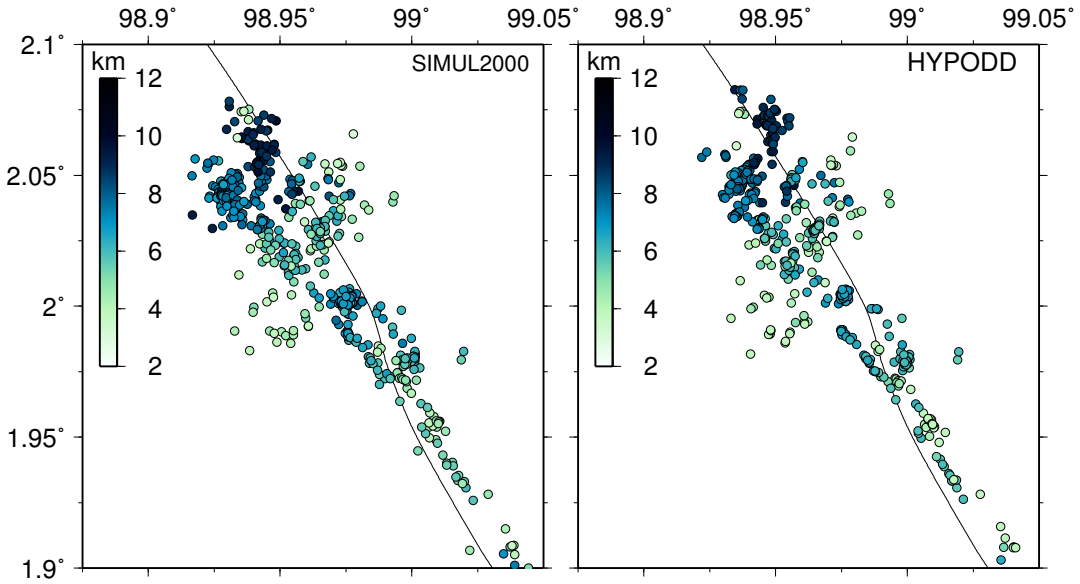

Figure 6.4: The comparison between the hypocenters obtained from SIMUL2000 (LEFT) and hypoDD relocation (RIGHT). Color indicates earthquake depths.

Given the ray azimuth and takeoff angles derived from a 3D inversion, each focal mechanism is calculated for different trials indicated by black thin lines on each fault-plane solution in Fig. 6.5a. A grid search procedure is performed to find fault-plane solutions which explain the data. Following Hardebeck and Shearer (2002) we perform 50 trials with a 50 interval. The preferred solution represents the most probable mechanism of all acceptable mechanisms. Fig. 6.5a shows some examples of the focal mechanisms with different quality defined in Table 6.2. After removing outliers indicated by black dots on the white areas and white dots on the black areas in Fig. 6.5a the average of acceptable solutions is chosen as the preferred mechanism. In the procedure of the focal mechanism calculation, the solution with the largest difference from the average is excluded and the new average is calculated until all remaining mechanisms are within 30^0 of the average.

The mechanism quality criteria shown in Table 2 are similar to the criteria used by Hardebeck and Shearer (2002). We assume that the focal mechanisms with quality B (31 events), C (23 events) and D (376 events) are acceptable. From 725 events, only 430 events have acceptable focal mechanisms which are located at latitude larger than 1.850. Because of poor station coverage, earthquakes located in Sarulla (sourthern part of Tarutung) have low quality focal mechanisms (E and F criteria). The majority of the earthquakes along the main fault is right lateral strike-slip associated with the

NW-SE striking main fault (Fig. 6.4 and Fig. 6.5b). Along the secondary fault system within the Tarutung Basin the earthquakes are more complex containing NW-SE strike-slip, NS strike-slip and (oblique) normal mechanisms (Fig. 6.6).

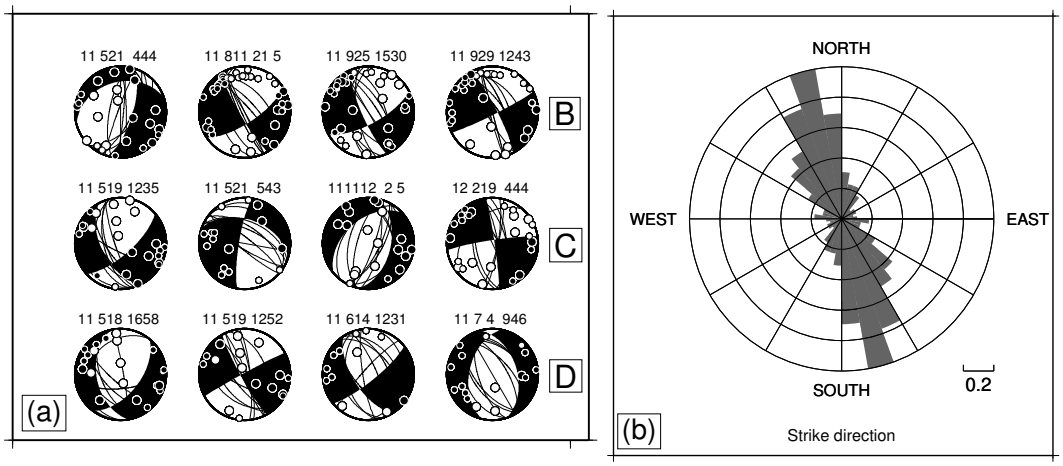

Figure 6.5: The results of focal mechanism analysis. (a) Examples of preferred solutions of focal mechanisms characterized as B, C, and D defined in Table 2. White and black dots represent down and up polarities, respectively. The thin lines show 10 different possible solutions with higher RMS values. (b) The total strike direction of all focal mechanisms.

6.4 Discussion

6.4.1 Fault system

The Seismicity along Sumatran Fault and the basin margin

We focus the analysis of the fault structure on the area surrounding the Tarutung basin. Since the stations along the Sarulla Basin (the southern part of the network) were only located along the fault, we could not derive good quality focal mechanisms for the events in the south. As shown in Fig. 6.6, in the south of Tarutung (outside of the basin), the earthquakes are distributed along the main SFS. This earthquake cluster is mostly strike-slip associated with the strike-slip fault of the main SFS. The seismicity distribution also confirms that the Tarutung Basin is a pull-apart basin. The two active flanks (the eastern and the western) of the SFS are delineated by the seismicity. The events along these two flanks are mostly strike-slip similar to the SFS. The western flank of the fault seems to be more active than the eastern flank.

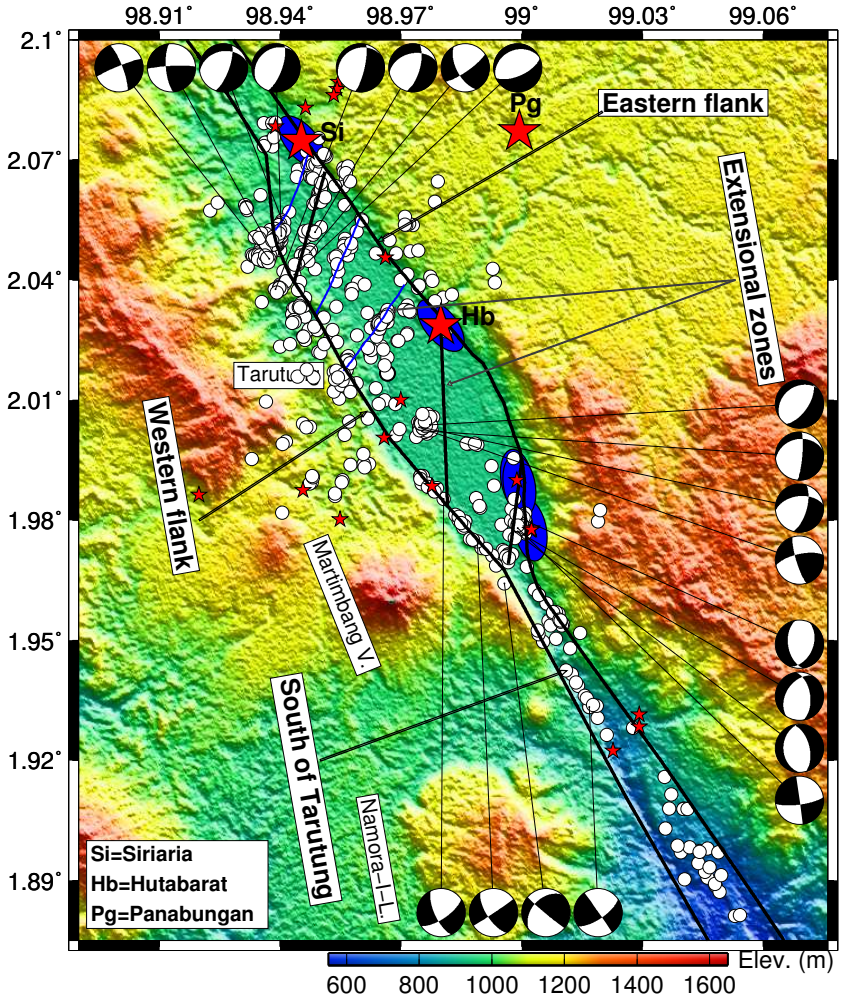

Figure 6.6: The seismicity pattern and selected focal mechanisms plotted onto the topographic map. Topography is ASTER G-DEM (30 m resolution). The basin geometry and the extensional zones are represented by the black solid lines (after Nukman and Moeck, 2013). The blue lines indicate the extensional zones derived from the seismicity. The red stars, the white circles, and the blue ellipses respectively represent the hot springs, the seismicity, and the travertines.

The earthquake distribution in and around the Tarutung Basin reflects the geometry of the basin. The boundary line of the basin in Fig. 6.6 is obtained from Nukman and Moeck (2013). A large number of earthquakes occurred at the northwestern and southeastern corners of the basin. The normal fault system at the southeastern corner of the basin (Fig. 6.6 in Nukman and Moeck (2013)) is also reflected by the seismicity pattern. The high seismicity in the corner of the basin is associated with the fault bend. A pull-apart basin along a strike-slip fault normally starts to develop at the fault bends (e.g. Woodcock and Fischer, 1986). The large number of the earthquakes at the fault bents (at both corners) indicates that the basin is very active and the basin is still developing.

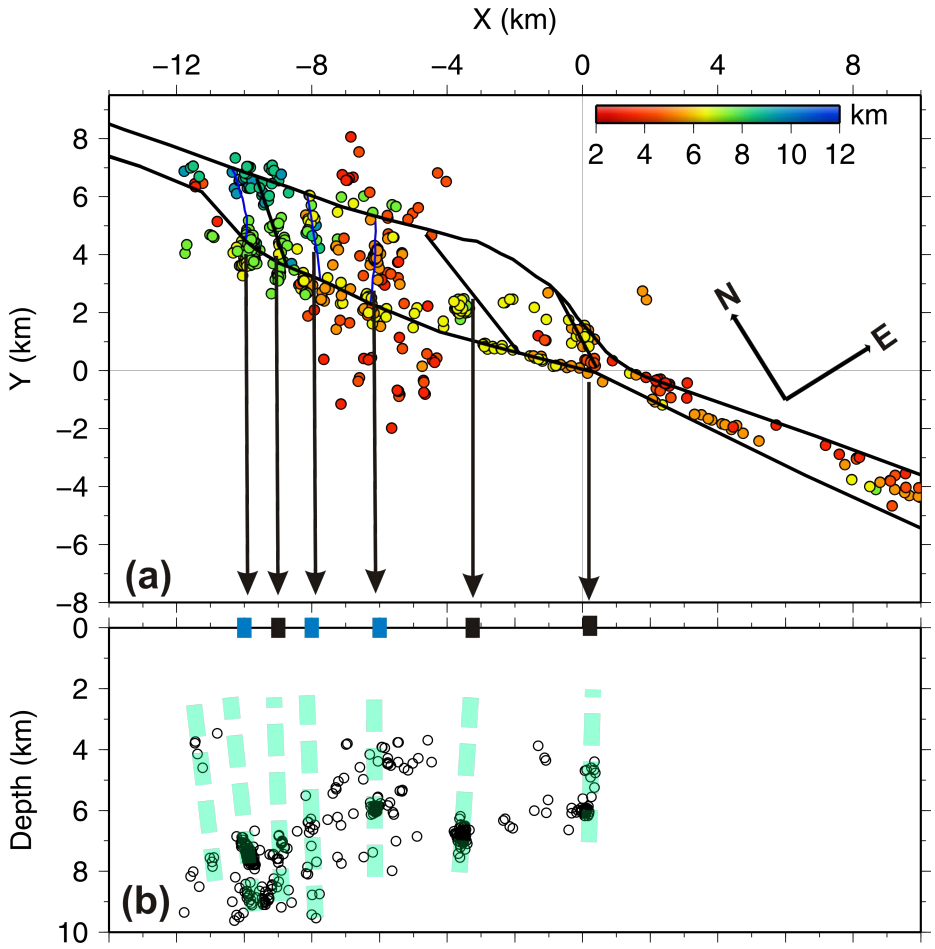

Figure 6.7: (a) The rotated map view of the seismicity. (b) The seismicity at all depth projected to X coordinate. The black and blue marks on the surface in Fig. b represent the locations of extensional zone derived from the geological observation and the seismicity, respectively. The seismicity along the main fault is exluded in Fig. b. The thick transparant light-blue lines indicate the vertical fault system deduced from the seismicity pattern.

Extensional zones

In addition to the boundary faults, we notice large number of earthquakes related to a set of secondary faults. The secondary fault system associated with the extensional zones from Nukman and Moeck (2013) is also indicated by the almost north-south direction strike-slip and (oblique) normal fault earthquakes (Fig. 6.6). Some extensional zones within the basin can be observed in the topography. The extensional zones derived from the lineation of seismicity are consistent with those obtained from the geological observation. The black and blue nearly N-S striking extensional zones (Fig. 6.6) represent the fault zones derived from geological observation and seismicity lineation, respectively. The N-S and NNE-SSW strike of fault plane solutions along

the extensional faults correlates with the maximum principal stress direction. The almost N-S compressional stress would be induced by the nearly N-S Indo-Australian plate motion. The extensional faults form an en-echelon pattern indicated by the NW-SE dextral strike-slip earthquake along the northern extensional zones.

The conceptual model

In order to study the fault system at depth we rotate the seismicity, the faults, and the basin geometry so that the secondary fault system (the extensional zones) is perpendicular to the X-axis as shown in Fig. 6.7a. All earthquakes are then projected onto the Y axis showing the distribution of the earthquakes at depth (Fig. 6.7b). We deduce the vertical fault system from the depth to the surface based on the seismicity pattern. The derived fault system is indicated by the thick transparent light blue lines overlaying the seismicity. In Fig. 6.7b we exclude the seismicity along the main SFS and along the basin margins in order to analyze the vertical pattern of the seismicity within the Tarutung Basin. The earthquakes did not occur at shallow depth, most likely because the basin is filled with unconsolidated material until a depth of 2.5 km, as indicated in the Vp images (Muksin et al., 2013a).

The secondary fault system appears to be very steep as also found by the geological studies (Nukman and Moeck, 2013). The vertical seismicity pattern also correlates with the location of the extensional zones at the surface as observed by the geological mapping. The black squares at 0 km in Fig. 6.7b indicate the location of the fault zones observed at the surface. We determine the location of the other extensional zones at the surface (blue squares at 0 km in Fig. 6.7b) according to the pattern of the seismicity.

From the seismicity pattern and the focal mechanisms we propose a simplified conceptual model of the fault system in the Tarutung Basin as shown in Fig. 6.8. The layers in Fig. 6.8 are taken from from seismic velocity derived from the Vp and Vp/Vs tomography study (Muksin et al., 2013a – Fig. 15). Different layers represented by the variation of seismic velocities are caused mostly by the changes in rock types. The map view of the seismicity shows imbricate fault arrays in strike-slip systems splaying on the Tarutung Pull-Apart Basin. This indicates the presence of almost symmetrically extensional duplexes occurring at a releasing bend between 1.96 N and 2.07 N (Fig. 6.6). Normal or oblique normal faults should accompany the extensional duplexes to accommodate the extension caused by the NW-SE dextral strike-slip main SFS. The conceptual model (Fig. 6.8) shows dip-slip faults resulting in the extensional duplexes in the cross-section view. In a fault-perpendicular cross-section, this

structure would be recognized as a negative flower structure. Nukman and Moeck (2013) suggested that several parallel WNW–ESE striking normal faults in the east of the Tarutung Basin indicate the presence of negative flower structure (see Fig. 3 in Nukman and Moeck, 2013). Following Nukman and Moeck (2013), the strike direction of these parallel normal faults has rotated clockwise to WNW-ESE.

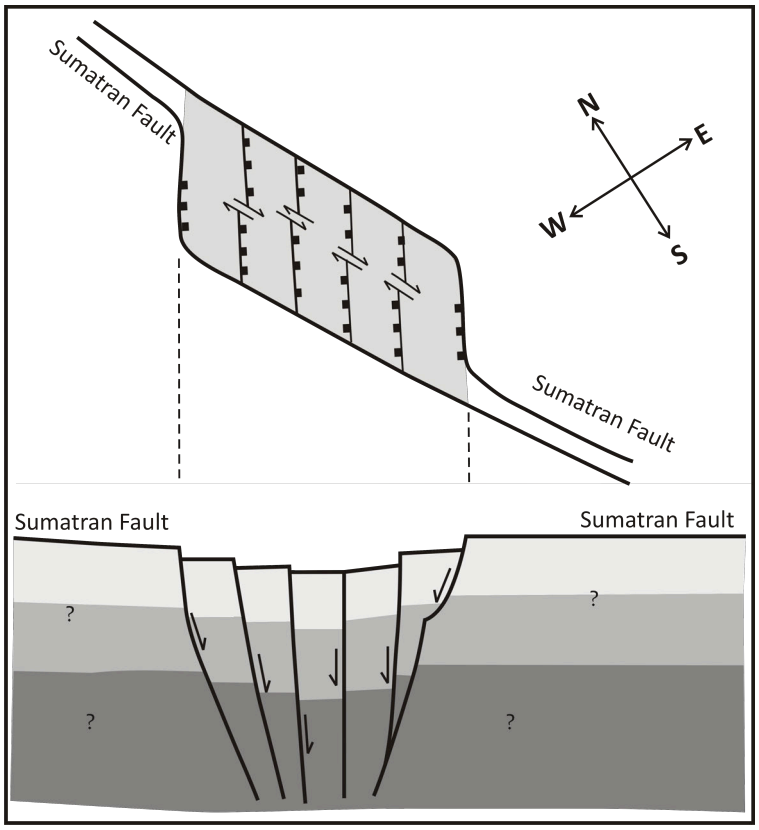

Figure 6.8: Simplified conceptual model of the fault system in the Tarutung Basin. The layers are adopted from Muksin et al. (2013a).

Although the extensional duplex system is not observed clearly on the surface it is revealed by the accurate hypocenter locations in the small Tarutung Basin. Extensional duplex faults are often observed at a bend or a step over offset of a strike-slip fault (Woodcock and Fischer, 1986). A slightly different type of an extensional duplex system is observed in the vicinity of the bifurcation just south of the Tarutung district (Weller et al., 2012). Other duplex systems might also be found along the SFS since several fault bends and step over offsets are visually observed (e.g. Singkarak and Suoh pull-apart basins). Similar extensional duplex systems are found in other areas for example along the Liquiñe-Ofqui Fault Zone, southern Chile (Cembrano

et al., 1996) and York Cliffs strike-slip fault system, southern coastal Maine, USA (Swanson, 1990).

6.4.2 Fault-controlled geothermal system

It has been proposed that the geothermal resource in the Tarutung area is controlled by the fault system (Muksin et al., 2013a; 2013b; Nukman and Moeck, 2013). This interpretation is based on the high Vp/Vs structure and the high seismic attenuation anomalies (Muksin et al., 2013a; 2013b). The ratio of helium isotope as measured by Halldórsson et al. (2013) shows a low value (i.e R/Ra 1.6-1.7). This low R/Ra indicates that a heat source in the crust is more dominant than one from the mantle. Niasari et al. (2012) suggested that the geothermal resource in Tarutung is a result of deep fluid circulation according to the interpretation of the magnetotelluric data.

At the eastern junctions of the extensional zones and the eastern margin of the basin we found travertine (indicated by blue ellipses in Fig. 6.6). Nukman and Moeck (2013) and Hochstein and Sudarman (1993) suggested that these travertine dykes explain the characteristics of the geothermal reservoir. The presence of the travertine dykes in the eastern margin indicates that high hydrogen-carbonate rich hot fluid is fed from depth (6-10 km) to the east (Nukman and Moeck, 2013). At depth, the fluid uses the faults as the path ways while at shallow depth the fluid is transported along a more permeable zone in the east (Hochstein and Sudarman, 1993). At the surface, Nukman and Moeck (2013) observed large number of west dipping normal faults (e.g. around Panabungan) and fractures in the east that ease the fluid transport.

6.5 Conclusion

We derived the fault structure at depth from the seismicity relocation and focal mechanism analysis and supported by structural geological evidence. The application of the relative relocation scheme sharpens the seismicity distribution reflecting the fault lineation more clearly although the cluster centroids do not change significantly. The seismicity distribution images well the geometry of the Tarutung Pull-Apart Basin at depth. Along the western and eastern margin as well as along the fault south of the Tarutung Basin the earthquakes are mostly strike-slip associated with the dextral strike-slip SFS.

The delineation of the events shows the presence of the strike-slip extensional duplex at the releasing bend within the Tarutung Pull-Apart Basin which is not clearly ob-

served at the surface. The extensional duplex system forms a negative flower structure of the Tarutung Basin. Two duplex faults derived from the seismicity distribution coincide with extensional zones found by geological observation. The array of parallel extensional zones accommodates the almost N-S maximum stress associated with the direction of the Indo-Australian and Sunda plates convergence. The geothermal system in the Tarutung area seems to be a fault-controlled system which uses the fault zones (at depth) as the fluid path ways. We suggest that the hot fluid is transported to the more dilatational, more fractured and more permeable region in the east.

Acknowledgment

This work is part of the project "Sustainability concepts for exploitation of geothermal reservoirs in Indonesia-capacity building and methodologies for site deployment" funded by the German Federal Ministry of Education and Research (BMBF) under grant 03G0753A. At the Indonesian side, we wish to thank the Center for Geological Resources (the Indonesian governmental agency responsible for geothermal exploration) and the local government of North Tapanuli (Tarutung), North Sumatra for their support in the deployment of the instruments. The instruments for the experiment were provided by the Geophysical Instrument Pool Potsdam (GIPP). Particular thanks go also all colleagues who participated in the field work.

Chapter 7
Summary and Conclusions

7.1 Quality of the models

The work was started with the deployment of the seismic network for 10 months in the Tarutung region in May 2011. The seismic arrivals were identified by an optimized automatic seismic arrival detection and the earthquakes were localized by using the HYPO71 algorithm. In order to increase the quality of the arrivals, the automatic picks were revised manually and the earthquakes were relocated. The network recorded 2586 local earthquakes but only 809 events were located within the network (events with azimuthal gap angle less than 180^0) and used for traveltime tomography. Among those 809 events, only 229 events with very good quality waveforms were used for attenuation tomography. Having high accuracy phase arrival picks, I produced a 1D velocity model by using a simultaneous inversion for velocity modelling and hypocenter determination (VELEST software). The detailed procedure is described in Chapter 4 (in Muksin et al., 2013a). The quality of the 1D inversion result is assessed from the decreases of the data variance and the RMS residuals. This 1D velocity model was then applied as the initial velocity model in the 3D inversion (SIMUL2000) for 3D velocity and seismic attenuation tomography.

The quality of the results of the 3D inversion for the velocity models (Vp and Vp/Vs) as well as the seismic attenuation was investigated by using several approaches: the model resolution matrix, the spread function and the synthetic test. A node with a small spread function value and localized contour lines of the resolution matrix is supposed to be well-resolved. Synthetic models including checkerboard and characteristic feature (designed based on the observed geological setting) were resolved well in the area with sufficient ray-paths. The quality assessments are discussed in Section 4.5 (Muksin et al., 2013a) for the Vp and Vp/Vs models and in Section 5.5 (Muksin et al., 2013b) for the attenuation tomography. From the quality investigation I conclude that the 3D velocity and the seismic attenuation models are resolved 12 km to the west and to the east of the Sumatran Fault. However, along the Sarulla area, the models were only resolved along the vicinity of the Sarulla basin.

7.2 Velocity, seismic attenuation and other geophysical signatures

Geophysical anomalies are related to lithology and physical properties of rock or fluid as described in Chapter 4 and 5 (Muksin et al. 2013a; 2013b). The distributions of three geophysical properties have been determined by this seismology research, namely Vp, Vp/Vs (from traveltime tomography) and seismic attenuation (Q_p) structure (from attenuation tomography). Subsequent magnetotelluric measurements have provided electrical resistivity/conductivity signatures of the region (Niasari et al., 2012) that is used to constrain the interpretation. Previous geophysical studies by the Centre for Geological Resource of Indonesia provided the resistivity (Mustang et al., 2005), density (Djudjun, 2005) and magnetic anomalies (Situmorang, 2005) of the area.

The anomalies of the Vp, Vp/Vs, the seismic attenuation and other geophysical properties are summarized in Table 7.1 and compiled in Fig. 7.1. Based on the vertical Vp model (see Fig. 4.15), the seismic structure of the region is divided into three main layers. In general, there are five different zones classified from joint interpretation of geophysical anomalies.

Zone 1 is the Tarutung pull-apart basin which is the northern green area in Fig. 7.1. This region is characterized by low Vp, high seismic attenuation (low Q_p) and high electrical conductivity (Niasari et al., 2012) associated with unconsolidated material within the basin. The thicknesses of the low Vp and high conductivity anomalies are around 2.0 km representing the depth of the Tarutung basin. At depths of around 3 - 10 km the Tarutung basin is characterized by high Vp/Vs and low Q_p (high attenuation) anomalies. These anomalies are interpreted as the source of the hot fluid.

Zone 2 is the northeastern region of the Tarutung basin where the three big hot springs, Sipoholon, Hutabarat, and Panabungan, are located (the red area in Fig. 7.1). This zone is characterized by low Vp, high Vp/Vs, high attenuation, and high conductivity. At shallow depth (above ~3 km), a high attenuation anomaly covers all three big hot springs while the low Vp, high Vp/Vs and high conductivity anomalies are located slightly further east around the Panabungan hot spring. The high Vp/Vs, high conductivity and high attenuation anomalies most likely reflect the much higher flow rate of the Panabungan hot spring compared to that of the Sipoholon hot spring. Zone 2 is connected to Zone 1 at greater depth.

Zone 3 is a dry area (based on observation) located in the west of the Tarutung basin (the blue area in Fig. 7.1). This zone is mostly occupied by granite (Nukman and Moeck, 2013). This granitic area is characterized by a prominent low Vp/Vs anomaly and low conductivity. Granite normally consists of quartz, mica, and feldspar. The low Vp/Vs might be caused by a large amount of quartz in the rock. Quartz has the lowest Vp/Vs or Poisson's ratios. For the pressure range of 200 MPa - 100 MPa, quartz has Vp/Vs values of 1.478 - 1.502 and Poisson's ratios of 0.027 - 0.024 (Christensen, 1996). The low Vp/Vs anomaly covers a large area from the northwest to southwest of the Tarutung basin including the Martimbang volcano.

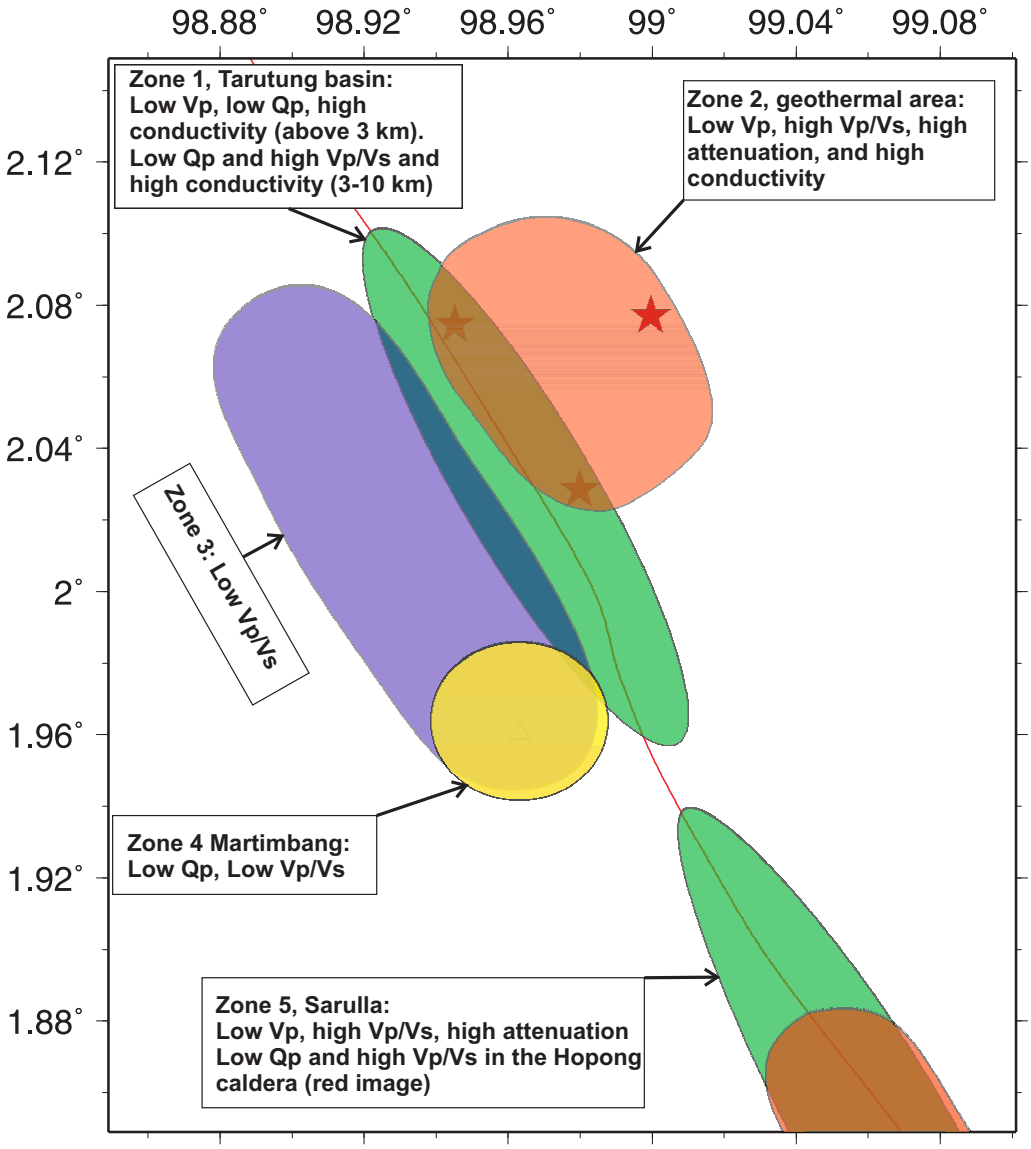

Figure 7.1: The summary of the geophysical signatures observed in the Tarutung area.

Table 7.1: The summary of geophysical anomalies of the Tarutung and Sarulla region

Location	**Geophysical properties**	**Interpretation**
Zone 1: Along the Tarutung basin	At depth around 2 km: low Vp, low Q_p (high attenuation), high conductivity (MT result).	Unconsolidated material within the basin
	At depth greater than 3 km: high Vp/Vs, low Q_p, and high conductivity (MT result).	Hot fluid flow
Zone 2: Northeastern Tarutung geothermal area	At depth above 2 km: Low Vp and high Vp/Vs around Panabungan	High fluid content
	At depth above 2 km: High conductivity (MT results) around Panabungan	Fluid circulation
	At depth above 2 km: Low Q_p around Sipoholon and Panabungan.	High fluid content in Panabungan and slightly higher temperature and less fluid in Sipoholon
	At depth of 700 m: East of Sipoholon: low resistivity. At depth of 1700 m: West of Sipoholon (eastern margin of the Tarutung basin): low resistivity.	Location of reservoir is shallower in the East than that in the West
Zone 3: West of the Tarutung basin	Low Vp/Vs Low conductivity	Compact and rigid granitic rock and dry region
Zone 4: Beneath Martimbang volcano	Normal Vp, low Q_p, and high conductivity	Sleeping magma body or dry hot rock
Zone 5: Sarulla basin	At depth above 2 km: low Vp, high Vp/Vs, and low Q_p	Weak Sarulla basin and geothermal resources located along the basin
	At depth below 2 km: high Vp/Vs and low Q_p	Sarulla basin and geothermal resources located along the basin
	Around Hopong caldera: prominent high Vp/Vs and low Q_p	Magma chamber of Hopong caldera and geothermal resource.

Zone 4 is the area of the Martimbang volcano (the yellow area in Fig. 7.1) which

is located in the southwest of the Tarutung basin with the age around 1.8 M year. The low Q_p anomaly is found below the volcano at depth of 0-8 km. However, normal Vp and low Vp/Vs values are observed in this area. Nukman and Moeck (personal communication, 24 January 2014) suggested that the volcano is inactive. It is proposed that there is no fluid intrusion below the volcano as there are no hot springs or fumaroles around the volcano. The high attenuation (low Q_p) is interpreted to be indicative of sleeping magma or dry hot rock (without or with little amount of partial melting) below the volcano. Another possibility is that hot fluid could not rise up since granite (indicated by low Vp/Vs) underlies the magma. The low Q_p (high attenuation) anomaly could also be associated with old hydrothermal alteration.

Zone 5 is the Sarulla area (the southern green area in Fig. 7.1) which consists of the Sarulla basin, Hopong caldera, geothermal resources along the basin and the Namora Langit dome field in the northwest of the Sarulla basin. However, since the focus of the study was the Tarutung region and the road was inaccessible in the south, the stations in Sarulla were deployed along the basin (along the Sumatran fault). Therefore the resolution of the tomography results in this area is best only along the Sarulla basin. This zone is characterized by low Vp, high Vp/Vs and low Q_p anomalies. The low Vp anomaly images the unconsolidated material within the basin to a depth of around 2 km indicating the thickness of the basin. The high Vp/Vs and high attenuation features are observed at greater depth indicating a weak zone associated with volcanic activity and high temperature geothermal resources. The most prominent block of high Vp/Vs and high attenuation signatures is located in the vicinity of the Hopong caldera. These high Vp/Vs and high attenuation anomalies indicate high temperature magma below the caldera.

7.3 Tectonic setting and geothermal system of Tarutung

7.3.1 Fault system

The fault system in the region was derived from the hypocentres and the focal mechanisms of the earthquakes and also supported by the geological observation. The procedure of the fault deduction from local earthquake data as well as its results is described in detail in Chapter 6. The delineation of the earthquakes correlates with the diamond shape Tarutung basin margin (see Fig. 6.6 for more detail). The seismicity distribution confirms that the Tarutung basin is a pull-apart basin. The

eastern and the western flanks of the faults correlate with the seismicity distribution. In the south of the Tarutung basin (outside the basin) the seismicity is confined to the main Sumatran fault. The focal mechanisms of the earthquakes in the south are mostly strike-slip which is consistent with the characteristics of the main Sumatran fault. Within the Tarutung basin several extensional zones are determined by geological observation and also deduced from the local earthquake data. The extensional zones derived from the seismicity are consistent with the field observation. These parallel extensional zones form the extensional duplex in the Tarutung basin. From vertical view of the seismicity (Fig. 6.7) I suggest that the Tarutung basin consists of a negative flower structure.

The fault setting in the Sarulla region could not be deduced directly from the seismicity since the station coverage in the southernmost region was poor. The fault setting in the Sarulla region was described in detail by Hickman et al. (2004). Most earthquakes along the Sarulla basin have an azimuthal gap angle larger than 180^0. However, from the seismicity location I could observe that the earthquakes tend to be located in the west of the Sarulla graben (see Fig. 2.3). The earthquakes located in the western margin of the graben might be related to the secondary fault system as discussed in Hickman et al. (2004). The Sarulla graben is considered to be weaker than the Tarutung basin since several magmatic activities are located along the basin such as the Hopong caldera, the Namora Langit dome field, and the geothermal resources (see Fig. 1.4). The Sarulla basin is characterized by several normal faults parallel to the main Sumatran fault. This graben is not a pull-apart basin since there is no step over that forms two separate flanks (Hickman et al., 2004).

7.3.2 Geothermal system

Previous geothermal exploration studies speculated that the heat source of the geothermal system around the Tarutung basin is related to the magma chamber beneath the Martimbang volcano. However, those geophysical studies focussed on the area of the Tarutung basin. With this limited area of geophysical experiments, it is difficult to deduce the relation between the volcano and the geothermal system. The only measurement that covered the volcano area was the gravity measurement (Djudjun, 2005). The gravity anomaly does not clearly show the correlation between the magma of the volcano and the geothermal system around Tarutung. The previous geophysical results, however, could be used to constrain the interpretation.

Passive seismic and magnetotelluric studies suggest that there is no strong correlation between the geothermal system around the Tarutung basin and the magmatic system

beneath the Martimbang volcano. The Vp/Vs values, the seismic attenuation, the magnetotelluric signatures as well as the structural geology analysis suggest that the volcano consists of sleeping magma body or dry hot rock with little amount of partial melting as described in Section 7.2. The results of the new observation conclude that the geothermal resource around Tarutung is mainly a fault-controlled system with deep circulation of water. Meteoric water flows down and heats up and then flows back up to the surface using the fault zones as path-ways.

The Vp/Vs, the seismic attenuation and also the magnetotelluric anomalies suggest that the hot fluid originates from depths below the Sumatran fault and is transported to the northeast (Muksin et al. 2013a; 2013b). The results of the new geophysical investigations suggest that the three big geothermal manifestations (Sipoholon, Hutabarat, and Panabungan) are fed by the same source of hot fuid below the basin. In contrast to two other geothermal manifestations (Sipoholon and Hutabarat), the Panabungan area is characterized by the high Vp/Vs and high conductivity anomalies. These anomalies are associated with higher fluid flow rate ($>$ 55 liter/second) but slightly lower temperature (~58 ^0C). On the other hand, the Sipoholon (Si) geothermal area is characterized by high seismic attenuation. This correlates with higher fluid temperature (~65 ^0C) and less fluid flow rate (~25 liter/second) (compared to those in Panabungan). It seems that the geothermal resource in Panabungan consists of more meteoric water than that in Sipoholon area. The Sipoholon geothermal resource is located closer to the hot fluid source (the Tarutung basin) so that it has higher temperature. From geoelectrical measurements, the depth of the reservoir around the Sipoholon geothermal area is shallower in the east (700 m) and becomes deeper (1,400 m) further west. This coincides with the interpretation from the Vp/Vs and attenuation tomography. The hot fluid (interpreted as reservoir by Hasan et al., 2005) is found shallower in the east and deeper in west (closer to the basin) since the hot fluid at depth from below the fault flows to the east.

Several scenarios are considered to be the reasons for the northeastern hot fluid flow in the Tarutung region. Granitic rocks are found in the western part of the basin (Nukman and Moeck, 2013) and also indicated by low Vp/Vs and low electrical conductivity (Niasari et al., 2012). In contrast, a large amount of volcanic andesitic rock is observed in the east (Nukman and Moeck, 2013). The granitic rock could continue underneath the basin. This compact and rigid granitic rock prevents the hot fluid from below the fault to flow directly to the basin or to the west of the Tarutung basin.

The andesitic rock in the east of the basin on the other hand has higher porosity and is weaker than granite. Therefore, more cracks and fractures occur in the eastern

region of the Tarutung basin occupied by andesitic rock. Consequently, the hot fluid originated from below the Sumatran fault is easier to transport to the northeast. The hot fluid path-way is mimicked by the northeast direction of high Vp/Vs (Muksin et al., 2013a or Chapter 4), the high seismic attenuation (Muksin et al., 2013b or Chapter 5), and low resistivity determined by the magnetotelluric study (Niasari et al., 2012).

Furthermore, Nukman and Moeck (2013) suggested that there is a clock-wise rotation in the east of the Tarutung basin. This rotation has made the eastern part more dilatational, indicated by large amount of normal and oblique normal faults in the east. It is very likely that the hot fluids flow following the dilatational fault system. This concept has been suggested in Chapter 4 (Muksin et al., 2013a) and in Chapter 5 (Muksin et al., 2013b). I suggest that these three scenarios together contribute to the control of the hot fluid flow in the east of the Tarutung basin.

A caldera-like structure in the east of the Tarutung basin was introduced in Chapter 1 (see Fig. 1.4 in Chapter 1). Several calderas associated with the presence of basins are observed in the east of the Sumatran fault. Among them are the Toba caldera in the north of the Tarutung basin and the Hopong caldera in Sarulla. If an old caldera is present in the east of the Tarutung basin the high Vp/Vs and high attenuation could be associated with an old magma beneath the old caldera. However, there is no clear geological and geochemical evidence of the presence of a caldera found in this area (Nukman and Moeck, personal communication, January 24, 2014).

From the Vp/Vs and the attenuation tomography results I conclude that the geothermal reservoir of those three manifestations (Sipoholon, Hutabarat, and Panabungan in Fig. 5.8 Chapter 5) is located between 1 to 2 km depth in the northeast of the Tarutung basin. The reservoir is fed by hot fluids circulating to depths of around 10 km. The hot fluid uses the vertical fault line as the path-way and migrates to the more dilatational and the more permeable zone in the northeast. The Sipoholon (Si) and the Hutabarat (Ht) manifestations are classified as the upflow geothermal system since they are located just above the reservoir as indicated by the presence of travertine. Travertine in a geothermal area indicates high carbonate contents of water associated with the geothermal reservoir (Nukman and Moeck, 2013; Hochstein and Sudarman, 1993). The Panabungan (Pg) geothermal manifestation is located more to the east of the reservoir therefore has lower temperature compared to those of the Sipoholon and the Hutabarat manifestations. The boundaries of the prominent normal faults play an important role in the geothermal fluid discharge in the area as also suggested by Muraoka et al. (2010). The Sipoholon and the Hutabarat manifes-

tations are located at the eastern junction of the oblique normal extensional zones and at the eastern margin of the basin (Fig. 6.6, Chapter 6). The Panabungan (Pg) manifestation is also located the NW-SE normal fault (see Fig. 3 in Nukman and Moeck, 2013).

As mention above that the geothermal system in Tarutung is controlled by the fault system in the area. Several amagmatic fault-controlled geothermal system have also been found in other areas such as in the Northwestern Great Basin-Nevada USA, the South Fork Payette geothermal system Idaho USA, and the Paralana hot springs in the Northern Flinders Ranges, South Australia. The geothermal system in the Great basin Nevada is located along a right lateral strike-slip Walker lane fault striking northwest-southeast and along several northeast striking normal fault (Faulds et al., 2004). Several lineations of the hot springs in the Great basin Nevada are formed following these extensional fault zones. The geothermal system in this area is believed to be caused by deep circulation of water along the dilatational fault system (Faulds et al., 2004). In South Fork Payette Idaho USA the geothermal manifestations are located where the northwest striking normal faults terminate against the transtensional fault system (Dingee, 1987). In this region, the fault system is used as the channel for the migration of the thermal water to the surface. In the Northern Flinders Ranges, South Australia, radioactivity is suggested to be the heat source for the Paralana hot springs (Brugger et al., 2005). Meteoric water circulates at depth and is transported back to the surface through the Paralana fault.

7.4 The advantages and the drawback of passive seismic methods for application in geothermal exploration

The results of this study suggest that the passive seismic (seismology) method is a powerful tool to be used for geothermal exploration especially in seismically active geothermal areas such as Sumatra. Passive seismic methods could provide seismic structure (Vp, Vp/Vs, seismic attenuation) which is related to lithology and physical properties of rocks or fluids. Passive seismic studies could also provide information of fault structures from seismicity and focal mechanisms. From focal mechanisms, the stress field of a region can be derived which is important for drilling, resource assesment, and reservoir management. The results of a passive seismic study could be used as the basis for the exploitation monitoring. One could also extend the study area to reach deeper and a larger study area with similar cost or effort. On the other

hand, one could study a more detailed structure of an area by installing a network with closer distances of stations.

Very often active faults are found around magmatic geothermal resources. For example, the seismically active Lembang fault is located around the magmatic geothermal resources in Lembang West Java, Indonesia. Several other geothermal fields in West Java, Indonesia such as Wayang Windu, Kamojang, and Papandayan are also accompanied by active fault zones (Jousset et al., 2013). In Central-Southern Chile, the volcanic-geothermal activities are also controlled by the seismically active Liquiñe-Ofqui Fault Zone (Lahsen et al., 2005). Therefore, passive seismic methods could also be used for geothermal exploration of magmatic geothermal systems. The techniques of seismic tomography have been continuously developing. In case of geothermal fields are located in a non-seismically active region one could use ambient noise tomography to study the seismic structure of a region (e.g. Bensen et al., 2009).

One of the disadvantages of passive seismic methods is that longer recording time is needed compared to other methods such as magnetotelluric and geoelectric. A sufficient number of seismic stations has to be deployed at the same time in order to achieve reliable results. For comparison, magnetotelluric experiment (normally used for geothermal exploration) can be conducted with limited number of instruments. The MT instruments can be moved from one to the next measurement area. Another limitation of passive seismic method is that it can only be used in a region with seismicity which can be partly overcomed by ambient noise tomography technique.

7.5 Outlook

The research will be continued by using other methods. With sufficient fault plane solutions, the method of damped stress inversion of Hardebeck and Michael (2006) will be applied. This technique has been successfully used to understand the stress tensor changes related to fluid injection at the Geysers geothermal field (Martínez-Garzón et al., 2013). Ambient noise tomography will be conducted to complement the shear velocity structure. Ambient noise tomography has been used to study shear velocity in a geothermally active region (e.g. Behr et al., 2010). With Vp, Vp/Vs, seismic attenuation and shear velocity structure a joint analysis will be performed by using a pattern recognition technique (e.g. Bauer et al., 2003; Bauer et al., 2008). Joint analysis will include the magnetotelluric results of Niasari et al. (2012).

Bibliography

Aki, K., 1967. Scaling law of seismic spectrum. Journal of Geophysical Research 72 (4), 1217–1231.

Aki, K., Chouet, B., 1975. Origin of coda waves: source, attenuation, and scattering effects. Journal of Geophysical Research 80 (23), 3322–3342.

Aki, K., Richards, P., 1980. Quantitative seismology: Theory and methods.

Allen, R. V., 1978. Automatic earthquake recognition and timing from single traces. Bulletin of the Seismological Society of America 68 (5), 1521–1532.

Anderson, D. L., Given, J. W., 1982. Absorption band Q model for the Earth. Journal of Geophysical Research 87 (B5), 3893–3904.

Ardiwinata, N., Setiawan, Asngari, Supardjo, E., Kurniawan, S., 2005. Penyelidikan geokimia panas bumi daerah Sipoholon Kabupaten Tapanuli Utara-Sumatera Utara. In: Pemaparan Hasil Kegiatan Lapangan Subdit Panas Bumi 2005.

Artemieva, I. M., Billien, M., Lévêque, J.-J., Mooney, W. D., 2004. Shear wave velocity, seismic attenuation, and thermal structure of the continental upper mantle. Geophysical Journal International 157 (2), 607–628.

Atkinson, G. M., 2004. Empirical attenuation of ground-motion spectral amplitudes in southeastern Canada and the northeastern United States. Bulletin of the Seismological Society of America 94 (3), 1079–1095.

Badan Meteorologi Klimatologi dan Geofisika, 2012. http://bmkg.go.id. Accessed: 2012-02-26.

Barber, A. J., Crow, M. J., Milsom, J. S., 2005. Sumatra: geology, resources and tectonic evolution. No. 31. Geological Society.

Bauer, K., Muñoz, G., Moeck, I., 2012. Pattern recognition and lithological interpretation of collocated seismic and magnetotelluric models using self-organizing maps. Geophysical Journal International 189 (2), 984–998.

Bauer, K., Pratt, R., Haberland, C., Weber, M., 2008. Neural network analysis of crosshole tomographic images: The seismic signature of gas hydrate bearing sediments in the Mackenzie Delta (NW Canada). Geophysical Research Letters 35 (19).

Bauer, K., Schulze, A., Ryberg, T., Sobolev, S., Weber, M., 2003. Classification of lithology from seismic tomography: A case study from the Messum igneous complex, Namibia. Journal of geophysical research 108 (B3), 2152.

Beck, M. E., 1983. On the mechanism of tectonic transport in zones of oblique subduction. Tectonophysics 93, 1 – 11.

Behr, Y., Townend, J., Bannister, S., Savage, M. K., 2010. Shear velocity structure of the Northland Peninsula, New Zealand, inferred from ambient noise correlations. Journal of Geophysical Research: Solid Earth 115 (B5).

Bellier, O., Sébrier, M., 1994. Relationship between tectonism and volcanism along the Great Sumatran Fault Zone deduced by spot image analyses. Tectonophysics 233, 215–231.

Bellier, O., Sébrier, M., 1995. Is the slip rate variation on the Great Sumatran Fault accommodated by fore-arc stretching? Geophysical Research Letters 22 (15), 1969–1972.

Bensen, G. D., Ritzwoller, M. H., Yang, Y., 2009. A 3-d shear velocity model of the crust and uppermost mantle beneath the United States from ambient seismic noise. Geophysical Journal International 177 (3), 1177–1196.

Boatwright, J., Fletcher, J. B., Fumal, T. E., 1991. A general inversion scheme for source, site, and propagation characteristics using multiply recorded sets of moderate-sized earthquakes. Bulletin of the Seismological Society of America 81 (5), 1754–1782.

Bohm, M., Haberland, C., Asch, G., 2013. Imaging fluid related subduction processes beneath Central Java (indonesia) using seismic attenuation tomography. Tectonophysics.

Brugger, J., Long, N., McPhail, D., Plimer, I., 2005. An active amagmatic hydrothermal system: the Paralana hot springs, Northern Flinders Ranges, South Australia. Chemical Geology 222 (1), 35–64.

Brune, J. N., 1970. Tectonic stress and the spectra of seismic shear waves from earthquakes. Journal of geophysical research 75 (26), 4997–5009.

Brune, J. N., 1971. Correction. Journal of Geophysical Research 76, 5002.

Cembrano, J., Hervé, F., Lavenu, A., 1996. The Liquiñe Ofqui fault zone: a long-lived intra-arc fault system in southern Chile. Tectonophysics 259 (1), 55–66.

Chatterjee, S., Pitt, A., Iyer, H., 1985. Vp/Vs ratios in the Yellowstone National Park region, Wyoming. Journal of volcanology and geothermal research 26 (3), 213–230.

Christensen, N. I., 1996. Poisson's ratio and crustal seismology. Journal of Geophysical Research: Solid Earth (1978–2012) 101 (B2), 3139–3156.

Chung, J.-K., Chen, Y.-L., Shin, T.-C., 2009. Spatial distribution of coda Q estimated from local earthquakes in Taiwan area. Earth Planets and Space (EPS) 61 (9), 1077.

De Lorenzo, S., Gasparini, P., Mongelli, F., Zollo, A., 2001. Thermal state of the Campi Flegrei caldera inferred from seismic attenuation tomography. Journal of geodynamics 32 (4), 467–486.

De Siena, L., Del Pezzo, E., Bianco, F., 2010. Seismic attenuation imaging of Campi Flegrei: Evidence of gas reservoirs, hydrothermal basins, and feeding systems. Journal of Geophysical Research: Solid Earth 115 (B9), 1–18.

Dingee, B. E., 1987. Geology, hydrology and geochemistry of the geothermal area East of Lowman, Idaho. Master's thesis, Department of Geology, Washington State University.

Djudjun, A., 2005. Penyelidikan gaya berat daerah panas bumi Ria-Ria Sipoholon, Tarutung, Tapanuli Utara-Sumatra Utara. In: Pemaparan Hasil Kegiatan Lapangan Subdit Panas Bumi 2005.

Dziewonski, A. M., 1984. Mapping the lower mantle: Determination of lateral heterogeneity in P velocity up to degree and order 6. Journal of Geophysical Research: Solid Earth (1978–2012) 89 (B7), 5929–5952.

Dziewonski, A. M., Anderson, D. L., 1981. Preliminary reference earth model. Physics of the Earth and Planetary Interiors 25 (4), 297–356.

Eberhart-Phillips, D., 1986. Three-dimensional velocity structure in northern California Coast Ranges from inversion of local earthquake arrival times. Bulletin of the Seismological Society of America 76 (4), 1025–1052.

Eberhart-Phillips, D., 1990. Three-dimensional P and S velocity structure in the Coalinga region, California. Journal of Geophysical Research: Solid Earth (1978–2012) 95 (B10), 15343–15363.

Eberhart-Phillips, D., 1993. Local earthquake tomography: earthquake source regions. Seismic Tomography: Theory and Practice, 613–643.

Eberhart-Phillips, D., Chadwick, M., 2002. Three-dimensional attenuation model of the shallow Hikurangi subduction zone in the Raukumara Peninsula, New Zealand. Journal of geophysical research 107 (B2), 2033.

Eberhart-Phillips, D., Michael, A. J., 1998. Seismotectonics of the Loma Prieta, California, region determined from three-dimensional Vp, Vp/Vs, and seismicity. Journal of Geophysical Research: Solid Earth (1978–2012) 103 (B9), 21099–21120.

Evans, J. R., Eberhart-Phillips, D., Thurber, C., 1994. User's manual for simulps12 for imaging Vp and Vp/Vs: a derivative of the" Thurber" tomographic inversion simul3 for local earthquakes and explosions. US Department of the Interior, US Geological Survey.

Evans, J. R., Zucca, J. J., 1988. Active high-resolution seismic tomography of compressional wave velocity and attenuation structure at Medicine Lake Volcano, Northern California Cascade Range. Journal of Geophysical Research: Solid Earth (1978–2012) 93 (B12), 15016–15036.

Faul, U. H., Gerald, F., John, D., Jackson, I., 2004. Shear wave attenuation and dispersion in melt-bearing olivine polycrystals: 2. microstructural interpretation and seismological implications. Journal of Geophysical Research: Solid Earth (1978–2012) 109 (B6).

Faulds, J. E., Coolbaugh, M., Blewitt, G., Henry, C. D., 2004. Why is Nevada in hot water? Structural controls and tectonic model of geothermal systems in the northwestern Great Basin. Geothermal Resources Council Transactions 28, 649–654.

Flanagan, M. P., Wiens, D. A., 1990. Attenuation structure beneath the Lau back arc spreading center from teleseismic S phases. Geophysical Research Letters 17 (12), 2117–2120.

Foulger, G., 1982. Geothermal exploration and reservoir monitoring using earthquakes and the passive seismic method. Geothermics 11 (4), 259 – 268.

Frankel, A., Wennerberg, L., 1987. Energy-flux model of seismic coda: Separation of scattering and intrinsic attenuation. Bulletin of the Seismological Society of America 77 (4), 1223–1251.

Gasparon, M., 2005. Quaternary volcanicity. Sumatra: Geology, Resources, and Tectonic Evolution, 120–130.

Gassmann, F., 1951. Über die elastizität poröser medien: Vierteljahrss-chrift der Naturforschenden Gesellschaft in Zurich 96, 1-23. Paper translation at http://sepwww. stanford. edu/sep/berryman/PS/gassmann. pdf.

Gilbert, P., 1972. Iterative methods for the three-dimensional reconstruction of an object from projections. Journal of Theoretical Biology 36 (1), 105–117.

Gladwin, M. T., Stacey, F., 1974. Anelastic degradation of acoustic pulses in rock. Physics of the Earth and Planetary Interiors 8 (4), 332–336.

Global Centroid Moment Tensor Project, 2014. http://www.globalcmt.org. Accessed: 2014-02-26.

Gorbatov, A., Fukao, Y., Widiyantoro, S., 2001. Application of a three-dimensional ray-tracing technique to global P, PP and Pdiff traveltime tomography. Geophysical Journal International 146 (3), 583–593.

Gordon, R., Bender, R., Herman, G. T., 1970. Algebraic reconstruction techniques (ART) for three-dimensional electron microscopy and X-ray photography. Journal of theoretical Biology 29 (3), 471–481.

Gunderson, R., Dobson, P., Sharp, W., Pudjianto, R., Hasibuan, A., 1995. Geology and thermal features of the Sarulla contract area, North Sumatra, Indonesia. In: Proceedings of the World Geothermal Congress. Vol. 2. pp. 687–692.

Gunderson, R., Ganefianto, N., Riedel, K., Sirad-Azwar, L., Suleiman, S., 2000. Exploration results in the sarulla block, north sumatra, indonesia. In: Proceedings World Geothermal Congress 2000.

Gutenberg, B., Richter, C. F., 1944. Frequency of earthquakes in california. Bulletin of the Seismological Society of America 34 (4), 185–188.

Haberland, C., Rietbrock, A., 2001. Attenuation tomography in the western central Andes: A detailed insight into the structure of a magmatic arc. Journal of Geophysical Research 106 (B6), 11151–11.

Halldórsson, S. A., Hilton, D. R., Troll, V. R., Fischer, T. P., 2013. Resolving volatile sources along the western Sunda arc, Indonesia. Chemical Geology 339, 263–282.

Hanks, T. C., Wyss, M., 1972. The use of body-wave spectra in the determination of seismic-source parameters. Bulletin of the Seismological Society of America 62 (2), 561–589.

Hardebeck, J. L., Michael, A. J., 2006. Damped regional-scale stress inversions: Methodology and examples for southern California and the Coalinga aftershock sequence. Journal of Geophysical Research: Solid Earth 111 (B11).

Hardebeck, J. L., Shearer, P. M., 2002. A new method for determining first-motion focal mechanisms. Bulletin of the Seismological Society of America 92 (6), 2264–2276.

Hasan, R., Setiadarma, Risdianto, D., Supardi, K., 2005. Geologi daerah panas bumi Ria-Ria Sipoholon, Tarutung, Tapanuli Utara-Sumatra Utara. In: Pemaparan Hasil Kegiatan Lapangan Subdit Panas Bumi 2005.

Hauksson, E., Shearer, P. M., 2006. Attenuation models (QP and QS) in three dimensions of the southern California crust: Inferred fluid saturation at seismogenic depths. Journal of geophysical research 111 (B5), B05302.

Havskov, J., Ottemöller, L., 2010. Routine data processing in earthquake seismology: with sample data, exercises and software. Springer.

Hickman, R., Dobson, P., van Gerven, M., Sagala, B., Gunderson, R., 2004. Tectonic and stratigraphic evolution of the Sarulla graben geothermal area, North Sumatra, Indonesia. Journal of Asian Earth Sciences 23 (3), 435–448.

Hildyard, M. W., Nippress, S. E., Rietbrock, A., 2008. Event detection and phase picking using a time-domain estimate of predominate period Tpd. Bulletin of the Seismological Society of America 98 (6), 3025–3032.

Hildyard, M. W., Rietbrock, A., 2010. Tpd, a damped predominant period function with improvements for magnitude estimation. Bulletin of the Seismological Society of America 100 (2), 684–698.

Hochstein, M., Sudarman, S., 1993. Geothermal resources of Sumatra. Geothermics 22 (3), 181 – 200.

Holbrook, W. S., Mooney, W. D., Christensen, N. I., 1992. The seismic velocity structure of the deep continental crust. Continental Lower Crust 23, 1–43.

Husen, S., Smith, R. B., Waite, G. P., 2004. Evidence for gas and magmatic sources beneath the Yellowstone volcanic field from seismic tomographic imaging. Journal of Volcanology and Geothermal Research 131 (3), 397–410.

Hwang, Y., Ritsema, J., Goes, S., 2011. Global variation of body-wave attenuation in the upper mantle from teleseismic P wave and S wave spectra. Geophysical Research Letters 38 (8).

Jousset, P., Haberland, C., Bauer, K., Arnason, K., 2011. Hengill geothermal volcanic complex (Iceland) characterized by integrated geophysical observations. Geothermics 40 (1), 1 – 24.

Jousset, P., Hendriyana, A., Jaya, M., Diningrat, W., Rachmat Sule, M., Syahbana, D., Braeuer, B., Otto, C., Merz, M., Muksin, U., et al., 2013. Broadband seismological observations at two phase geothermal area in West Java, Indonesia. In: EGU General Assembly Conference Abstracts. Vol. 15. p. 6908.

Julian, B., Gubbins, D., 1977. Three-dimensional seismic ray tracing. Journal of Geophysics 43 (1), 95–114.

Julian, B. R., Pitt, A., Foulger, G., 1998. Seismic image of a CO2 reservoir beneath a seismically active volcano. Geophysical Journal International 133 (1), F7–F10.

Julian, B. R., Ross, A., Foulger, G. R., Evans, J. R., 1996. Three-dimensional seismic image of a geothermal reservoir: The Geysers, California. Geophysical Research Letters 23 (6), 685–688.

Karato, S.-I., 2003. Mapping water content in the upper mantle. Inside the subduction factory, 135–152.

Kennett, B., Engdahl, E., Buland, R., 1995. Constraints on seismic velocities in the Earth from traveltimes. Geophysical Journal International 122 (1), 108–124.

Kennett, B. L. N., Engdahl, E. R., 1991. Traveltimes for global earthquake location and phase identification. Geophysical Journal International 105 (2), 429–465.

Kissling, E., 1988. Geotomography with local earthquake data. Reviews of Geophysics 26 (4), 659–698.

Kissling, E., Ellsworth, W., Eberhart-Phillips, D., Kradolfer, U., 1994. Initial reference models in local earthquake tomography. Journal of Geophysical Research: Solid Earth (1978–2012) 99 (B10), 19635–19646.

Kohonen, T., 2001. Self-organizing maps. Vol. 30. Springer.

Koulakov, I., 2009. Lotos code for local earthquake tomographic inversion: benchmarks for testing tomographic algorithms. Bulletin of the Seismological Society of America 99 (1), 194–214.

Koulakov, I., Yudistira, T., Luehr, B.-G., et al., 2009. P, S velocity and VP/VS ratio beneath the Toba caldera complex (Northern Sumatra) from local earthquake tomography. Geophysical Journal International 177 (3), 1121–1139.

Lahsen, A., Sepulveda, F., Rojas, J., Palacios, C., 2005. Present status of geothermal exploration in Chile. In: Proceedings World Geothermal Congress.

Lange, D., Cembrano, J., Rietbrock, A., Haberland, C., Dahm, T., Bataille, K., 2008. First seismic record for intra-arc strike-slip tectonics along the Liquiñe-Ofqui fault zone at the obliquely convergent plate margin of the southern Andes. Tectonophysics 455 (1), 14–24.

Lange, D., Tilmann, F., Rietbrock, A., Collings, R., Natawidjaja, D. H., Suwargadi, B. W., Barton, P., Henstock, T., Ryberg, T., 2010. The fine structure of the subducted investigator fracture zone in Western Sumatra as seen by local seismicity. Earth and Planetary Science Letters 298 (1), 47–56.

Lee, W. H. K., Lahr, J. C., 1975. HYPO71 (revised): a computer program for determining hypocenter, magnitude, and first motion pattern of local earthquakes. US Department of the Interior, Geological Survey, National Center for Earthquake Research.

Lee, W. H. K., Valdes, C., 1985. HYPO71PC: A personal computer version of the HYPO71 earthquake location program. Vol. 85. US Geological Survey.

Martínez-Arévalo, C., Patanè, D., Rietbrock, A., Ibánez, J. M., 2005. The intrusive process leading to the Mt. Etna 2001 flank eruption: Constraints from 3-D attenuation tomography. Geophysical Research Letters 32 (21), L21309.

Martínez-Garzón, P., Bohnhoff, M., Kwiatek, G., Dresen, G., 2013. Stress tensor changes related to fluid injection at The Geysers geothermal field, California. Geophysical Research Letters 40 (11), 2596–2601.

Mavko, G., Kjartansson, E., Winkler, K., 1979. Seismic wave attenuation in rocks. Reviews of Geophysics 17 (6), 1155–1164.

Mavko, G. M., 1980. Velocity and attenuation in partially molten rocks. Journal of Geophysical Research: Solid Earth (1978–2012) 85 (B10), 5173–5189.

McCaffrey, R., 2009. The tectonic framework of the Sumatran subduction zone. Annual Review of Earth and Planetary Sciences 37, 345–366.

McCarthy, A., Elders, C., 1997. Cenozoic deformation in Sumatra: oblique subduction and the development of the Sumatran Fault System. Geological Society, London, Special Publications 126 (1), 355–363.

McMechan, G. A., 1983. Seismic tomography in boreholes. Geophysical Journal of the Royal Astronomical Society 74 (2), 601–612.

Menke, W., 1989. Geophysical data analysis: discrete inverse theory. Vol. 45. Access Online via Elsevier.

Morozov, I. B., 2010. On the causes of frequency-dependent apparent seismological Q. Pure and Applied Geophysics 167 (10), 1131–1146.

Mosegaard, K., Sambridge, M., 2002. Monte Carlo analysis of inverse problems. Inverse Problems 18 (3), R29.

Muksin, U., Bauer, K., Haberland, C., 2013a. Seismic Vp and Vp/Vs structure of the geothermal area around Tarutung (North Sumatra, Indonesia) derived from local earthquake tomography . Journal of Volcanology and Geothermal Research 260, 27 – 42.

Muksin, U., Haberland, C., Bauer, K., Weber, M., 2013b. Three-dimensional upper crustal structure of the geothermal system in Tarutung (North Sumatra, Indonesia) revealed by seismic attenuation tomography. Geophysical Journal International 195 (3), 2037–2049.

Muksin, U., Haberland, C., Nukman, M., Bauer, K., Weber, M., 2014. Detailed fault structure of the Tarutung pull-apart basin in Sumatra-Indonesia derived from local earthquake data. Journal of Asian Earth Sciences (submitted).

Muraoka, H., Takahashi, M., Sundhoro, H., Dwipa, S., Soeda, Y., Momita, M., Shimada, K., 2010. Geothermal systems constrained by the sumatran fault and its pull-apart basins in sumatra, western indonesia. In: Proceedings of the World Geothermal Congress. pp. 25–29.

Mustang, A., Widodo, S., Purwoto, E., Rustama, I., 2005. Penyelidikan Geolistrik Daerah Panas Bumi Sipoholon-Tarutung Kabupaten Tapanuli Utara, Provinsi Sumatera Utara. In: Pemaparan Hasil Kegiatan Lapangan Subdit Panas Bumi 2005.

Nakanishi, I., Yamaguchi, K., 1986. A numerical experiment on nonlinear image reconstruction from first-arrival times for two-dimensional island arc structure. Journal of Physics of the Earth 34 (2), 195–201.

Niasari, S., Munoz, G., Kholid, M., E., S., Ritter, O., 2012. Magnetotelluric Exploration of the Sipoholon Geothermal Field, Indonesia. In: Geophysical Research Abstracts, EGU2012-9405-1. Vol. 14.

Nippress, S., Rietbrock, A., Heath, A., 2010. Optimized automatic pickers: application to the ANCORP data set. Geophysical Journal International 181 (2), 911–925.

Nukman, M., Moeck, I., 2013. Structural controls on a geothermal system in the Tarutung Basin, north central Sumatra. Journal of Asian Earth Sciences 74, 86–96.

Paige, C. C., Saunders, M. A., 1982. Lsqr: An algorithm for sparse linear equations and sparse least squares. ACM Transactions on Mathematical Software (TOMS) 8 (1), 43–71.

Park, J., Lindberg, C. R., Vernon, F. L., 1987. Multitaper spectral analysis of high-frequency seismograms. Journal of Geophysical Research: Solid Earth (1978–2012) 92 (B12), 12675–12684.

Pesicek, J. D., Thurber, C. H., Widiyantoro, S., Zhang, H., DeShon, H. R., Engdahl, E. R., 2010. Sharpening the tomographic image of the subducting slab below Sumatra, the Andaman Islands and Burma. Geophysical Journal International 182 (1), 433–453.

Priyono, A., Suantika, G., Widiyantoro, S., Nugraha, A., 2011. Three-dimensional Seismic Attenuation Structure of Mt. Guntur, West Java, Indonesia. International Journal of Tomography & Simulation 17 (S11), 17–28.

Quan, Y., Harris, J. M., 1997. Seismic attenuation tomography using the frequency shift method. Geophysics 62 (3), 895–905.

Rawlinson, N., Sambridge, M., 2003. Seismic traveltime tomography of the crust and lithosphere. Advances in Geophysics 46, 81–198.

Reasenberg, P. A., Oppenheimer, D., 1985. FPFIT, FPPLOT and FPPAGE: Fortran computer programs for calculating and displaying earthquake fault-plane solutions. Open-File Rept. 85-739, 109pp, United States Geolological Survey.

Rietbrock, A., 2001. P wave attenuation structure in the fault area of the 1995 Kobe earthquake. Journal of geophysical research 106 (B3), 4141–4154.

Rose, W., Chesner, C., 1987. Dispersal of ash in the great Toba eruption, 75 ka. Geology 15 (10), 913–917.

Ryberg, T., Hole, J., Fuis, G., Rymer, M., Bleibinhaus, F., Stromeyer, D., Bauer, K., 2012. Tomographic Vp and Vs structure of the California Central Coast Ranges, in the vicinity of SAFOD, from controlled-source seismic data. Geophysical Journal International 190 (3), 1341–1360.

Sambridge, M., Kennett, B., 1990. Boundary value ray tracing in a heterogeneous medium: a simple and versatile algorithm. Geophysical Journal International 101 (1), 157–168.

Sambridge, M., Mosegaard, K., 2002. Monte Carlo methods in geophysical inverse problems. Reviews of Geophysics 40 (3), 3–1.

Sanders, C., 1993. Local earthquake tomography: attenuation theory and results. Seismic Tomography: Theory and Practice, 676–694.

Saragiotis, C. D., Hadjileontiadis, L. J., Panas, S. M., 2002. PAI-S/K: A robust automatic seismic P phase arrival identification scheme. Geoscience and Remote Sensing, IEEE Transactions on 40 (6), 1395–1404.

Saragiotis, C. D., Hadjileontiadis, L. J., Rekanos, I. T., Panas, S. M., 2004. Automatic P phase picking using maximum kurtosis and κ-statistics criteria. Geoscience and Remote Sensing Letters, IEEE 1 (3), 147–151.

Sato, H., Sacks, I. S., Murase, T., Muncill, G., Fukuyama, H., 1989. Qp-melting temperature relation in peridotite at high pressure and temperature: Attenuation mechanism and implications for the mechanical properties of the upper mantle. Journal of Geophysical Research: Solid Earth (1978–2012) 94 (B8), 10647–10661.

Scherbaum, F., 1990. Combined inversion for the three-dimensional Q structure and source parameters using microearthquake spectra. Journal of Geophysical Research: Solid Earth (1978–2012) 95 (B8), 12423–12438.

Schurr, B., Asch, G., Rietbrock, A., Trumbull, R., Haberland, C., 2003. Complex patterns of fluid and melt transport in the central Andean subduction zone revealed by attenuation tomography. Earth and Planetary Science Letters 215 (1), 105–119.

Shapiro, N. M., Ritzwoller, M. H., Engdahl, E. R., 2008. Structural context of the great Sumatra-Andaman Islands earthquake. Geophysical Research Letters 35 (5), L05301.

Sieh, K., Natawidjaja, D., 2000. Neotectonics of the Sumatran fault, Indonesia. Journal of Geophysical Research: Solid Earth (1978–2012) 105 (B12), 28295–28326.

Sipkin, S. A., 1994. Rapid determination of global moment-tensor solutions. Geophysical Research Letters 21 (16), 1667–1670.

Situmorang, T., 2005. Penyelidikan geomagnet daerah panas Bumi Ria-Ria Sipoholon, Tarutung, Tapanuli Utara-Sumatra Utara. In: Pemaparan Hasil Kegiatan Lapangan Subdit Panas Bumi 2005.

Smith, W. D., 1981. The b-value as an earthquake precursor. Nature 289 (5794), 136–139.

Smithsonian Institution, National Museum of Natural History, Global Volcanism Program, 2012. http://www.volcano.si.edu. Accessed: 2012-02-26.

Snoke, J., Munsey, J., Teague, A. G., Bollinger, G., 1984. A program for focal mechanism determination by combined use of polarity and SV-P amplitude ratio data. Earthquake notes 55 (3), 15.

Stankiewicz, J., Bauer, K., Ryberg, T., 2010a. Lithology classification from seismic tomography: additional constraints from surface waves. Journal of African Earth Sciences 58 (3), 547–552.

Stankiewicz, J., Ryberg, T., Haberland, C., Natawidjaja, D., et al., 2010b. Lake Toba volcano magma chamber imaged by ambient seismic noise tomography. Geophysical Research Letters 37 (17).

Stein, S., Wysession, M., 2009. An Introduction to Seismology, Earthquakes, and Earth Structure. Wiley.

Subarya, C., Chlieh, M., Prawirodirdjo, L., Avouac, J.-P., Bock, Y., Sieh, K., Meltzner, A. J., Natawidjaja, D. H., McCaffrey, R., 2006. Plate-boundary deformation associated with the great Sumatra-Andaman earthquake. Nature 440, 2.

Swanson, M. T., 1990. Extensional duplexing in the York Cliffs strike-slip fault system, southern coastal Maine. Journal of Structural Geology 12 (4), 499–512.

Takanami, T., Selwyn Sacks, I., Hasegawa, A., 2000. Attenuation structure beneath the volcanic front in northeastern Japan from broad-band seismograms. Physics of the Earth and Planetary Interiors 121 (3), 339–357.

Tatsumi, Y., 1989. Migration of fluid phases and genesis of basalt magmas in subduction zones. Journal of Geophysical Research 94 (B4), 4697–4707.

Teyssier, C., Tikoff, B., Markley, M., 1995. Oblique plate motion and continental tectonics. Geology 23 (5), 447–450.

Thurber, C., 1993. Local earthquake tomography: velocities and Vp/Vs-theory. Seismic Tomography: Theory and Practice, 563–583.

Thurber, C., Roecker, S., Ellsworth, W., Chen, Y., Lutter, W., Sessions, R., 1997. Two-dimensional seismic image of the San Andreas Fault in the Northern Gabilan Range, central California: Evidence for fluids in the fault zone. Geophysical Research Letters 24 (13), 1591–1594.

Thurber, C. H., 1983. Earthquake locations and three-dimensional crustal structure in the Coyote Lake area, central California. Journal of Geophysical Research: Solid Earth (1978-2012) 88 (B10), 8226–8236.

Toomey, D. R., Foulger, G. R., 1989. Tomographic inversion of local earthquake data from the Hengill-Grensdalur Central Volcano Complex, Iceland. Journal of Geophysical Research: Solid Earth 94 (B12), 17497–17510.

Um, J., Thurber, C., 1987. A fast algorithm for two-point seismic ray tracing. Bulletin of the Seismological Society of America 77 (3), 972–986.

USGS National Earthquake Information Center, 2012. http://earthquake.usgs.gov. Accessed: 2012-02-26.

Van der Hilst, R., Engdahl, E., Spakman, W., Nolet, G., 1991. Tomographic imaging of subducted lithosphere below northwest Pacific island arcs. Nature 353, 37–42.

Vidale, J., 1988. Finite-difference calculation of travel times. Bulletin of the Seismological Society of America 78 (6), 2062–2076.

Walck, M. C., 1988. Three-dimensional Vp/Vs variations for the Coso region, California. Journal of Geophysical Research: Solid Earth (1978–2012) 93 (B3), 2047–2052.

Waldhauser, F., Ellsworth, W. L., 2000. A double-difference earthquake location algorithm: Method and application to the northern Hayward fault, California. Bulletin of the Seismological Society of America 90 (6), 1353–1368.

Walsh, J., 1995. Seismic attenuation in partially saturated rock. Journal of Geophysical Research: Solid Earth (1978–2012) 100 (B8), 15407–15424.

Wang, Z., Nur, A., 1990. Wave velocities in hydrocarbon-saturated rocks: Experimental results. Geophysics 55 (6), 723–733.

Weller, O., Lange, D., Tilmann, F., Natawidjaja, D., Rietbrock, A., Collings, R., Gregory, L., 2012. The structure of the Sumatran Fault revealed by local seismicity. Geophysical Research Letters 39 (1).

Whittaker, J., Müller, R., Sdrolias, M., Heine, C., 2007. Sunda-Java trench kinematics, slab window formation and overriding plate deformation since the Cretaceous. Earth and Planetary Science Letters 255, 445 – 457.

Widiyantoro, S., Kennett, B., van der Hilst, R., 1999. Seismic tomography with P and S data reveals lateral variations in the rigidity of deep slabs. Earth and Planetary Science Letters 173 (1-2), 91 – 100.

Wiyono, W., Polom, U., Krawczyk, C. M., 2013. P- and SH-wave high-resolution seismic experiments in pyroclastic sediments - a case study from volcanic regions in Indonesia. Near Surface Geophysics (in review).

Woodcock, N. H., Fischer, M., 1986. Strike-slip duplexes. Journal of Structural Geology 8 (7), 725 – 735.

Wu, H., Lees, J. M., 1996. Attenuation structure of Coso geothermal area, California, from wave pulse widths. Bulletin of the Seismological Society of America 86 (5), 1574–1590.

Yang, X., Lay, T., Xie, X.-B., Thorne, M. S., 2007. Geometric spreading of Pn and Sn in a spherical Earth model. Bulletin of the Seismological Society of America 97 (6), 2053–2065.

Zucca, J., Hutchings, L., Kasameyer, P., 1994. Seismic velocity and attenuation structure of the Geysers geothermal field, California . Geothermics 23 (2), 111 – 126.

Zucca, J. J., Evans, J. R., 1992. Active high-resolution compressional wave attenuation tomography at Newberry Volcano, Central Cascade Range. Journal of Geophysical Research: Solid Earth (1978–2012) 97 (B7), 11047–11055.

List of Figures

List of Tables

Appendix A

Hot Springs

Figure A.1: Hot spring in Sipoholon (Riaria)

Figure A.2: Hot spring in Hutabarat

Figure A.3: Hot spring in Panabungan

Appendix B

Seismic network

B.1 Station list

Name	Longitude	Latitude	Elevation	Start date	End date
X01	1.978679	99.00215	989	2011.05.18	2012.03.13
X03	1.974531	98.91524	1154	2011.05.19	2012.03.14
X04	2.030251	98.95348	984	2011.05.17	2012.03.13
X05	2.060021	98.93164	1035	2011.05.17	2012.03.13
X06	1.781707	99.12202	481	2011.05.17	2012.03.14
X07	2.117587	98.97785	1181	2011.05.17	2012.03.14
X08	2.213883	98.98918	1297	2011.05.17	2012.03.14
X09	2.204280	99.01766	1280	2011.05.17	2012.03.14
X10	2.137429	99.04877	1169	2011.05.16	2012.03.14
X11	2.120006	99.08561	1238	2011.05.16	2012.03.14
X12	2.033331	99.11510	1222	2011.05.16	2012.03.15
X13	2.007656	99.15375	1247	2011.05.16	2012.03.15
X14	2.078326	99.02426	1168	2011.05.17	2012.03.14
X15	2.059676	98.98766	1173	2011.05.17	2012.03.14
X16	2.113229	98.93632	1175	2011.05.18	2012.03.13
X17	2.139549	98.90797	1208	2011.05.18	2012.03.15
X18	2.135479	98.86336	1431	2011.05.17	2012.03.14
X19	2.118341	98.79644	1339	2011.05.18	2012.03.15
X20	2.084819	98.78733	1020	2011.05.18	2012.03.13
X21	2.193766	98.90043	1204	2011.05.18	2012.03.14
X22	1.891750	98.92815	1071	2011.05.19	2012.03.13
X23	1.862799	98.90614	822	2011.05.19	2012.03.13
X24	1.892797	98.83789	591	2011.05.19	2012.03.13
X25	1.860372	98.86271	516	2011.05.17	2012.03.14
X26	1.960545	98.96302	1582	2011.05.18	2012.03.13
X27	2.018496	99.00202	1242	2011.05.16	2012.03.13
X28	2.009631	99.03136	1240	2011.05.16	2012.03.13
X29	2.034300	99.07954	1237	2011.05.17	2012.03.14
X30	1.966110	99.14615	1234	2011.05.17	2012.03.15
X31	1.940893	99.21737	1204	2011.05.17	2012.03.15
X32	1.967814	99.08639	1265	2011.05.17	2012.03.15
X33	1.878791	99.05121	516	2011.05.17	2012.03.14
X34	1.916467	99.03991	936	2011.05.18	2012.03.14
X35	1.935580	98.96575	1014	2011.05.18	2012.03.13
X36	1.924287	98.92096	1066	2011.05.19	2012.03.13
X37	2.156476	98.99382	1193	2011.05.17	2012.03.15
X38	2.073751	98.89213	1212	2011.05.18	2012.03.14
X39	2.048021	98.86287	1139	2011.05.18	2012.03.14

X40	2.098064	98.84665	1486	2011.05.16	2012.03.14
X42	1.714510	99.15665	484	2011.09.13	2012.03.13
X43	1.820250	99.08403	515	2011.05.13	2012.03.13
X44	2.003805	98.95621	1081	2011.09.13	2012.03.12

B.2 Pictures of stations

Figure B.1: One of the seismic stations and the deployment team

Aknowledgement

I would like to express a deep sense of gratitude to a large number of people: my family, colleagues and staff at German Research Centre for Geosciences, GFZ-Potsdam for their supports and encouragement when the research had been conducted. Foremost, I would like to thank to my supervisor Prof. Dr. Michael Weber, the Head of the Department 2 "Physics of the Earth", and also the Section 2.2. "Geophysical Deep Sounding" at German Research Center for Geosciences, GFZ-Potsdam.

Special thanks to Dr. Klaus Bauer and Dr. Christian Haberland as my advisory team at GFZ-Potsdam for their invaluable help, discussion and guidance in the use of several seismological methods I applied in this research. Together with Prof. Dr. Michael Weber they are also the co-authors of my papers I include in the dissertation. Dr. Benjamin Bräuer is thanked for the help on the application of the seismological methods. I would like to thank to Prof. Dr. Inga Moeck for the discussions of the interpretation of the seismological results.

My great appreciation goes to Prof. Dr. Ernst Huenges, the Head of International Centre for Geothermal Research GFZ-Potsdam and the management team of the Indonesian Geothermal Project, Dr. Kemal Erbas, Prof. Dr. David Bruhn, and Dr. Makky Sandra Jaya. Their efforts have made this research is possible to be conducted and funded by the Federal Ministry of Education and Research (BMBF) of Germany under the umbrella project called "Sustainability concepts for exploitation of geothermal reservoirs in Indonesia".

Dr. Mochammad Nukman and Sintia Windhi Niasari, the members of the Tarutung geothermal exploration group, are thanked for the discussions of the seismology results in comparison with the structural geology and the magnetotelluric results. My deepest thanks to Edi Soehanto from Center for Geological Resource, Geological Agency of Indonesia who supported the shipping of the instruments to the field. I would like to thank to all people who invloved in the field experiments from different institutions: Dr. Trond Ryberg, Dr. Klaus Bauer, Dr. Benjamin Bräuer, Dr. Jacek Stankiewicz, Christof Lendl (GFZ-Potsdam, Germany), Dr. Nazli Ismail, Irwandi Nurdin, Zakiul Fuady (Syiah Kuala University, Aceh, Indonesia), Doddi Tampubolon, Oki Hutauruk (the University of North Sumatra, Indonesia), and Mekto P. Purba (Dinas ESDM, Tarutung North Tapanuli, Indonesia).

This dissertation is a special present to my beloved wife, Wanti Meiriyana, and my son, Ahmad Habibie, who always support me in my study.

Declaration of Originality

I, hereby, declare that this dissertation and the work reported herein was composed by and originated entirely from me. Information derived from the published and unpublished work of others has been acknowledged in the text and references are given in the list of sources.

Potsdam, April 2014

Muksin